



**Michigan
Technological
University**

Michigan Technological University
Digital Commons @ Michigan Tech

Dissertations, Master's Theses and Master's Reports

2019

Modeling and Control of Maximum Pressure Rise Rate in RCCI Engines

Aditya Basina

Michigan Technological University, abasina@mtu.edu

Copyright 2019 Aditya Basina

Recommended Citation

Basina, Aditya, "Modeling and Control of Maximum Pressure Rise Rate in RCCI Engines", Open Access Master's Thesis, Michigan Technological University, 2019.

<https://digitalcommons.mtu.edu/etdr/865>

Follow this and additional works at: <https://digitalcommons.mtu.edu/etdr>



Part of the [Automotive Engineering Commons](#), [Controls and Control Theory Commons](#), and the [Heat Transfer, Combustion Commons](#)

MODELING AND CONTROL OF MAXIMUM PRESSURE RISE RATE IN RCCI
ENGINES

By

Laxmi Narayana Aditya Basina

A THESIS

Submitted in partial fulfillment of the requirements for the degree of

MASTER OF SCIENCE

In Mechanical Engineering

MICHIGAN TECHNOLOGICAL UNIVERSITY

2019

© 2019 Laxmi Narayana Aditya Basina

This thesis has been approved in partial fulfillment of the requirements for the Degree of MASTER OF SCIENCE in Mechanical Engineering.

Department of Mechanical Engineering-Engineering Mechanics

Thesis Advisor: *Dr. Mahdi Shahbakhti*

Committee Member: *Dr. Jeffery Naber*

Committee Member: *Dr. Jeremy Worm*

Department Chair: *Dr. William W Predebon*

Dedication

To my parents Dr. K. Anuradha and Dr. B. Gouri Sankar Rao

Contents

List of Figures	xi
List of Tables	xv
Preface	xvii
Acknowledgments	xix
List of Abbreviations	xxi
Nomenclature	xxv
Abstract	xxvii
1 Introduction	1
1.1 LTC strategies	4
1.2 RCCI control	9
1.3 Shortcomings of state of the art	15
1.4 Objectives of this Thesis	16
1.5 Structure of this Thesis	17

2	Experimental setup and Analysis	19
2.1	Engine specifications	19
2.2	Modifications made for RCCI operation	20
2.3	Data Acquisition	22
2.4	Test Procedure	24
2.5	Uncertainty Analysis for Measured and Derived Parameters	26
2.6	Maximum Pressure Rise Rate calculation	28
2.7	Coefficient Of Variance of IMEP	29
2.8	Experimental data analysis	31
3	Dynamic model for RCCI combustion	35
3.1	Introduction	35
3.2	SOC model	37
3.3	Maximum Pressure Rise Rate modeling	39
3.3.1	Introduction	39
3.3.2	Double Wiebe vs Single Wiebe function	43
3.3.3	Parametrization of Single Wiebe function	44
3.3.4	PR Transient	47
3.3.5	SOI Transient	48
3.3.6	Statistical Analysis	48
3.4	CA50 model	50
3.5	IMEP Model	51

3.6	Cycle by Cycle dynamic model	52
3.6.1	Intake stroke ($IVO \rightarrow IVC$)	53
3.6.2	Polytropic Compression $IVC \rightarrow SOC$	55
3.6.3	Combustion ($SOC \rightarrow EOC$)	56
3.6.3.1	BD Model for EOC estimation	56
3.6.4	Polytropic Expansion ($EOC \rightarrow EVO$)	59
3.6.5	Exhaust stroke ($EVO \rightarrow EVC$)	59
3.7	Data Driven LPV identification	62
3.7.1	Introduction	62
3.7.2	DDM for LPV identification	63
3.7.3	LPV model identification and validation	70
4	Combustion Phasing and Load Control with MPRR Limitation	75
4.1	Development of the LPV system	75
4.2	Model Predictive Controller (MPC)	79
4.2.1	Controller design	79
4.2.2	Tracking performance	84
4.3	Motivation for split DI fuel injection	90
5	Conclusions and Future work	93
5.1	Summary and Conclusions	93
5.2	Future work	96

References	99
A Control Oriented Modeling of split injection in RCCI engines .	115
A.1 Wiebe function modeling for Split injection	116
A.2 Modifying MKIM for split injection	118
B Combustion regime separation in RCCI combustion	121
C Experimental Data used for Parametrizing the MVM for MPRR	127
C.1 Data used for parametrizing the MVM for MPRR	127
C.2 Data used for validating the MVM for MPRR	133
D Programs and data files summary	139
D.1 Chapter 1	139
D.2 Chapter 2	140
D.3 Chapter 3	140
D.4 Chapter 4	141
D.5 Appendix A	141
D.6 Appendix B	141
E Letters of Permission	143

List of Figures

1.1	Emission maps of LTC strategies [26]	3
1.2	Recent studies in RCCI research [34, 35, 36, 37, 38, 39, 40]	6
1.3	Gasoline-Diesel (left) vs Ethanol-Diesel (right) operating points [43]	7
1.4	Prior work in RCCI control [1, 3, 4, 5, 50, 51, 52, 53]	10
1.5	LQI controller implemented by Sadabadi et al. [1]	12
1.6	Feedback PI controller implemented by Arora et al. for real time control of RCCI engine [53]	13
1.7	Thesis organization	18
2.1	LTC Engine setup [4]	21
2.2	Experimental setup	22
2.3	Data acquisition setup	24
2.4	Variations of MPRR as a function of SOI, FQ and PR. (a) $N = 1000$, $T_{in} = 60^\circ$, SOI = 40 CAD bTDC, (b) $N = 1000$, $T_{in} = 60^\circ$, SOI = 50 CAD bTDC,(c) $N = 1000$, $T_{in} = 60^\circ$, SOI = 60 CAD bTDC	32

2.5	Standard deviation of MPRR for 87 data points as shown in Table 2.3. SOI: 20 - 60 (CAD bTDC); PR: 10 - 60 (-); FQ: 9 - 29 (mg/cycle). Standard deviation is calculated over 100 cycles for each data point.	34
3.1	Effect of double Wiebe function accuracy on MPRR prediction, FQ = 17 mg/cycle, SOI = 40 bTDC, PR = 20	44
	(a) Accurate double Wiebe function	44
	(b) Inaccurate double Wiebe function	44
3.2	Data points used for parametrizing the model N = 1000 RPM, T_{in} = 60° C	46
3.3	Experimental validation of the MPRR model at N = 1000 RPM, T_{in} = 60° C	46
3.4	Transient validation of the MPRR model at N = 1000 RPM, T_{in} = 60° C, SOI = 40 CAD bTDC and FQ = 22 mg/cycle	47
3.5	Transient validation of the MPRR model at N = 1000 RPM, T_{in} = 60° C, PR = 40 and FQ = 21 mg/cycle	48
3.6	Statistical Analysis for three different operating conditions. (a) N = 1000, T_{in} = 60°, FQ = 19 mg/cycle, SOI = 40 bTDC, PR = 20 ,(b) N = 1000, T_{in} = 60°, FQ = 19 mg/cycle, SOI = 35 bTDC, PR = 20,(c) N = 1000, T_{in} = 60°, FQ = 22 mg/cycle, SOI = 45 bTDC, PR = 60	49
	(a) Least variation	49
	(b) Average variation	49

(c) Maximum variation	49
3.7 Cycle by cycle RCCI dynamic model schematic	61
3.8 Inputs to RCCI dynamic Model $N = 1000$ RPM, $T_{in} = 60^\circ$ C	71
3.9 State outputs from the RCCI dynamic model $N = 1000$ RPM, $T_{in} = 60^\circ$ C	72
3.10 Data driven SVM based LPV identification on validation data set at $N = 1000$ RPM, $T_{in} = 60^\circ$ C	72
4.1 $A(p_k)$ vs scheduling parameter (PR)	77
4.2 $A(p_k)$ vs scheduling parameter (PR)	77
4.3 Schematic of the LPV - Adaptive MPC setup for controlling CA50 and IMEP with MPRR limitation	83
4.4 CA50 and IMEP tracking <u>without</u> MPRR limitation. Magenta colored dotted lines show the bounds for Inputs and Outputs	86
4.5 CA50 and IMEP tracking <u>with</u> MPRR limitation. Magenta colored dotted lines show the bounds for Inputs and Outputs	87
4.6 CA50 and IMEP tracking <u>with</u> MPRR limitation and <u>noise</u> . Magenta colored dotted lines show the bounds for Inputs and Outputs	88
4.7 CA50 and IMEP tracking <u>with</u> MPRR limitation. Magenta colored dotted lines show the bounds for Inputs and Outputs.	89
4.8 Heat Release Rate (HRR) modeling for split injection	91
A.1 HRR modeling for split injection	117

A.2	Effect of ρ and SOI on SOC	120
(a)	$\rho_{pilot} = 10\%$	120
(b)	$\rho_{pilot} = 50\%$	120
(c)	$\rho_{pilot} = 90\%$	120
B.1	Different combustion regimes seen during RCCI operation	122
B.2	Effect of different parameters on heat release shape	124
(a)	Effect of SOI	124
(b)	Effect of FQ	124
(c)	Effect of PR	124
(d)	Effect of SOC	124
B.3	Combustion regime separation	125
E.1	Letter of permission	143
E.2	Letter of permission	144

List of Tables

2.1	Engine Specifications	20
2.2	Fuel Specifications	22
2.3	RCCI Test Conditions	26
2.4	Measured parameters and their uncertainties	27
2.5	Derived parameters and their uncertainties	28
3.1	Optimized parameters for MKIM	39
3.2	Operating conditions for parametrization and validation of the Wiebe function	45
3.3	Optimized parameters for MPRR model	46
3.4	Optimized parameters for CA50 model	51
3.5	Optimized parameters for the BD model	58
4.1	Input constraints	84
4.2	Output constraints	84
C.1	Experimental data used for parametrizing the MVM for MPRR	128
C.2	Experimental data used for parametrizing the MVM for MPRR	134

D.1	Figure Files	139
D.2	Visio Files	139
D.3	Visio Files	140
D.4	Plot files	140
D.5	Plot Files	140
D.6	Plot Files	141
D.7	Visio Files	141
D.8	Plot Files	141
D.9	Plot Files	142

Preface

The work presented in this thesis is built upon the previous works done by Kaveh Sadabadi [1], Kaushik Kannan [2], Nitin Kondipati [3], Akshat Raut [4] and Behrouz Khoshbakht [5]. The work from [1, 2, 3, 4] helped to develop the dynamic RCCI engine model presented in Sections 3.3, 3.4, 3.5 and 3.6 that has been used to simulate an RCCI engine. The work from [5, 6] helped to develop the data driven modeling technique presented in Section 3.7, used to develop the LPV representation of the RCCI engine. Dr. Mahdi Shahbakhti gave technical guidance in developing the MPRR model, LPV and MPC models and design of controllers. Dr. Javad Mohammadpur gave technical advice in developing the MATLAB[®] code for Data Driven Modeling of the RCCI engine presented in Section 3.7. The work by Radhika Sitaraman has aided in tuning the Data Driven Modeling MATLAB[®] code in Section 3.7.

Acknowledgments

I would like to thank my parents and my family for supporting me through this endeavor and constantly supporting and believing in me.

I would also like to thank Dr. Shahbakhti for advising me and for helping me gain not just technical knowledge but also for pushing me to do my best every single time.

I also extend my gratitude to Dr. Naber and Dr. Worm for agreeing to be on my committee. I would like to thank Behrouz for helping me throughout my work and explaining different concepts and being a great mentor.

List of Abbreviations

AFR	Air Fuel Ratio
aBDC	after Bottom Dead Centre
aTDC	after Top Dead Centre
bBDC	Before Bottom Dead Centre
BDC	Bottom Dead Centre
BR	Blending Ratio
bTDC	before Top Dead Centre
CA50	Crank Angle at 50% heat release
CAD	Crank Angle Degree
CDC	Conventional Diesel Combustion
CFD	Computational Fluid Dynamics
CI	Compression Ignition
CN	Cetane Number
COM	Control Oriented Model
COV	Co-efficient of Variation
CR	Compression Ratio
DDM	Data Driven Modeling
DI	Direct Injection

E85	Ethanol fuel blend containing 85% ethanol
EVC	Exhaust Valve Closing
EVO	Exhaust Valve Opening
FAR	Fuel to Air Ratio
FPGA	Field Programmable Gate Array
FQ	Fuel Quantity
GDI	Gasoline Direct Injection
HCCI	Homogeneous Charge Compression Ignition
HRR	Heat Release Rate
ICE	Internal Combustion Engine
ID	Ignition Delay
IMEP	Indicated Mean Effective Pressure
IVC	Intake Valve Closing
IVO	Intake Valve Opening
LHV	Lower Heating Value
LPV	Linear Parameter Varying
LQI	Linear Quadratic Integral
LTC	Low Temperature Combustion
MABX	Micro Auto Box
mf	Mass of Fuel
MIMO	Multi Input Multi Output

MKIM	Modified Knock Integral Model
ML	Machine Learning
MPC	Model Predictive Control
MPPR	Maximum Pressure Rise Rate
MVM	Mean Value Model
PCCI	Pre-mixed Charge Compression Ignition
PFI	Port Fuel Injection
PM	Particulate Matter
PR	Pre-mixed Ratio
PRR	Pressure Rise Rate
PPCI	Partially Pre-mixed Compression Ignition
RCCI	Reactivity Controlled Compression Ignition
SI	Spark Ignition
SOC	Start of Combustion
SOI	Start of Ignition
SVM	Support Vector Machine
TDC	Top Dead Centre
UHC	Unburnt Hydrocarbons

Nomenclature

Symbol	Variable	Units
c_v	Specific heat at constant volume	KJ/Kg.K
LHV	Lower Heating Value	MJ/Kg
\dot{m}_{air}	Mass flow of air	g/s
\dot{m}_{fuel}	Mass flow of fuel	mg/cycle
$m_{f_{iso}}$	Mass of iso-octane fuel	mg/cycle
$m_{f_{nhep}}$	Mass of n-heptane fuel	mg/cycle
N	Engine speed	RPM
n_c	Polytropic coefficient for compression	-
n_e	Polytropic coefficient for expansion	-
P_{in}	Intake Pressure	KPa
P_{ivc}	Pressure at IVC	KPa
r_c	Compression Ratio	-
S_{ig}	Spontaneous ignition front speed	m/s
T_{exh}	Exhaust Temperature	K
T_{in}	Intake Temperature	K
T_{ivc}	Temperature at IVC	K
T_{rg}	Temperature of Residual gas	K

U_x	Uncertainty in measured parameters	-
U_y	Uncertainty in derived parameters	-
V	Volume	m^3
X	State vector	-
X_b	Mass Fraction Burn	-
$\Delta\phi$	Gradient of equivalence ratio	-
ΔT	Temperature rise	K
γ	Ratio of specific heats	-
ϕ	Equivalence ratio	-
τ	Ignition Delay	sec
θ	Crank Angle	CAD

Abstract

Low Temperature Combustion (LTC) is a combustion strategy that burns fuel at lower temperatures and leaner mixtures in order to achieve high efficiency and near zero NO_x emissions. Since the combustion happens at lower temperatures it inhibits the formation of NO_x and soot emissions. One such strategy is Reactivity Controlled Compression Ignition (RCCI). One characteristic of RCCI combustion and LTC combustion in general is short burn durations which leads to high Pressure Rise Rates (PRR). This limits the operation of these engines to lower loads as at high loads, the Maximum Pressure Rise Rate (MPRR) hinders the use of this combustion strategy.

This thesis focuses on the development of a model based controller that can control the Crank Angle for 50% mass fraction burn (CA50) and Indicated Mean Effective Pressure (IMEP) of an RCCI engine while limiting the MPRR to a pre determined limit. A Control Oriented Model (COM) is developed to predict the MPRR in an RCCI engine. This COM is then validated against experimental data. A statistical analysis of the experimental data is conducted to understand the accuracy of the COM. The results show that the COM is able to predict the MPRR with reasonable accuracy in steady state and transient conditions. Also, the COM is able to capture the trends during transient operation. This COM is then included in an existing cycle by cycle dynamic RCCI engine model and used to develop a Linear Parameter

Varying (LPV) representation of an RCCI engine using Data Driven Modeling (DDM) approach with Support Vector Machines (SVM). This LPV representation is then used along with a Model Predictive Controller (MPC) to control the CA50 and IMEP of the RCCI engine model while limiting the MPRR. The controller was able to track the desired CA50 and IMEP with a mean error of 0.9 CAD and 4.7 KPa respectively while maintaining the MPRR below 5.8 bar/CAD.

Chapter 1

Introduction

The use of fossil fuels and the extent of environmental damage it has caused in the past few decades has driven the industry and the society in general towards tougher regulations and control of the use of the fuels. Automobiles being one of the largest consumers of fossil fuel has been presented with the challenge of improving the efficiency of the machines and reduce the extent of pollution caused by them [7, 8]. Automobiles are the largest producers of CO₂ emissions right after electricity generation [9, 10]. Hence, the regulating bodies in the USA, have set high standards for fuel economy and emissions for 2025 [11]. However, the projected use of fossil fuels is not going down [12]. Even by 2040 fossil fuels are projected to be the largest producers of energy over other sources. In order to meet the regulations and achieve the level of efficiency necessary, the automotive industry has been working on various

types of technologies [13]. Diesel is more efficient than gasoline but produces higher emissions of Nitrogen Oxides (NO_x) and Particulate Matter (PM) [14]. Processing these emissions requires catalytic converters. But, the cost of catalytic converters is rising with increase in complexity. Various technologies such as turbo-charging, cylinder deactivation and GDI have been explored but every added technology adds a certain cost making the development and by implication the cost of the product higher [13].

In order to meet the emission and fuel economy regulations, it is necessary to achieve a higher efficiency for the ICE while reducing its emissions. Higher efficiencies can be achieved by reducing the losses within the ICE. However, different emission particles need different strategies to avoid them. NO_x can be avoided by having lower temperature combustion while PM can be avoided by eliminating the chance of formation of rich mixture pockets and having a homogenous mixture of fuel and air [3].

Low Temperature Combustion (LTC) strategies have gained attention over the past years [15, 16, 17, 18, 19, 20, 21, 22, 23, 24, 25, 26, 27, 28] as a potential solution. All LTC strategies work with lean combustion thus reducing the peak temperatures of the cylinder and hence reducing the heat losses to the wall [18] and also reducing the NO_x emissions [19, 20]. Some of them use a strategy for mixing two fuels. Some involve unthrottled intake of air thus reducing throttling losses. They form a homogenous mixture of the fuels thus reducing local rich regions, hence avoiding the PM emissions.

However, HC and CO emissions are an area of concern due to low temperatures not favoring their oxidation and also they suffer from increased chances of misfires [3]. There are multiple strategies within LTC regimes. A comparison of their emissions with conventional diesel combustion is shown in Figure 1.1. It can be seen that the LTC regimes Homogenous Charge Compression Ignition (HCCI), Reactivity Controlled Compression Ignition (RCCI) and Premixed Charge Compression Ignition (PCCI) avoid the regions of temperature and equivalence ratio where soot or NO_x is formed. However, it should also be noted that the range of operation of LTC regimes is smaller than that of conventional diesel combustion.

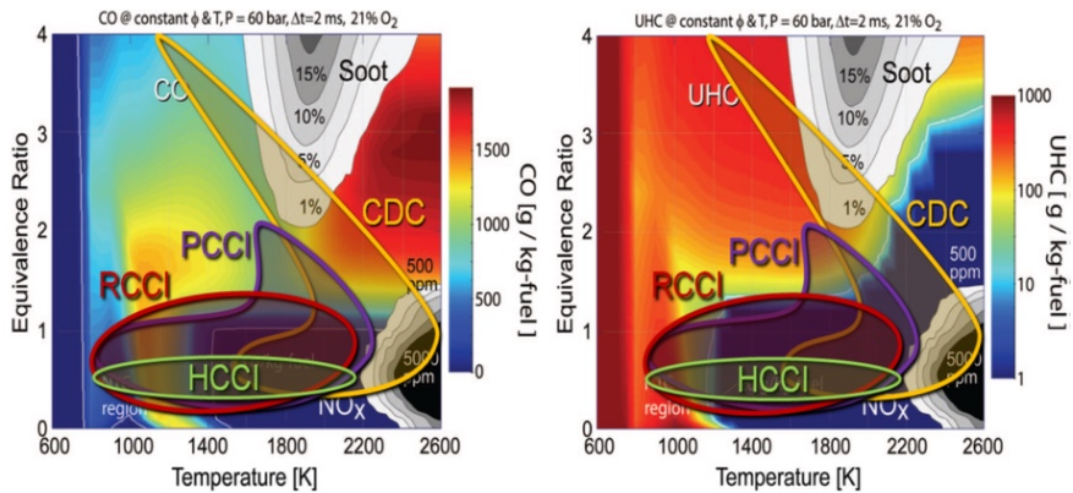


Figure 1.1: Emission maps of LTC strategies [26]

1.1 LTC strategies

There are multiple LTC strategies each having a different homogeneity of mixture and stratification of the charge. HCCI combustion strategy has a homogenous mixture throughout. A homogenous mixture of air and fuel is injected and compressed to auto ignition. This leads to a very short combustion duration and almost constant volume combustion of the mixture which can lead to knock. Hence, HCCI combustion is knock limited at higher loads. Also, there is no direct control for combustion phasing such as injection timing for compression ignition and spark timing for spark ignition. It further suffers from the lack of control of heat release rate which is done with fuel flow in Compression Ignition engines and turbulent flame propagation in SI engines. [29, 30].

Premixed Charge Compression Ignition (PCCI) is another strategy that tries to overcome the challenges of HCCI. The fuel is injected early directly into the cylinder which then creates a homogenous mixture for auto ignition. The same strategy is called Partially Premixed Compression Ignition (PPCI) if the injection is done late into the compression stroke [31]. This is because the mixing of the fuel and air within the cylinder is only partial as the fuel is injected closer to TDC and there is not much time for the fuel and air to mix. This strategy gave control over the combustion phasing with the Start of Injection (SOI) and over the heat release rate with the

amount of fuel added [32]. However, PPCI of diesel required higher rates of Exhaust Gas Recirculation (EGR) to maintain low NO_x and PM emissions while the gasoline PPCI generated higher NO_x emissions and lower efficiency [15, 16]. PCCI was explored further using either diesel and gasoline, [17, 32] which led to the development of a dual injection strategy which allowed control over combustion phasing with SOI.

Work by Bessonette et al. [33] suggested that the use of fuel blends has the potential to increase the operating range of HCCI engines. They had achieved an increase of 60% in the peak load to 16 bar. They had also observed that for low load combustion, a fuel of derived cetane number ≈ 45 was necessary. In addition, research by Inagaki et al. [24] showed that the use of premixed fuels can help reduce the rate of heat release and also combustion noise. This encouraged the research by Kokjohn et al. into the use of dual fuels in an HCCI regime [23]. A high reactivity fuel similar to diesel or n-heptane and a low reactivity fuel similar to gasoline or iso-octane were to be injected into the cylinder to form a mixture. This then gave a direct control over the reactivity of the charge within the cylinder. Kokjohn et al. named it as Reactivity Controlled Compression Ignition (RCCI) [25, 27]. To achieve the dual fuel combustion, the low reactivity fuel is injected into the cylinder via port fuel injection and the high reactivity fuel is injected into the cylinder via direct injection. RCCI is an improvement over the PCCI and PPCI strategies. It has a better control over the combustion phasing and the heat release rate. By controlling the amount of reactivity within the chamber RCCI is able to control the combustion events in the cylinder

more effectively when compared to other LTC strategies. The stratification of fuel reactivity leads to staged combustion of the fuel with the higher reactive fuel auto igniting first and then low reactivity fuel burns. This leads to a longer duration of combustion when compared to HCCI and thus reduces the Maximum Pressure Rise Rate (MPRR) within the cylinder.

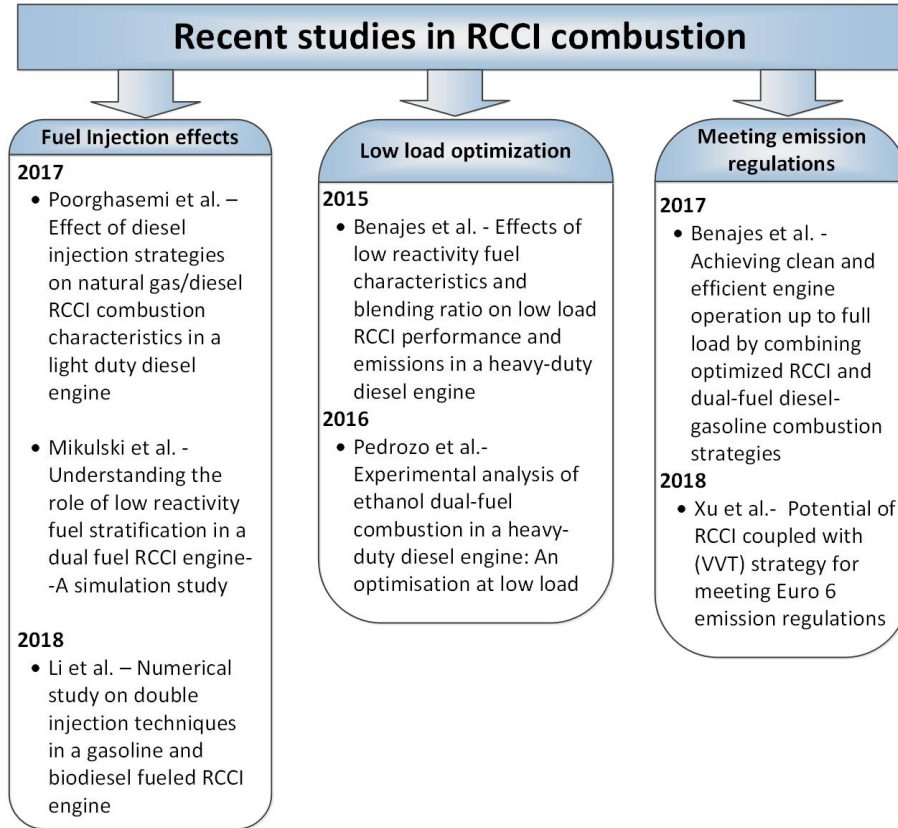


Figure 1.2: Recent studies in RCCI research [34, 35, 36, 37, 38, 39, 40]

RCCI combustion still has some challenges to overcome. Some of the notable recent studies into RCCI engines are shown in Fig. 1.2. As all LTC strategies, RCCI also suffers from high Unburnt Hydrocarbons (UHC) and Carbon Monoxide (CO) emissions.

The required EGR for high loads is very high [23] and the required Compression Ratio (CR) is also low [41]. This then led to the study of using fuels other than gasoline such as natural gas and ethanol and the use of mode switching strategies between RCCI and Conventional Diesel Combustion (CDC). The emission characteristics have also been studied [42, 43] along with the study of piston bowl geometry effects on the combustion [44, 45]. It has been observed that use of fuels such as E85 can increase the operating range of the RCCI engine. However, it also leads to increased HC and CO emissions at low loads due to the inherent low temperatures of the combustion process [43]. Natural Gas also has shown some good results. It has shown that the Natural Gas-RCCI engine can achieve 13.5 bar Indicated Mean Effective Pressure (IMEP) with no EGR with acceptable NOx and CO emissions [41].

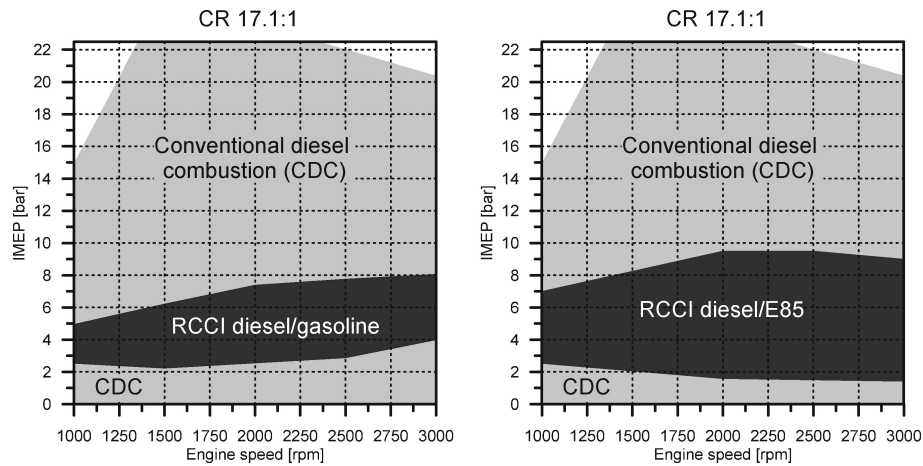


Figure 1.3: Gasoline-Diesel (left) vs Ethanol-Diesel (right) operating points [43]

Further studies by changing various parameters to increase combustion efficiency and decrease emissions have been done. Poorghasemi et al. [34] have shown that by

varying the amount of diesel fraction and the pressure and timing of the injections of fuel into the cylinder, the indicated efficiency and the emissions of the engine can be improved [34]. Li et al. have recently conducted simulation studies with a gasoline bio-diesel RCCI regime where they found that by varying the dwell of the injection of bio diesel could help mitigate MPRR and also reduce NO and soot emissions [36]. Mikulski et al. [35] have conducted simulation studies on the effect of directly injecting low reactivity fuel, in this case Natural Gas, into the cylinder. It was observed that there is potential for improvement of RCCI combustion efficiency, overall indicated efficiency and methane emissions in low load conditions. However, an increase in NO_x emissions has also been noted. Benajes et al. have also performed experimental studies that show that increase of efficiency in low loads is possible by increasing the in-cylinder fuel reactivity gradient and also that the EURO VI NO_x and soot emissions can be met along with a reduction in CO and HC emissions [37]. Pedrozo et al. have conducted experimental studies that have shown that the use of ethanol can increase the efficiency of the dual fuel operation beyond conventional diesel and that NO_x and soot emissions can be reduced significantly [38].

One of the major drivers for study in LTC regimes is the need to meet the emission standards. Simulation studies by Xu et al. have shown that a NG/Diesel engine with VVT can be optimized to meet Euro VI emission standards with little use of after treatment device for high loads [40]. Experimental studies by Benajes et al. have shown that RCCI strategy can be extended to operate over the entire engine

load speed range when combined with diffusive dual fuel strategies for combustion of gasoline-diesel [39]. The study showed that EURO VI emission standards can be achieved up until 14 bar IMEP reducing the need and use of after treatment systems. But, the same strategy has shown that although NO_x emissions are reduced drastically, the CO and HC emissions are higher [46]. The trend of studies is moving towards dual fuel combustion, using two different combustion strategies to achieve the load required. Both RCCI/CDC and RCCI/diffusive dual fuel combustion have been explored [39, 46, 47]. But, as noted above, both the strategies still suffer from high HC and CO emissions and need an after treatment system to reduce the emissions

1.2 RCCI control

RCCI has been the focus of research in LTC over the past few years. However, the number of studies in closed loop control of RCCI engines is not very high. For RCCI engines to become viable a robust controller is necessary. Even though RCCI offers better control over combustion phasing and Heat Release Rate (HRR), the number of actuators and sensors involved make it really hard and expensive for map-based control. It was also observed through simulation that the RCCI engine is sensitive to the injection timing of the fuel. Hence a precise control of injector is needed [45] which requires an understanding of the injector performance of both the port and direct injector. It is known that port injector systems are very dynamic [48, 49]

and their control can be achieved better with model based controllers. Hence, a control strategy that can handle the complexity of an RCCI engine control while being computationally light has to be designed to be used real time. In order to control the RCCI engine reliably in different conditions it is important to be able to control it during the transient states. This can be achieved effectively with a model-based controller.

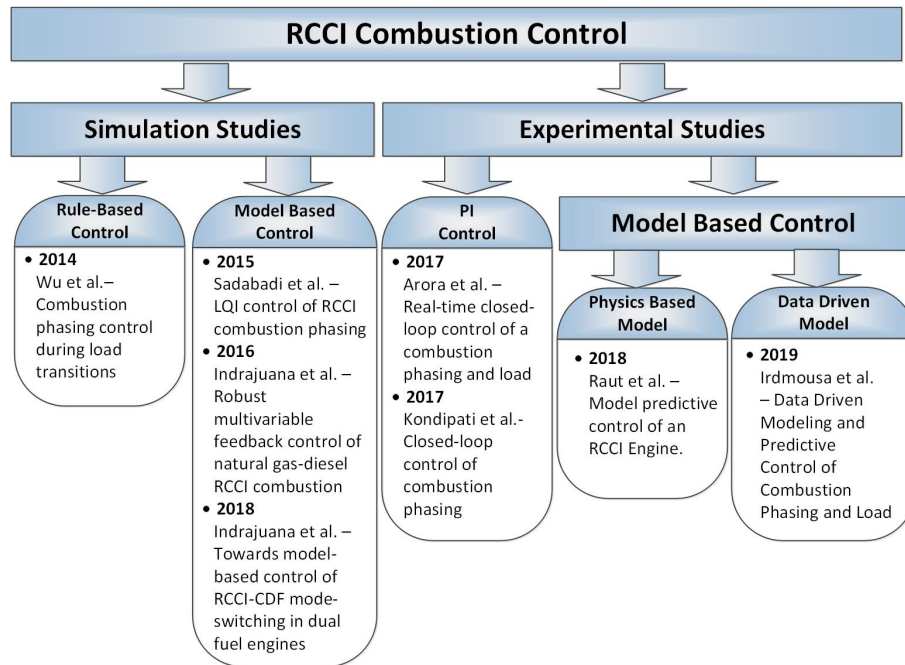


Figure 1.4: Prior work in RCCI control [1, 3, 4, 5, 50, 51, 52, 53]

Early studies into the control of RCCI engines did not involve model based control. Wu et al. had worked on a rule based strategy for control of the CA50 of an RCCI engine during load transients. To develop a control strategy, a CA50 vs PFI (Port Fuel Injection) ratio map was generated for different cycle numbers right after the transition from 1 bar to 4 bar IMEP and from 4 bar to 1 bar IMEP. This map was

then used to create a strategy for changing the PFI at the appropriate cycle after a change in IMEP was detected. This though gives an insight into how CA50 can be controlled, is not a very efficient solution since it is rule based and would require extensive experiments and tests to cover all operating points and conditions while capturing the transients.

Some model-based controllers have been developed in the recent years. Sadabadi et al. developed a physics based control oriented model (COM) which was validated with a CFD model simulation that was experimentally validated [1]. The COM uses a Modified Knock Integral Model (MKIM) to detect the start of combustion (SOC) of the mixture within the cylinder of an RCCI engine. The MKIM was modified from the Knock Integral Model which was developed by Livengood et al. [54] for detecting knock in SI engines. The MKIM was also used for detecting SOC in diesel and HCCI engines [55, 56]. The model was later augmented with the addition of modified Wiebe function to predict the CA50. This COM was then used as a plant model for an RCCI engine to develop an LQI controller to control CA50 using Premixed Ratio (PR). However, PR has slower response time, due to fuel transport dynamics [48], than SOI which can be a better control input for CA50 control. However, this study did not include the control of IMEP but provided a good base COM for further studies.

A study was undertaken by Kannan et al. [2] and later by Jayant et al. [53] to

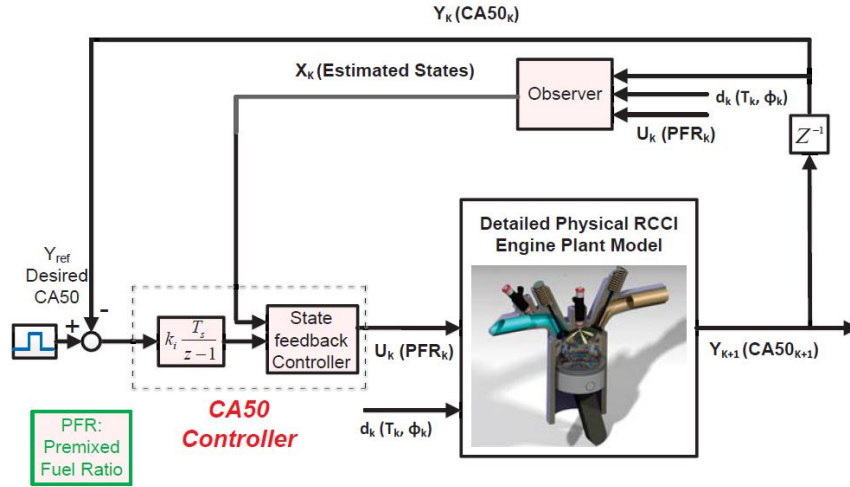


Figure 1.5: LQI controller implemented by Sadabadi et al. [1]

understand the effect of different control knobs on the combustion of RCCI engine and to develop a PI controller for control of CA50 and IMEP and mode switching with SI to improve operating range. A PI controller was then implemented for real time control of an RCCI engine. The implementation on the RCCI engine showed that there is cyclic variability and that it has to be addressed for smooth operation and consistent control as shown in Figure 1.6. Kondipati et al. [3] explored different control knobs for the control of combustion phasing. A sensitivity map was generated for CA50 vs SOI and PR. This was proposed to be used as a trigger for controlling CA50 using SOI or PR depending on the point of operation.

A dynamic model for fuel and air transport during transients was developed by Shahbakhti et al. [4, 48]. This model was used to augment the COM developed by Sadabadi et al. [4]. This COM was then used to develop controllers for control of

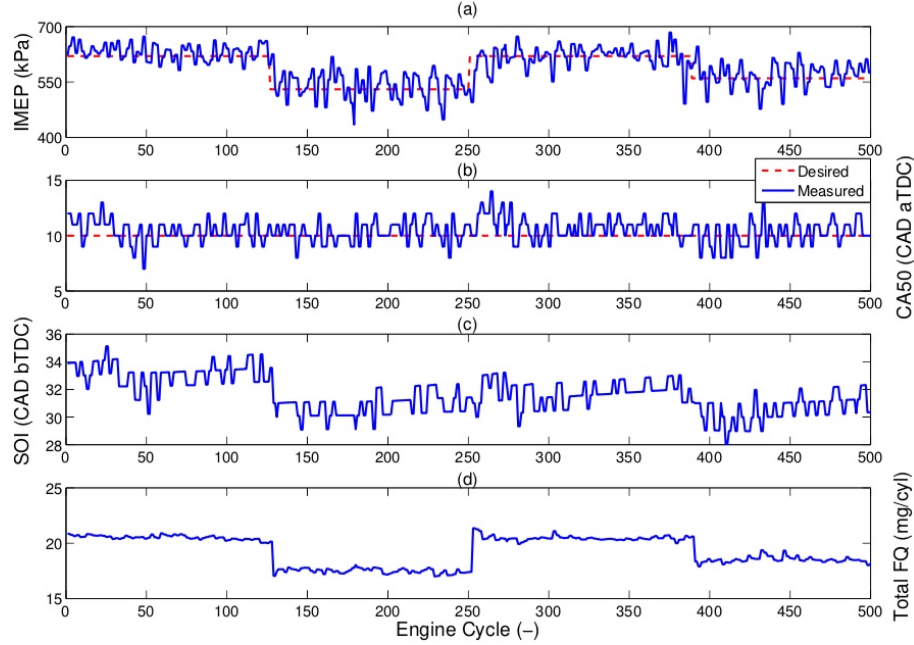


Figure 1.6: Feedback PI controller implemented by Arora et al. for real time control of RCCI engine [53]

CA50 and IMEP in an RCCI engine. Robust controllers including LQI and MPC controllers were implemented and experimentally validated by Akshat et al. [1, 4]. This work included the development of a sensitivity-based controller to use either the SOI or PR to control the CA50 of the engine. The authors have also worked on limiting Coefficient of Variance of IMEP (COV_{imep}) of one cylinder [57]. This is achieved by using engine maps for feed-forward values to find the optimal CA50 and PR to maintain a COV_{imep} less than 5%.

A multi zone chemical kinetics based detailed model was developed for predicting the combustion characteristics of an NG-Diesel RCCI engine [51, 58]. This model

implements a numerical analysis within a cylinder model which is divided into multiple zones concentrically. Each zone is initialized with its own species spread and these zones are coupled with heat and mass transfer. A total of 354 reactions involving 65 species are included in the model. The model is capable of predicting the pressure trace of the combustion as a function of CA degree and NOx emissions per cycle. This model was then experimentally validated [59] and Indrajana et al. [51] then linearized the model about an operating point and used that as a model for a multivariable feedback controller. The controller was assessed using simulation.

Recently a multi variable feedback controller for NG-Diesel RCCI engine was developed along with mode switching between RCCI and Conventional Dual Fuel (CDF) Combustion by Indrajana et al. [52]. This allows for improving the range of operation of the RCCI engine without using diesel combustion while meeting emissions standards. This controller also uses a COM that is a combination of the multi zone model by Bekdemir et al. discussed earlier and another dual zone model based on previous work [60, 61] for modeling the combustion in the dual fuel regime.

Even though controllers for RCCI engines have come a long way in terms of CA50 and IMEP control, there is still work to be done to achieve wide range of operation and safe and reliable performance.

1.3 Shortcomings of state of the art

Considering that limited amount of literature available on control of RCCI engines, there are still many areas for consideration of improvement. Some of them are listed below.

- † The controllers implemented only control CA50 and IMEP but not pressure rise rate while maintaining the COV_{imep} under 5%. The MPRR limits the load of the RCCI engine. By controlling the MPRR the load limit of the engine can be extended to reach higher loads. This active control of MPRR in RCCI engines has not been done before.
- † Most models and controllers that have been implemented work around an operating point and the others that work over a range of operating points have done that using scheduling [51, 57, 58]. This involves the tedious task of tuning the controller for different operating points and cannot be a viable option for controlling over a large range of operating points.
- † Owing to the highly non linear nature of RCCI dynamics, even the most robust controllers are not capable of operating over a large range of operating conditions.
- † More robust and comprehensive models are required to predict the behavior

of the RCCI engine over a wide range of operating points. In addition, this restricts the models from capturing the dynamics of the system between the linearized points or in transients.

† Stability of the controller is only given around the operating points about which the controller is tuned but not globally by design.

1.4 Objectives of this Thesis

The main objectives of this thesis are:

1. Develop a controller that can control CA50 and IMEP over a large operating range
2. Control CA50 and IMEP while limiting the MPRR to a pre-determined limit.

The first objective of control over a large operating range is accomplished by developing a Linear Parameter Varying (LPV) system. The second objective of controlling CA50 and IMEP while limiting MPRR is accomplished by modeling the MPRR during RCCI combustion, developing a Model Predictive Controller (MPC) using MPRR as a state and limiting the state of MPRR during the optimization of MPC.

1.5 Structure of this Thesis

In this thesis, a new model is developed for predicting the MPRR during RCCI combustion. The model is then validated with experimental data and then included into the existing Mean Value Model (MVM) for predicting MPRR cycle by cycle. This MVM is then used to develop an Linear Parameter Varying (LPV) system that is accurate over a large range of operating conditions. The MVM is then used to develop an MPC using the LPV system developed. The MPC is used to control the CA50 and IMEP while limiting the MPRR to a pre-determined value. The organization of the thesis is shown in Fig. 1.7

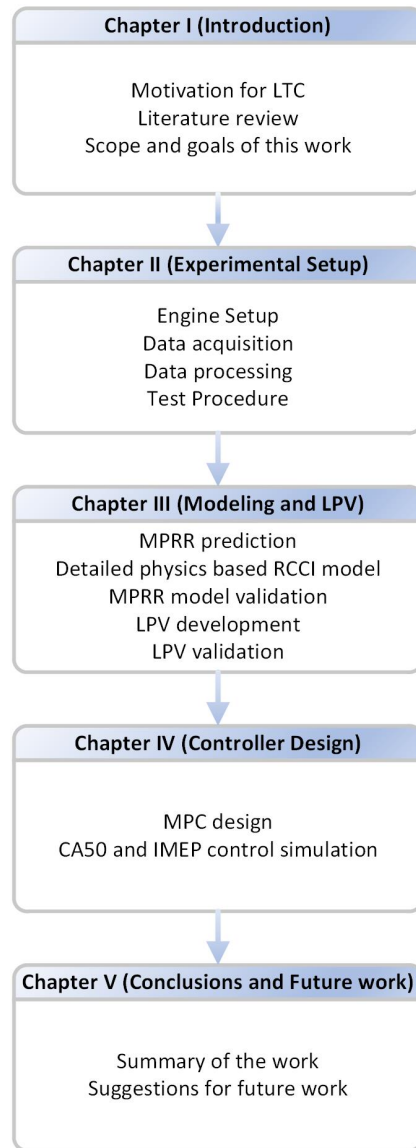


Figure 1.7: Thesis organization

Chapter 2

Experimental setup and Analysis

This chapter describes the experimental setup and analysis used to conduct the experiments. The following sections will describe the engine specifications, Modifications made for RCCI operation, Data acquisition setup, Test procedure and the uncertainty analysis.

2.1 Engine specifications

The Energy and Mechatronics Laboratory (EML) uses 2.0L GM Ecotec engine at the Advanced Propulsion Systems (APS) Research Center for studying RCCI combustion. The engine has been used for Homogenous Charge Compression Ignition (HCCI)

and Partially Premixed Charge Compression Ignition (PPCI) research during earlier studies [2]. Though the engine is capable of turbocharging, no boost was used for the experiments presented in the data here. All the experiments were conducted at NA conditions. The intake and exhaust valves were set for a Negative Valve Overlap (NVO). The engine specifications are shown in Table 2.1

Table 2.1
Engine Specifications

Make	General Motors
Model	Ecotec 2.0 L Turbocharged
Engine Type	4 stroke, Gasoline
Fuel System	Direct Injection
No of Cylinders	4 cylinders
Displaced Volume	1998 [cc]
Bore	86 [mm]
Stroke	86 [mm]
Compression Ratio	9.2:1
Max Engine Power	164 @ 5300 [KW@rpm]
Max engine torque	353 @ 2400 [Nm@rpm]
Firing order	1-3-4-2
IVO	25.5/-24.5 [°CAD bTDC]
IVC	2/-48 [°CAD bBDC]
EVO	36/-14 [°CAD bBDC]
EVC	22/-28 [°CAD bTDC]
Valve lift	10.3 [mm]

2.2 Modifications made for RCCI operation

The stock engine works on Gasoline Direct Injection (GDI) and was designed to inject only one fuel. This has been modified by the addition of two PFI rails to enable dual

fuel operation. The two PFI rails added were used primarily for in-cylinder fuel blending during HCCI operation. In this work only one of the PFI rails was used for delivery of the low reactivity fuel. The PFI injectors and DI injectors have been calibrated during previous studies for the fuels used in this work [2, 3]. Two air heaters have been added upstream of the PFI injectors to control the temperature of the intake air. The schematic for the engine is shown in Figure 2.1

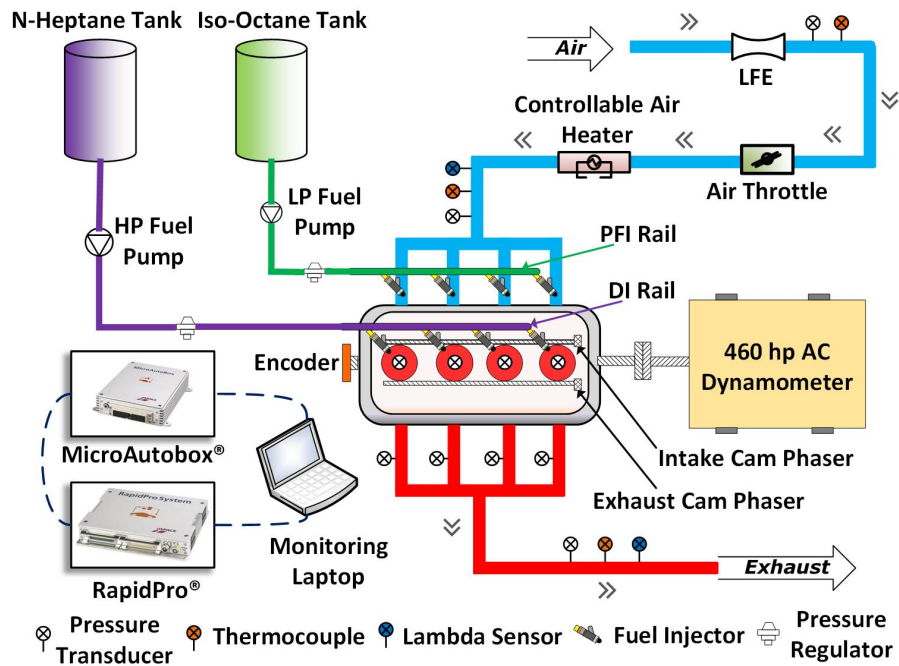


Figure 2.1: LTC Engine setup [4]

The two fuels used in this work are n-heptane and iso-octane as the low reactivity fuel and high reactivity fuel respectively. The specifications of these fuels are shown in Table 2.2

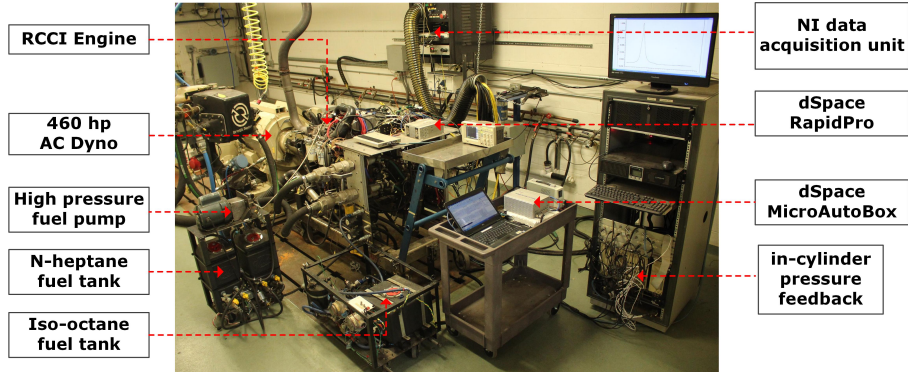


Figure 2.2: Experimental setup

Property	n-heptane	iso-octane
Higher Heating Value [MJ/Kg]	48.07	47.77
Lower Heating Value [MJ/kg]	44.56	44.30
Density [Kg/m ³]	686.6	693.8
Octane Number [-]	0	100
H/C ratio [-]	2.29	2.25

Table 2.2
Fuel Specifications

2.3 Data Acquisition

The engine requires a group of sensors for collecting and processing the parameters of operation of the engine and the combustion inside the combustion chamber. This is achieved by a combination of three systems including NI LabView, dSPACE and ACAP Combustion analyzer. The NI LabView system is responsible for controlling the dynamometer and the temperature of the intake air. It also collects temperatures at various points on the engine such as oil, coolant, exhaust etc., which are used for monitoring purposes. The ACAP Combustion Analyzer is used

to collect and process the pressure traces collected from the engine cylinders. This engine is equipped with piezo electric pressure transducers (115A04 transducer from PCB Piezotronics) inside each cylinder to collect the pressure trace from each of the cylinders. The methodology used for processing the pressure trace has been presented by N. Kondipati [3]. The third system used is the dSPACE system which is primarily used for controlling the actuators such as injectors, spark plugs, EGR valve etc. A Field Programmable Gate Array (FPGA) has been used to perform the calculations presented in [3]. These calculations are then fed to the dSPACE MABX which has a slave controller, RapidPro communicating via CAN. RapidPro is capable of controlling various actuators such as the PFI, DI, spark plugs, throttle body etc. The MABX and the RapidPro in conjunction control the engine on a cycle to cycle based on the real time combustion parameters such as CA50 and IMEP calculated by the FPGA. The engine is equipped with a crank sensor (Encoder Products - Model 260) with a resolution of 1 Crank Angle Degree (CAD). This crank sensor was used to calculate the current crank position and the RPM. An overview schematic of the data acquisition and control setup is shown in Figure 2.3

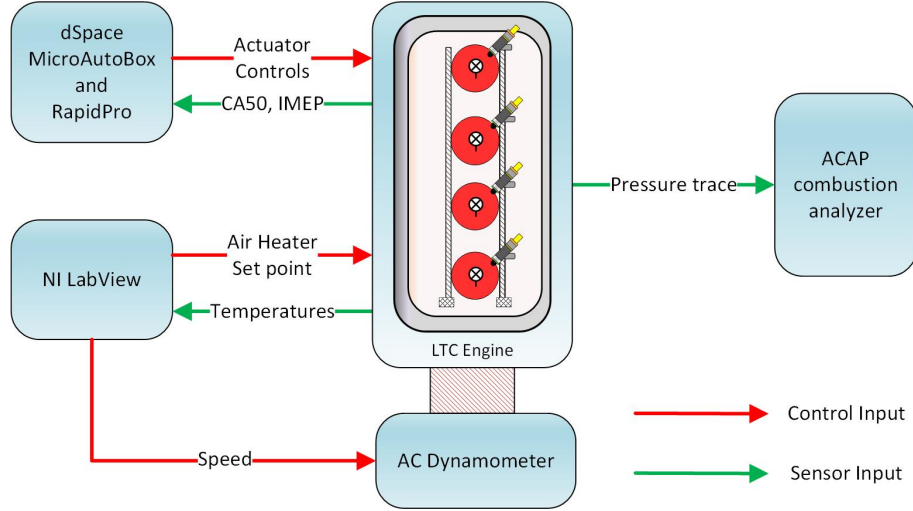


Figure 2.3: Data acquisition setup

2.4 Test Procedure

Multiple test runs were conducted to collect data about RCCI combustion to help developing the Mean Value model (MVM) to be discussed in Chapter 3. The data for these tests was collected using ACAP data acquisition software. There are three main parameters that were varied between the test runs, SOI, Fuel Quantity and Premixed Ratio (PR). PR is the ratio of the energy of the low reactivity fuel to that of the energy of the total fuel. In this case the low reactivity fuel is iso-octane. The PR is calculated using the Eq (2.1):

$$PR = \frac{LHV_{iso} * mf_{iso}}{LHV_{iso} * mf_{iso} + LHV_{nhcp} * mf_{nhcp}} \quad (2.1)$$

where, LHV_{iso} and LHV_{nhep} are the Lower Heating Values of the iso-octane and n-heptane respectively, $m_{f_{iso}}$ and $m_{f_{nhep}}$ are the mass of fuel of iso-octane and nheptane respectively.

The high reactivity fuel, n-heptane is injected via the DI rail while the low reactivity fuel, iso-octane is injected via one of the PFI rails. The compression ratio of the engine was low for cold starting the RCCI engine and hence SI mode was first used to bring the engine up to temperature.

Once at temperature, the engine was switched to RCCI operation using the dSPACE MBAX controller. In RCCI mode, the amount of n-heptane and iso-octane was regulated via PR. For the purpose of parameterizing and validating the MVM, the engine was run in steady state and transient conditions. The data collected under steady state operation was used to parameterize the MVM. Each test was run for 100 cycles. Any data points with over 5% COV_{IMEP} were not considered. The intake temperature was fixed at 60° C. The total Fuel Quantity (FQ) was swept at every SOI and PR step. The operating points collected for the tests are shown in Table 2.3.

Table 2.3
RCCI Test Conditions

SOI [$^{\circ}$ CAD bTDC]	PR [-]	FQ [mg/cycle]
60	10	17 - 21
	20	17 - 21
	30	19 - 23
50	10	17 - 23
	20	17 - 23
	30	19 - 25
45	30	19 - 25
	35	19 - 23
	60	19 - 28
40	10	17 - 23
	20	17 - 23
	40	14 - 28
35	20	10 - 28
	60	19.8 - 29
30	40	13 - 28
	60	18 - 28
25	20	9 - 27
	40	11 - 27
20	20	10 - 26

2.5 Uncertainty Analysis for Measured and Derived Parameters

The apparatus used for measuring various parameters are limited in accuracy. This leads to the propagation of those inaccuracies into the derived parameters that are calculated. Hence, it is important to measure the uncertainty in each of these parameters before making conclusions based on them. The uncertainty in the measured

parameters is presented in Table 2.4.

Table 2.4
Measured parameters and their uncertainties

Parameter [Units]	Value	Uncertainty (\pm)
Bore [m]	0.086	0.001
Stroke [m]	0.086	0.001
Length [m]	0.086	0.001
Cylinder Pressure [KPa]	95 - 4000	1%
Crank Angle [CAD]	0 - 720	1
λ [-]	1.0 - 3.0	0.05
T_{in}	4 - 100	2%
N [rpm]	800 - 2200	10
m_{air} [g/s]	12.1 - 31.0	0.72%
m_{fuel} [mg/cycle]	11.0 - 40.0	0.1%
P_{in} [KPa]	95 - 105	0.5%
$T_{exhaust}$ [<i>circ</i> C]	350 - 700	2%

The derived parameters uncertainties are calculated using Eq (2.2).

$$U_y = \sqrt{\sum_i \left(\frac{\partial Y}{\partial X_i} \right)^2 U_{X_i}^2} \quad (2.2)$$

Y is the derived parameter while X is the measured parameter. U_y is the uncertainty in the derived parameter while U_x is the uncertainty in the measured parameter.

The uncertainties of the derived parameters are shown in Table 2.5

Table 2.5
Derived parameters and their uncertainties

Parameter [Units]	Value \pm Uncertainty
BD [$^{\circ}$ CAD]	6 ± 1
CA50 [$^{\circ}$ CAD aTDC]	-1 ± 1
IMEP [KPa]	540.7 ± 28.1

2.6 Maximum Pressure Rise Rate calculation

For modeling the Maximum Pressure Rise Rate (MPRR), it is important to have experimental data to validate it against. This experimental data comes from the pressure trace that was collecting using the pressure transducers on the engine as mentioned in section (2.3). The pressure transducers are capable of measuring in the range of 0-3500 PSI and have a sensitivity of 1.442 pC/PSI. The electric charge from the piezo electric modules are amplified to a proportional voltage signal using a charge amplifier. However, the pressure transducers measure the relative pressure and hence need a reference. This process of giving the reference pressure to the pressure transducer is called pegging. In this case, the manifold pressure is the best reference for the transducer. Hence, it is pegged with the MAP signal. So when the pressure transducer measures a certain value it subtracts the value of the MAP signal to give an absolute measurement. This pressure signal is taken at an interval with the crank angle. This interval of crank angle determines the accuracy of the combustion parameters that are to be calculated from this pressure trace. In this setup, the signal

is taken at every 1 CAD.

However, the pressure trace that is collected from the pressure transducer is not entirely usable. It is important to get rid of any noise that comes with the signal [62]. For this purpose, it is important to filter the signal and average it over multiple cycles to remove any noise. Based on the previous work done on the same setup [3], a Butterworth low pass filter with a cutoff frequency of 0.5 and order 1 was deemed appropriate.

Once the pressure trace was conditioned and filtered, the MPRR has to be calculated. At each data point (combination of SOI, FQ and PR), 100 cycles of combustion were recorded. The pressure rise rate was calculated using the following equation.

$$\left(\frac{dP}{d\theta}\right)_i = \frac{P_{i+1} - P_i}{\Delta\theta} \quad (2.3)$$

$\Delta\theta$ in Eq. (2.3) is 1 CAD as the pressure trace is collected with an interval of 1 CAD.

2.7 Coefficient Of Variance of IMEP

In order to analyze the various combustion parameters, it is important to understand if the combustion was stable or not. A common metric for understanding combustion

stability is the COV_{IMEP} [63]. It quantifies the variation in the IMEP. For this study any experimental data with COV_{IMEP} greater than 5% is considered unstable and was not used for analysis.

To calculate the COV_{IMEP} , the IMEP should be calculated first. In this study, the IMEP is calculated using the gross work per cycle ($W_{c,ig}$) where c indicates that the work done is per cycle. The gross work per cycle includes the work delivered to the piston over the compression and expansion strokes and excludes the pumping losses [64]. The equation shown in Eq. (2.4) is used to calculate the IMEP per cycle.

$$IMEP_c = \frac{W_{c,ig}}{V_d} \quad (2.4)$$

V_d in the Eq. (2.4) is the displaced volume. The IMEP is averaged over n cycles to calculate the mean value as shown in Eq. (2.5).

$$IMEP = \frac{\sum_{c=1}^n IMEP_c}{n} \quad (2.5)$$

where, n in this study is 100. The COV_{IMEP} is then calculated using the Eq. (2.6) where σ_{IMEP} is the standard deviation of IMEP over the n cycles.

$$COV_{IMEP} = \frac{\sigma_{IMEP}}{IMEP} \quad (2.6)$$

2.8 Experimental data analysis

The Fig. 2.4 shows how MPRR varies with the input parameters, SOI, FQ and PR. The vertical range at each data point represents the range of MPRR over 100 cycles at that operating point. It can be seen that with early injections such as 60 CAD bTDC (Fig. 2.4(c)) and 50 CAD bTDC (Fig. 2.4(b)), MPRR has a near linear relationship with FQ. Also, there is not much variation between the different PR values considering the cyclic variability. However, with later injection, 40 CAD bTDC (Fig. 2.4(a)) the MPRR vs FQ relationship is no longer linear. The relationship between MPRR and FQ also changes with PR.

This suggests that there are different regimes of combustion. With earlier injections, the DI fuel gets time to mix well and form a homogeneous mixture with the PFI fuel and air. This leads to very rapid combustion with a short burn duration. The MPRR for a given PR value keeps increasing as the SOI advances. This further supports the argument that with advanced SOI, the in-cylinder mixture is more homogeneous and thus leads to high MPRR.

As the SOI is retarded, the mixture is not homogeneous anymore but is stratified.

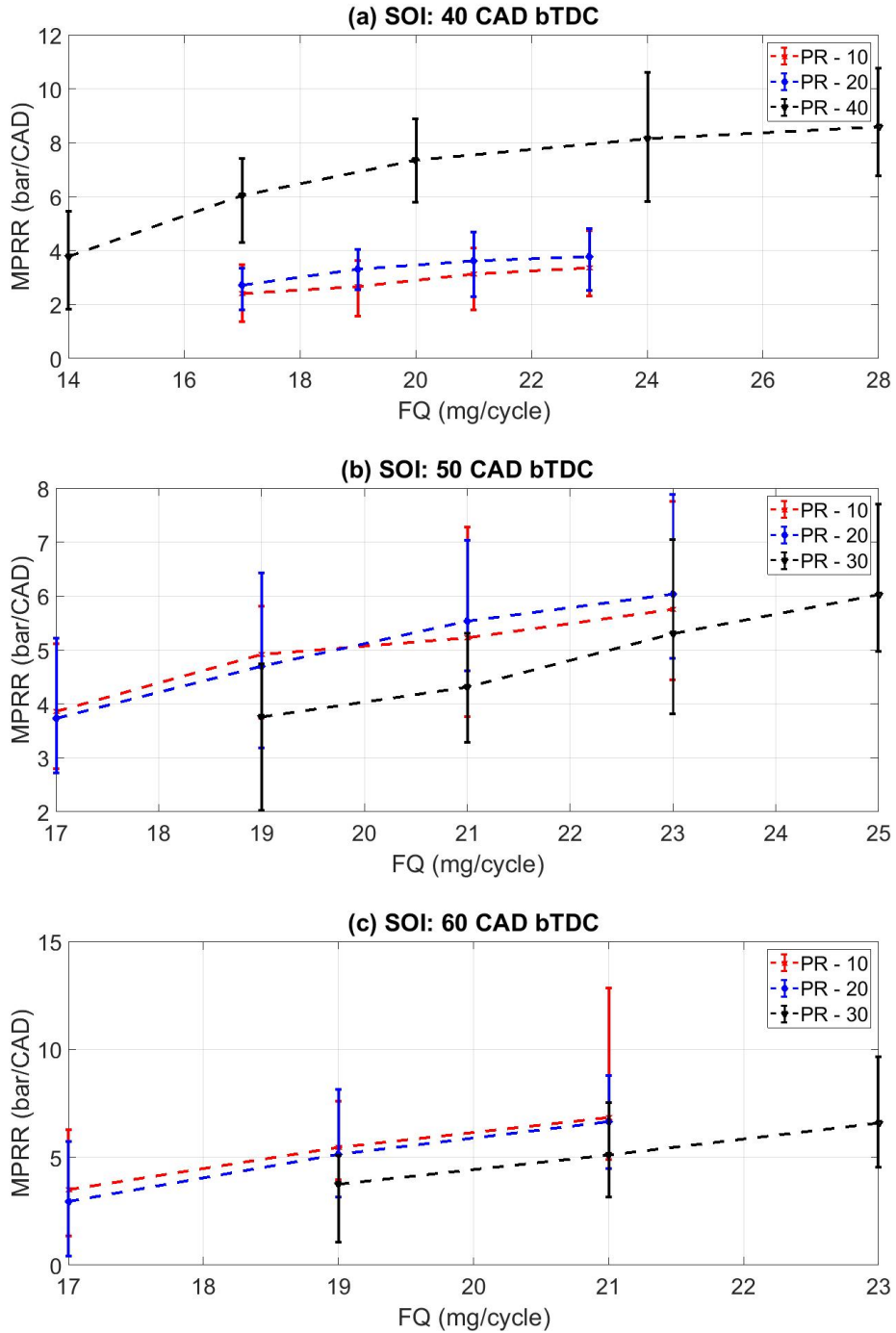


Figure 2.4: Variations of MPRR as a function of SOI, FQ and PR. (a) $N = 1000$, $T_{in} = 60^\circ$, SOI = 40 CAD bTDC, (b) $N = 1000$, $T_{in} = 60^\circ$, SOI = 50 CAD bTDC, (c) $N = 1000$, $T_{in} = 60^\circ$, SOI = 60 CAD bTDC

The DI fuel does not get enough time to mix with air and the PFI fuel. This leads to local high equivalence ratios and a longer burn duration. The combustion in this case is not as short and rapid as when there is a homogeneous mixture. In addition, due to stratification of the in-cylinder mixture, PR and FQ become dominant parameters because they affect the nature and amount of stratification within the cylinder. Hence, as the SOI retards, MPRR is affected strongly by PR and FQ.

The Fig. 2.5 represents the variation in MPRR with respect to the input parameters. It can be noted that the standard deviation of MPRR increases with earlier injection of the DI fuel, higher PR and with higher quantity of fuel.

With higher PR, the amount of low reactivity fuel increases in the mixture leading to relatively unstable combustion. It can be seen in Fig. 2.5(b) that for data points with high PR, the COV_{imep} is also higher. This instability in combustion leads to higher variation in the MPRR.

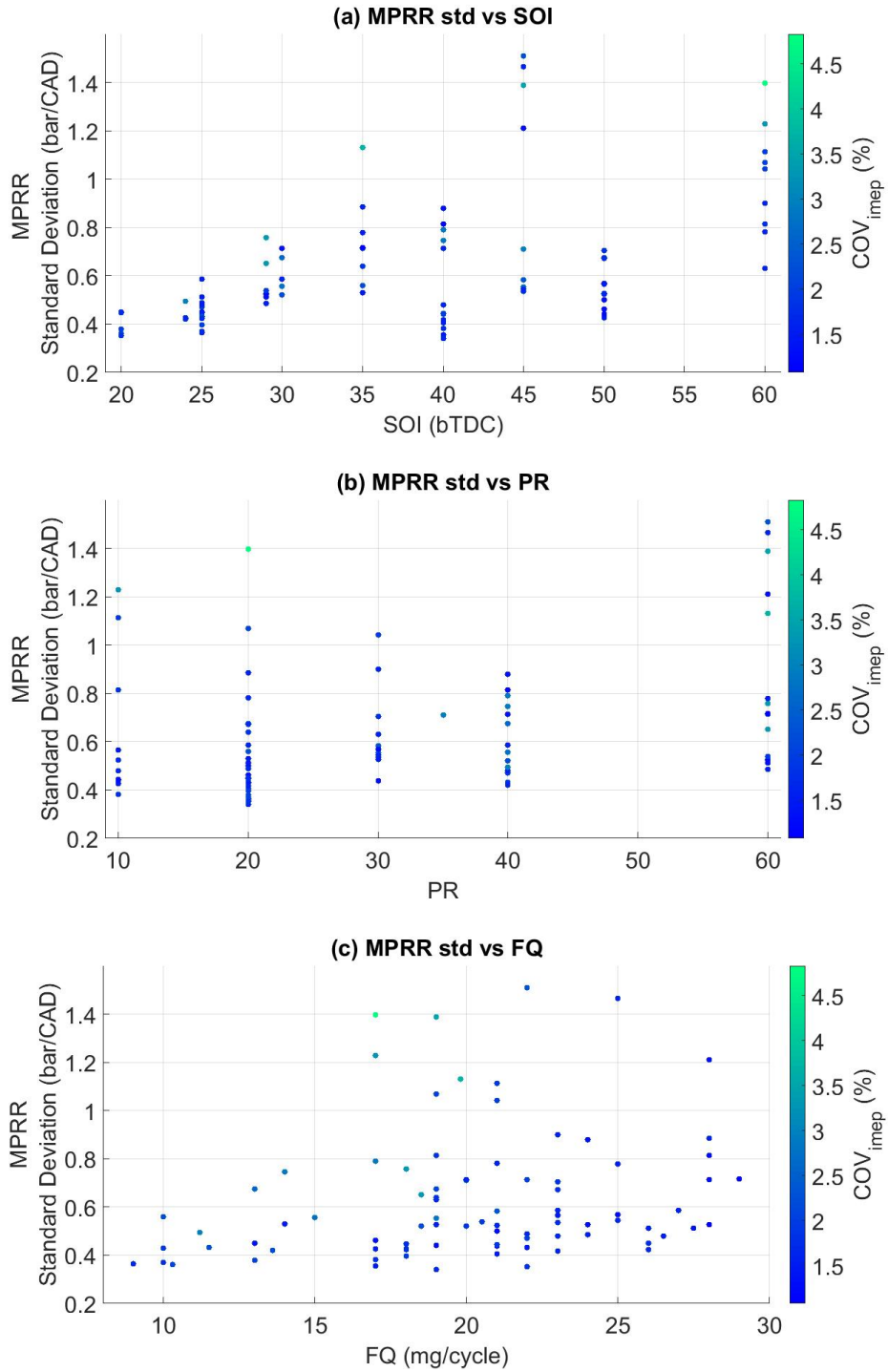


Figure 2.5: Standard deviation of MPRR for 87 data points as shown in Table 2.3. SOI: 20 - 60 (CAD bTDC); PR: 10 - 60 (-); FQ: 9 - 29 (mg/cycle). Standard deviation is calculated over 100 cycles for each data point.

Chapter 3

Dynamic model for RCCI combustion

3.1 Introduction

A computationally efficient and reliable plant model is required for real time model based control of combustion phasing and load. This plant model should be able to calculate various parameters that are of interest and the intermediate parameters accurately to be able to use for feedback control. Many plant models have been developed in the past for engines. Two common types of models include CFD [65, 66, 67] and Control Oriented Models (COM)[1, 58]. CFD plant models can be very

accurate, however, they are also very computationally expensive. Hence, they cannot be used as plant models for real time feedback controls. However, COMs as the name suggests are Control Oriented and hence are computationally light. They are not as extensive as the CFD models but can be developed to be accurate enough for the parameters of interest. In this work, the aim is to develop a model for predicting the MPRR on a cycle by cycle basis in order to be used as a COM for controlling CA50 and IMEP while limiting the MPRR.

A popular approach to model MPRR is to reconstruct the pressure trace which then allows for calculating the pressure rise rate [68, 69, 70]. In order to reconstruct the pressure trace, Wiebe function is widely used to model the MFB and the Woschni model is used for the heat transfer to the walls [68, 69, 71, 72, 73]. However, the modified Woschni model developed by Chang et. al [74] has been used in LTC combustion regimes.

This work expands on the methods used for pressure trace reconstruction in traditional ICE and apply it to RCCI combustion. It uses a Wiebe function along with the modified Woschni correlation to develop a MVM to predict the MPRR in steady state conditions. This MVM is then included with physics based equations to include the transient dynamics. This chapter also includes the models used for predicting SOC, CA50 and IMEP while accounting for the transients of residual gas fractions. This model is then linearized and developed into an LPV system using a machine

learning technique [6]. The following sections explain the development of the MPRR model and the rest of physics based dynamic model and the LPV development.

3.2 SOC model

The Start of Combustion (SOC) is predicted using a Modified version of the Knock Integral Model (KIM) developed by Livengood et al. [54] for detecting knock in SI engines. It was modified by Shahbakhti and Koch [56] to predict the SOC in HCCI engines. Later, Sadabadi [1] had modified it to work with RCCI combustion. The initial idea with KIM was that the ignition would happen when the significant species reached a certain critical value. Since, this was initially developed by Livengood for SI engines where the fuel is injected along with the air, there was only 1 stage of integration. However, in an RCCI setup, the Modified Knock Integral Model (MKIM) requires two stages as the DI fuel, n-heptane, is injected after Intake valve Closing (IVC). The MKIM is shown in Eq. (3.1). The first stage is from the IVC to SOI which represents the compression of the PFI fuel, iso-Octane, and the second stage represents the compression of the mixture of both the high reactivity (n-heptane) and the low reactivity (iso-Octane) fuels.

$$\int_{SOI}^{SOC} \frac{d\theta}{A_2 N (\phi_{DI}^{B_{2DI}} + \phi_{PFI}^{B_{2PFI}}) \exp\left(\frac{C_2}{CN_{mix} + b} (P_{IVC} v_c^{n_c})^D\right)} + \int_{IVC}^{SOI} \frac{d\theta}{A_1 N \phi_{PFI}^B \exp\left(\frac{C_1 (P_{IVC} v_c^{n_c})^{D_1}}{T_{IVC} v_c^{n_c - 1}}\right)} = 1 \quad (3.1)$$

where, N is engine speed, ϕ_{di} and ϕ_{pfi} are the equivalence ratios of the DI and PFI injected fuels which are calculated using Eq. (3.2) and Eq. (3.3) where ϕ_{tot} is the global combined equivalence ratio. CN_{mix} is the Cetane Number of the mixture which is represented with the Eq. (3.4) where FAR_{st} is the stoichiometric fuel-air ratio of the respective fuel and CN is the cetane number of the respective fuel. n_c is the polytropic coefficient which is calculated using the slope of the compression stroke on the PV diagram. v_c is the ratio of the volume at IVC to volume at any given crank angle θ as shown in the Eq. (3.5). The P_{IVC} and T_{IVC} are the pressure and temperature at IVC. Since the IVC happens 2 CAD before BDC, the conditions at IVC are considered to be equal to that of the manifold.

$$\phi_{di} = (1 - PR) \cdot \phi_{tot} \quad (3.2)$$

$$\phi_{pfi} = PR \cdot \phi_{tot} \quad (3.3)$$

$$CN_{mix} = \frac{FAR_{st,nhep} \phi_{di} CN_{nhep} + FAR_{st,iso} \phi_{PFI} CN_{iso}}{FAR_{st,nhep} \phi_{DI} + FAR_{st,iso} \phi_{PFI}} \quad (3.4)$$

$$v_c = \frac{V_{IVC}}{V(\theta)} \quad (3.5)$$

The constants in Eq. (3.1) are $A_1, A_2, B, B_{2DI}, B_{2PFI}, b, C_1, C_2, D_1$ and D_2 which are to be parametrized. The optimized parameters used in this work are given in Table 3.1

A_1	B	C_1	D_1	A_2
0.5366	-0.0072	5.2104	-0.0002	0.0024
B_{2DI}	B_{2PFI}	C_2	b	D_2
0.0016	7.3403e-05	1512.17e+03	174.24	-0.2374

Table 3.1
Optimized parameters for MKIM

3.3 Maximum Pressure Rise Rate modeling

3.3.1 Introduction

For the safe operation of an engine operation, it is important to keep the MPRR under safe limit of the engine. High MPRR can lead to physical damage to the engine. Especially, in RCCI combustion where the burn duration can be short, leading to sharp rises in the pressure. Hence, it is important to model and control the MPRR in order to safely operate the engine while reaching the desired CA50 and IMEP targets.

$$\frac{dQ}{d\theta} = \frac{\gamma}{\gamma - 1} \cdot P \frac{dV}{d\theta} + \frac{1}{\gamma - 1} V \frac{dP}{d\theta} + \frac{dQ_w}{d\theta} \quad (3.6)$$

where $\frac{dQ}{d\theta}$ is the rate of heat release, γ is the adiabatic coefficient of compression, P is the instantaneous pressure, V is the instantaneous volume and $\frac{dQ_w}{d\theta}$ is the heat transfer to the wall.

Pressure rise rate has been modeled in the past using the heat release equation as shown in Eq. (3.6) [68, 69, 70]. This equation can be re arranged to calculate the pressure rise rate as shown in Eq.(3.7):

$$\frac{dP}{d\theta} = \frac{\gamma - 1}{V} \left(\frac{dQ}{d\theta} - \frac{dQ_w}{d\theta} \right) - \frac{\gamma P}{V} \cdot \frac{dV}{d\theta} \quad (3.7)$$

The first term on the right hand side of Eq. (3.7) represents the heat release from the fuel. This term is modelled using the Wiebe function. The Wiebe function models the rate of burn of the fuel. The Wiebe function combined with the LHV of the fuels is used to calculate the heat release form the fuel as shown in Eq. (3.8).

$$\frac{dQ}{d\theta} = LHV_{eff} \frac{m}{\alpha \Delta\theta} \left(\frac{\theta - \theta_{soc}}{\Delta\theta} \right)^{(m-1)} \exp \left[- \left(\frac{\theta - \theta_{soc}}{\alpha \Delta\theta} \right)^m \right] \quad (3.8)$$

where LHV_{eff} is the effective Lower Heating Value, m is the shape factor, $\Delta\theta$ is the

burn duration, α is the scaling factor, θ_{soc} is the crank angle at SOC and θ is the instantaneous crank angle. The LHV_{eff} is calculated using Eq. (3.9).

$$LHV_{eff} = (1 - PR).LHV_{DI} + PR.LHV_{PFI} \quad (3.9)$$

where LHV_{DI} is the Lower Heating Value of the DI injected fuel, in this case, n-heptane and LHV_{PFI} is the Lower Heating Value of the PFI injected fuel, in this case Iso-Octane.

The second term on the right hand side in Eq. (3.7) represents the heat loss to the wall. It is modeled using the modified Woschni Model for LTC engines. It is shown in Eq. (3.10) [74]:

$$\frac{dQ_w}{d\theta} = \frac{h_c \cdot A_c \cdot (T_g - T_w)}{6 \cdot N} \quad (3.10)$$

where, N is the engine speed, A_c is the in-cylinder surface area, T_g and T_w are the gas temperature and the wall temperature, respectively. h_c is the heat transfer coefficient which is calculated based on the Eq. (3.11) and Eq. (3.12).

$$h_c(t) = 3.4.H(t)^{(-0.2)}.P(t)^{(0.8)}.T(t)^{(-0.73)}.\omega(t)^{(0.8)} \quad (3.11)$$

$$\omega(t) = C_1 \cdot S_p + \frac{C_2 \cdot V_d \cdot T_{IVC}}{6 \cdot P_{IVC} V_{IVC}} (P(t) - P_{mot}(t)) \quad (3.12)$$

where, $H(t)$ is the instantaneous cylinder height, $P(t)$ is in-cylinder pressure and $T(t)$ is the in-cylinder gas temperature as a function of time. S_p is the average piston speed and P_{mot} is the motoring pressure as a function of time. C_1 and C_2 are constants.

The third term on the right hand side in Eq. (3.7) comes from the instantaneous pressure and volume. Volume as a function of the crank angle θ can be represented using Eq. (3.13)

$$V(\theta) = V_c + \frac{\Pi D^2}{4} \cdot (l + r - r \cdot \cos\theta - \sqrt{l^2 - (r \cdot \sin\theta)^2}) \quad (3.13)$$

where, D is the bore diameter, l is the length of the connecting rod, r is the radius of the crank and V_c is the clearance volume.

The Eq. (3.7) is computed at every crank angle from SOC to EOC. The SOC is calculated using the MKIM adapted for RCCI combustion [1]. At SOC, the instantaneous P and V values are initialized to P_{soc} and V_{soc} . MPRR is the maximum value of the pressure rise rate from SOC to EOC.

3.3.2 Double Wiebe vs Single Wiebe function

As introduced in Section 3.3.1 a Wiebe function is required to model the heat release from the fuel. There are two types of Wiebe function, Single and Double Wiebe functions which are shown in Eq. (3.14) [75] and Eq. (3.15) respectively.

$$X_b(\theta) = 1 - \exp \left[- \left(\frac{\theta - \theta_{soc}}{\alpha \Delta \theta} \right)^m \right] \quad (3.14)$$

$$X_b(\theta) = p * \left[1 - \exp \left[- \left(\frac{\theta - \theta_{soc}}{\alpha_1 \Delta \theta_1} \right)^{m_1} \right] \right] + (1 - p) * \left[1 - \exp \left[- \left(\frac{\theta - \theta_{soc}}{\alpha_2 \Delta \theta_2} \right)^{m_2} \right] \right] \quad (3.15)$$

where θ_{soc} is the CAD at SOC, $\Delta\theta$ is the burn duration, α is a scaling factor based on the extent of burn considered (such as 10% to 90%) and m is a constant that determines the shape of the mass fraction burn. For a double Wiebe function, p ($0 < p < 1$) is a weighing factor between the two terms. Each term has its own $\alpha, \Delta\theta, \theta_{soc}$ and m .

The double Wiebe function is largely favored for pressure reconstruction [68, 71, 72].

However, as shown in Fig 3.1(b), the MPRR predicted using the a double Wiebe function which is highly inaccurate in the later stages of the MFB is not different from the MPRR predicted with an accurate double Wiebe function. This is largely because the MPRR occurs somewhere between the SOC and the point of peak pressure. The pressure trace after that is only decreasing. Hence, a single Wiebe function which is accurate in the region from SOC to peak pressure would be sufficient for the purpose of predicting the MPRR.

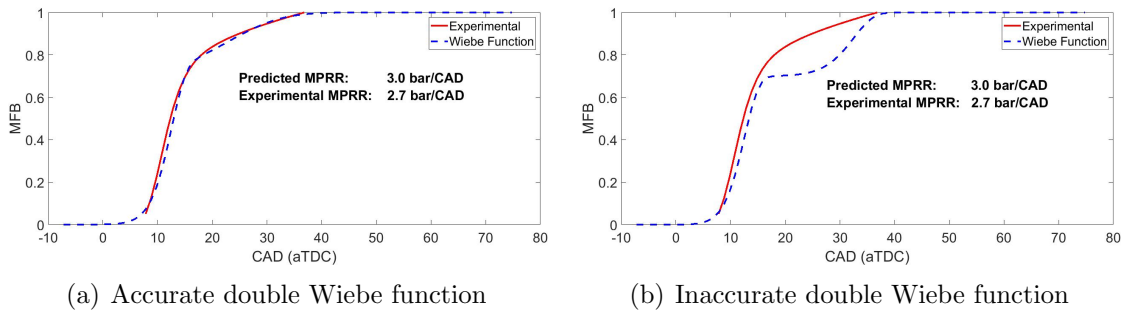


Figure 3.1: Effect of double Wiebe function accuracy on MPRR prediction, FQ = 17 mg/cycle, SOI = 40 bTDC, PR = 20

3.3.3 Parametrization of Single Wiebe function

To parametrize and validate the Wiebe function, 80 data points were used. 65% of these points, i.e. 52 data points were used to parametrize the Wiebe function while the rest 35%, i.e. 28 data points were used to validate the Wiebe function. The operating conditions are shown in Table 3.2.

Table 3.2
Operating conditions for parametrization and validation of the Wiebe function

Parameter [Units]	Operating point
PR [-]	10-20-30-40-50-60
SOI [$^{\circ}$ CAD bTDC]	10-15-20-30-40-50-60
T_{in} [circ C]	60
Λ [-]	2.5-10
P_{in} [KPa]	96.5
IVO [circ CAD bTDC]	25.5
EVC [circ CAD bTDC]	22
Speed [RPM]	1000

A Wiebe function as shown in Eq. (3.14) has three parameters that need to be parameterized, θ_{soc} , $\Delta\theta$ and m . θ_{soc} is predicted using the MKIM which is described in Section 3.2. $\Delta\theta$ and m are parameterized as shown in Eq. (3.16) and Eq. (3.17).

$$\Delta\theta = C_1 + K(C_2 \cdot \phi_{di} + C_3 \cdot \phi_{phi} + C_4 \cdot SOI + C_5) + C_4 \cdot SOI \quad (3.16)$$

$$m = C'_1 + C'_2 \cdot (1 + K) \cdot SOI + C'_3 \cdot K \quad (3.17)$$

$$K = \exp[-(SOI - C_6)^{C_7}] \quad (3.18)$$

where $C_1, C_2, C_3, C_4, C_5, C_6, C_7, C'_1, C'_2$ and C'_3 are constants that are parametrized.

The parametrized values are shown in Table 3.3.

The results of the 52 data points is shown in Fig. 3.2. The vertical range at each experimental data point represents the range of MPRR over 100 cycles. The mean of

Table 3.3
Optimized parameters for MPRR model

C_1	C_2	C_3	C_4	C_5	C_6	C_7	C'_1	C'_2	C'_3
29.00	-29.07	-15.75	-0.40	-1.77	60.00	2.00	1.298	-0.0012	0.202

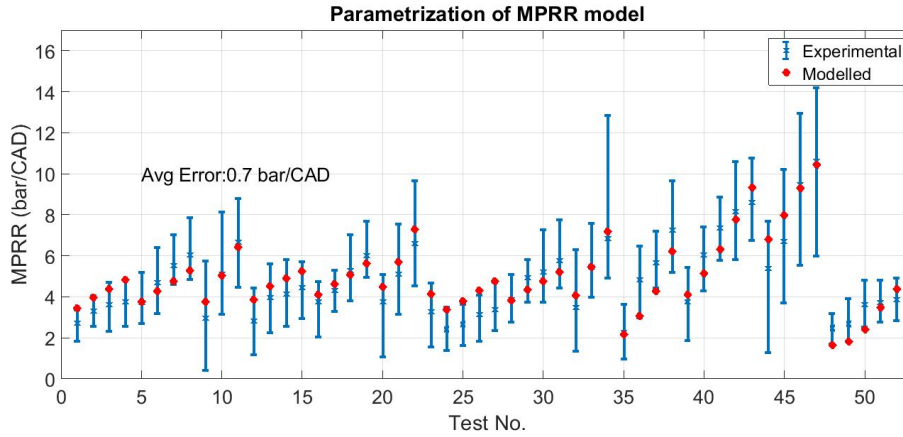


Figure 3.2: Data points used for parametrizing the model $N = 1000$ RPM, $T_{in} = 60^\circ \text{C}$

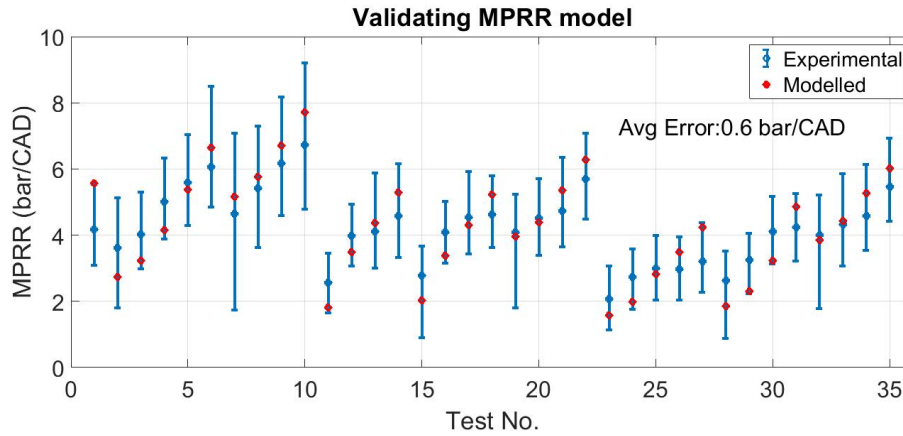


Figure 3.3: Experimental validation of the MPRR model at $N = 1000$ RPM, $T_{in} = 60^\circ \text{C}$

the 100 cycles is represented by the blue cross. The mean error between the predicted and the experimental values is 0.7 bar/CAD. The validation results are shown in Fig.

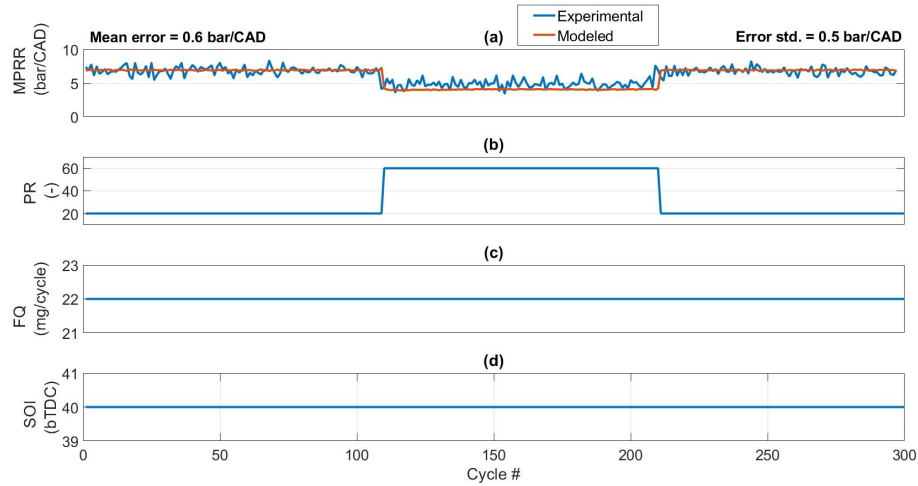


Figure 3.4: Transient validation of the MPRR model at $N = 1000$ RPM, $T_{in} = 60^\circ$ C, SOI = 40 CAD bTDC and FQ = 22 mg/cycle

3.3. These results confirm that the model is able to predict the MPRR with a mean error of 0.6 bar/CAD for steady-state conditions. The following sections will discuss the performance of the MPRR model for transient conditions.

3.3.4 PR Transient

The Fig. 3.4 shows the performance of the MPRR model when a step change in PR occurs. We can see that when the PR increases from 20 to 60 the MPRR reduces. The model is able to predict this change in the MPRR with an average error of 0.62 bar/CAD.

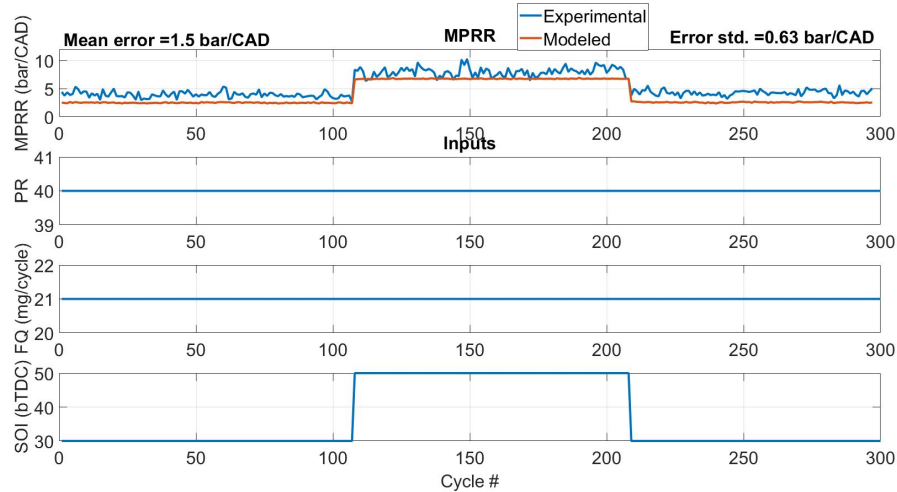


Figure 3.5: Transient validation of the MPRR model at $N = 1000$ RPM, $T_{in} = 60^\circ$ C, $PR = 40$ and $FQ = 21$ mg/cycle

3.3.5 SOI Transient

The Fig. 3.5 shows the performance of the MPRR model when a step change in SOI occurs. We can see that as the SOI is advanced from 30 CAD bTDC to 50 CAD bTDC, the MPRR increases. The model is able to predict this change in MPRR with an accuracy of 1.5 bar/CAD.

3.3.6 Statistical Analysis

In order to understand if the mean error of the model is acceptable, a statistical analysis was done on the experimental data. The aim of this analysis was to understand the range of MPRR within which most of the experimental data would fit. For this

purpose, the distribution of the MPRR of each data point's 100 cycles was plotted. The distribution plots of the data points with maximum, minimum and average variation across 100 cycles are shown in Fig. 3.6. The data was assumed to be a normal distribution. In a normal distribution, 2σ would cover 68% of the data [76]. Hence, σ was considered as the acceptable mean error.

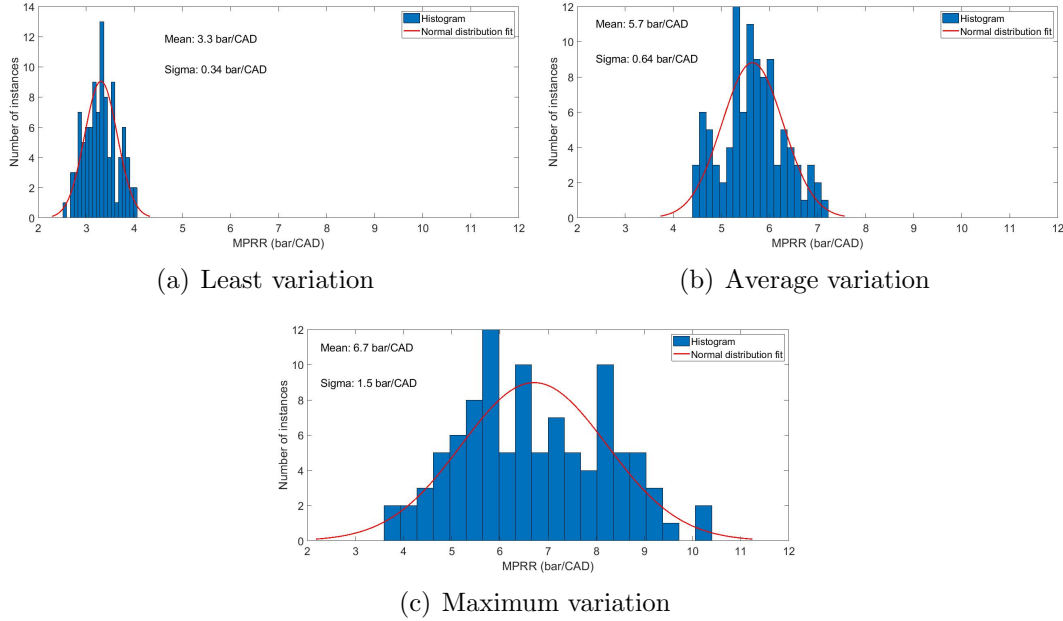


Figure 3.6: Statistical Analysis for three different operating conditions. (a) $N = 1000$, $T_{in} = 60^\circ$, $FQ = 19$ mg/cycle, $SOI = 40$ bTDC, $PR = 20$, (b) $N = 1000$, $T_{in} = 60^\circ$, $FQ = 19$ mg/cycle, $SOI = 35$ bTDC, $PR = 20$, (c) $N = 1000$, $T_{in} = 60^\circ$, $FQ = 22$ mg/cycle, $SOI = 45$ bTDC, $PR = 60$

As can be seen from the distribution plots in Fig. 3.6(a), σ for a data point with average variation is 0.6 bar/CAD. Thus, the MPRR model prediction error was within the MPRR cyclic variability limits of the RCCI engine studied. To this end, the MPRR model was able to predict the MPRR with similar or better accuracy for the

steady state and PR transient conditions. For SOI transient step the accuracy was still within 2σ of the data point with maximum variation and little over the 2σ of the data point with average variation. Given the MPRR model was able to largely predict with an accuracy of 0.7 bar/CAD or better, it was considered to be an accurate model for RCCI control applications.

3.4 CA50 model

Combustion phasing is one of the key parameters that characterize the combustion inside a cylinder. It is important to control the CA50 which is the Crank Angle at 50% Mass Fraction Burn (MFB) in order to achieve efficient combustion. For this purpose a Wiebe function is developed by Sadabadi [1]. The Wiebe function used is shown in Eq. (3.19):

$$X_b(\theta) = 1 - \exp\left(-A \left[\frac{\theta - \theta_{soc}}{\theta_d}\right]^B\right) \quad (3.19)$$

where, θ_{soc} is the SOC predicted by the MKIM discussed in Section 3.2 and θ_d is the burn duration that is estimated using the following equation:

$$\theta_d = C(1 + X_d)^D \cdot (\phi_{DI}^E + \phi_{PFI}^F) \quad (3.20)$$

where, X_d is the dilution fraction that includes the affect of EGR and residual gases. ϕ_{DI} and ϕ_{PFI} are the equivalence ratios as presented in Eq. (3.2) and (3.3). The constants A, B, C, D, E and F need to be parametrized. The optimized parameters are presented in Table 3.4.

A	B	C	D	E	F
0.1073	14.952	6.5361	0.03813	-0.1726	0.1064

Table 3.4
Optimized parameters for CA50 model

3.5 IMEP Model

IMEP is one of the major parameters of interest in engine control. It is linked to the engine load which should be controlled in engine applications. In order to control the IMEP a model needs to be developed that is able to predict the IMEP of the engine. IMEP is calculated using Eq. (3.21). It is the cyclic integral of in-cylinder pressure times the volume.

$$IMEP = \frac{1}{V_{dis}} \oint P dV \quad (3.21)$$

However, since the accurate prediction of P at every crank angle during combustion is computationally intensive, Bidarvatan [77] suggested the use of temperature variations to calculate the IMEP as shown in Eq. (3.22)

$$IMEP_{K+1} = m_{t,K+1} \frac{c_v}{V_{dis}} (T_{ivc,K+1} - T_{soc,K+1} + T_{eoc,K+1} - T_{evc,K+1}) \quad (3.22)$$

This work uses the same method as shown above to predict the IMEP which was validated in prior work on the same engine setup [4].

3.6 Cycle by Cycle dynamic model

In order to be able to control the RCCI engine effectively during transients, it is important to model the transient behaviour within the combustion chamber. Each combustion cycle has an effect on the next combustion cycle. This phenomenon has to be taken into account along with the effects of the mixing of residual gases trapped at the end of each cycle, with the fresh charge of it's successive cycle. For this purpose a cycle by cycle dynamic model is developed to represent the behaviour from IVO to EVC.

3.6.1 Intake stroke ($IVO \rightarrow IVC$)

During this phase, the dynamic model is initialized with the initial conditions for $PR, T_{in}, SOI, \phi_{tot}$ and P_{exh} . These initial values are set parameters either manually or by the controller. As discussed in the previous Section 3.2, the P_{ivc} and T_{ivc} are assumed to be equal to that of the manifold P and T as the IVC is 2 CAD bBDC. However, the residual gases that were trapped from the previous cycle will have an effect on the temperature of the intake charge. This in turn affects the SOC and CA50. The mixture temperature at IVC is calculated using the Eq. (3.23):

$$T_{ivc,k+1} = (1 - X_{rg})T_{in,k+1} + X_{rg}T_{rg,k} \quad (3.23)$$

where, $T_{ivc,k+1}$ is the temperature of the charge at IVC in current cycle, X_{rg} is the residual gas mass fraction and $T_{rg,k}$ is the temperature of the residual gas in the previous cycle. However, for the first cycle the parameter T_{rg} needs to be initialized. For this, the model developed by Cavina [78] is used in this work. It is represented in Eq. (3.24)

$$X_{rg} = \sqrt{\frac{1}{C}} \cdot \frac{\pi \cdot \sqrt{2}}{360} \cdot \frac{r_c - 1}{r_c} \cdot \frac{OF}{N} \sqrt{\frac{R \cdot T_{in} |P_{exh} - P_{in}|}{P_{exh}}} \cdot \left(\frac{P_{exh}}{P_{in}}\right)^{\frac{\gamma+1}{2\gamma}} + \frac{1}{C} \cdot \frac{r_c - 1}{r_c} \phi_{tot} \frac{V_{ivo}}{V_{dis}} \cdot \left(\frac{P_{exh}}{P_{in}}\right)^{\frac{1}{\gamma}} \quad (3.24)$$

where, T_{in} and P_{in} are the intake temperature and pressure respectively, r_c is the compression ratio, OF is the overlap of intake and exhaust valves, P_{exh} is the exhaust pressure, R is the gas constant, γ is the ratio of specific heats and V_{ivo} and V_{dis} are the volume at IVO and displaced volume respectively. C is calculated using the following equation:

$$C = \left[1 + \frac{LHV}{c_v T_{in} \left(\frac{m_{tot}}{m_f}\right) \cdot r_c^{\gamma-1}} \right]^{\frac{1}{\gamma}} \quad (3.25)$$

where, LHV is the lower heating value of the mixture calculated using the Eq. (3.26) and c_v is the specific heat capacity at constant volume calculated at IVC conditions.

$$LHV = \frac{PR}{100} \cdot LHV_{iso} + \left(1 - \frac{PR}{100}\right) \cdot LHV_{nhep} \quad (3.26)$$

Once the X_{rg} is calculated using the Eq. (3.24) for the first cycle, during the consecutive cycle the X_{rg} is calculated using the Eq. (3.27). This is done in an iterative loop

until X_{rg} converges to a terminal value. T_{rg} is also recalculated by using the same method until it converges to a terminal value.

$$X_{rg} = \frac{m_{rg}}{m_{tot}} \quad (3.27)$$

Where m_{tot} is the total mass of the charge at IVC and m_{rg} is the mass of the residual gas which is calculated using the Eq. (3.44) explained in Section 3.6.5.

3.6.2 Polytropic Compression $IVC \rightarrow SOC$

The P_{soc} and T_{soc} are calculated using the Eq. (3.28) and (3.29) assuming the compression is polytropic [79].

$$T_{soc,k+1} = T_{ivc,k+1} \left(\frac{V_{ivc}}{V_{soc,k+1}} \right)^{n_c-1} \quad (3.28)$$

$$P_{soc,k+1} = P_{ivc,k+1} \left(\frac{V_{ivc}}{V_{soc,k+1}} \right)^{n_c} \quad (3.29)$$

However, to use Eq. (3.28) and (3.29), the SOC has to be calculated using the MKIM developed in Section 3.2. n_c is the polytropic coefficient calculated from experimental data and V_{ivc} and V_{soc} are the volumes at IVC and SOC, respectively.

3.6.3 Combustion ($SOC \rightarrow EOC$)

MPPRR and CA50 are predicted during the combustion phase with the models presented in the previous sections 3.3.3 and 3.4. EOC and BD are estimated using the following models.

3.6.3.1 BD Model for EOC estimation

The primary mechanism of combustion in RCCI is the spontaneous ignition front as the flame propagation cannot be sustained [66]. A correlation was developed by Sadabadi between the Burn Duration (BD) and the spontaneous ignition front speed (S_{ig}) [1] as shown in Eq. (3.30):

$$BD = K_2(S_{ig})^t \quad (3.30)$$

where, K_2 and t are parameters that need to be estimated. Since, the high reactivity fuel and the low reactivity fuel create stratified layers and pockets of rich and high reactive fuel, the ignition delay is not constant throughout the combustion chamber. Hence, Sadabadi proposed the use of Eq. (3.31) to calculate the ignition front speed.

$$S_{ig} = \frac{1}{\left| \frac{d\tau}{d\phi_{DI}} \right| |\nabla \phi_{DI}|} \quad (3.31)$$

where, τ , the ignition delay is calculated using the denominator of the MKIM equation presented in Eq. (3.1) from SOI to SOC. The equivalence ratio gradient is calculated using the following Eq. (3.32):

$$|\nabla \phi_{DI}| = \frac{K_1}{ID^p} \cdot \phi_{DI}^r \quad (3.32)$$

$$ID = SOI - SOC \quad (3.33)$$

where, ID is the Ignition Delay and p, r and k_1 are parameters that are estimated. EOC is then estimated using the BD that was just calculated.

$$EOC = SOC + BD \quad (3.34)$$

The rise in temperature during combustion is given by Eq. (3.35):

$$\Delta T = \frac{LHV_{DI} FAR_{st,nhep} \cdot \phi_{DI} + LHV_{PFI} FAR_{st,iso} \cdot \phi_{PFI}}{c_v (FAR_{st,nhep} \cdot \phi_{DI} + FAR_{st,iso} \cdot \phi_{PFI} + 1)} \quad (3.35)$$

K_1	t	K_2	a_0	a_1	a_2
4.254	-0.3347	32.6389	0.2152	-1.2389e-05	4.1071e-07
b_0	b_1	b_2	p	r	
12.42655	0.001407	-3.3397e-05	2.2201e-05	0.53812	

Table 3.5
Optimized parameters for the BD model

The temperature at EOC ($T_{eoc,k+1}$) and pressure at EOC (P_{eoc}) are calculated using the Eq. (3.36) and 3.37

$$T_{eoc,k+1} = T_{soc,k+1} + e_1 \cdot \Delta T \quad (3.36)$$

$$P_{eoc,k+1} = P_{soc,k+1} + e_2 \cdot \Delta T \quad (3.37)$$

where, e_1 and e_2 are parameters that account for the heat loss and can be assumed to be a polynomial of 2nd degree [80] which are calculated using Eq. (3.38) and (3.39)

$$e_1 = a_0 + a_1 \theta_{soc} + a_2 \theta_{soc}^2 \quad (3.38)$$

$$e_2 = b_0 + b_1 \theta_{soc} + b_2 \theta_{soc}^2 \quad (3.39)$$

where, a_0, a_1, a_2, b_0, b_1 and b_2 are constants that are required to be estimated. The optimized parameters are shown in Table 3.5

3.6.4 Polytropic Expansion ($EOC \rightarrow EVO$)

The expansion phase from EOC to EVO can be approximated as a polytropic process [79]. The pressure at EVO (P_{evo}) and temperature at EVO (T_{evo}) can be calculated using the following equations:

$$T_{evo,k+1} = T_{eoc,k+1} \left(\frac{V_{eoc,k+1}}{V_{evo}} \right)^{n_e-1} \quad (3.40)$$

$$P_{evo,k+1} = P_{eoc,k+1} \left(\frac{V_{eoc,k+1}}{V_{evo}} \right)^{n_e} \quad (3.41)$$

where, n_e is the polytropic coefficient of expansion that is estimated from the experimental data.

3.6.5 Exhaust stroke ($EVO \rightarrow EVC$)

The last phase, exhaust stroke, is approximated to a polytropic process [79]. The temperature at EVC ($T_{evc,k+1}$) can be estimated using the following equation:

$$T_{evc,k+1} = T_{evo,k+1} \left(\frac{P_{exh,k+1}}{P_{evo,k+1}} \right)^{\frac{n_e-1}{n_e}} \quad (3.42)$$

where, exhaust pressure at current cycle is represented by $P_{exh,k+1}$. The temperature at EVC ($T_{evc,k+1}$) is assumed to be equal to that of the residual gas ($T_{rg,k+1}$). Hence, the mass of residual gas ($m_{rg,k+1}$) is estimated using the Eq. (3.43):

$$m_{rg,k+1} = \frac{P_{exh,k+1} \cdot V_{evc}}{R_{evc} \cdot T_{rg,k+1}} \quad (3.43)$$

where, R_{evc} is the gas constant. Therefore, the residual gas fraction can be calculated using the Eq. (3.44):

$$X_{rg,k+1} = \frac{m_{rg,k+1}}{m_{tot,k+1}} \quad (3.44)$$

A schematic of the entire RCCI cycle by cycle dynamic model is shown in Fig. 3.7. This model is capable of running at 36 ms/cycle on an Intel[®] Xeon[®] processor with 16 GB of RAM

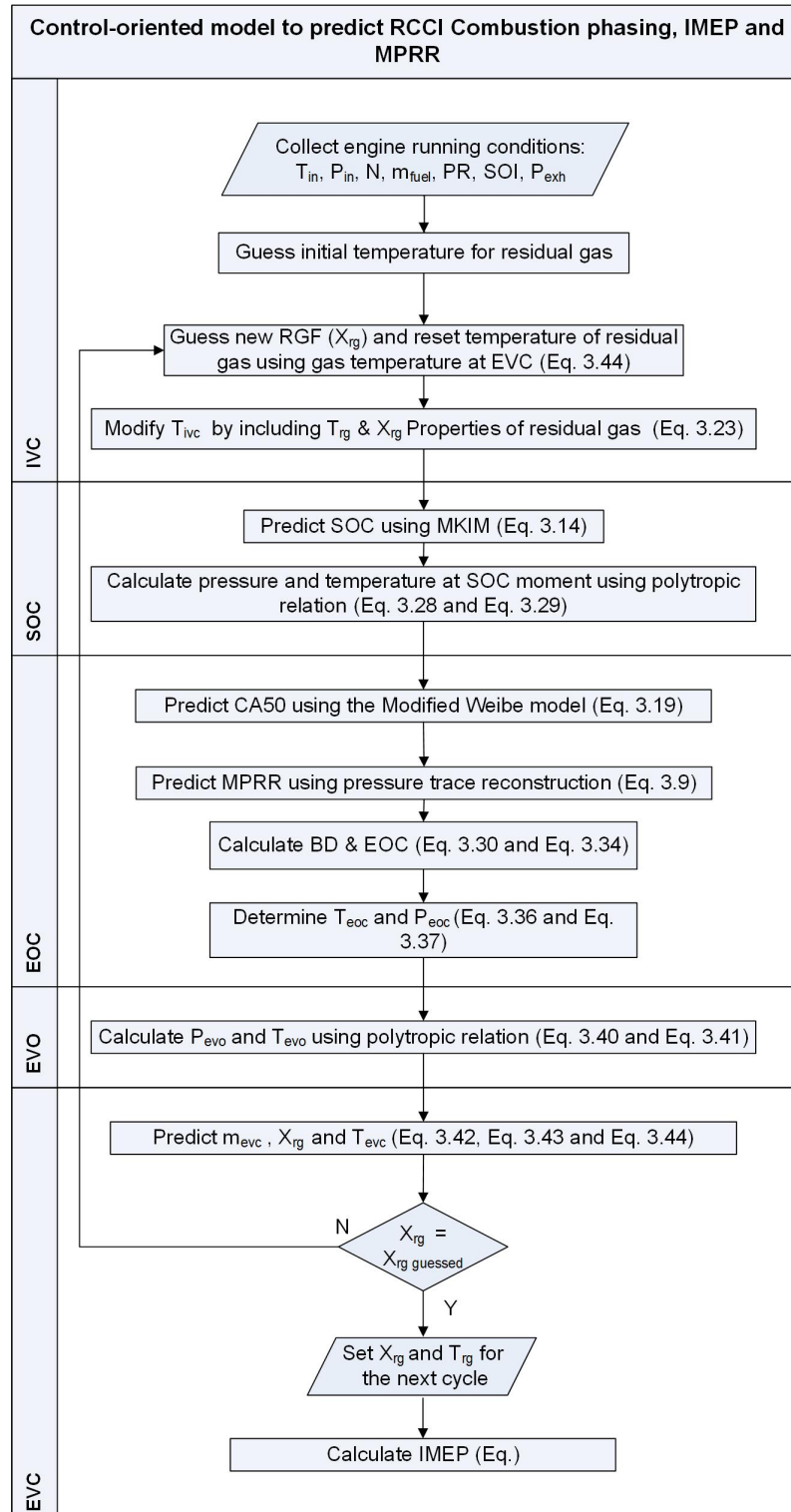


Figure 3.7: Cycle by cycle RCCI dynamic model schematic

3.7 Data Driven LPV identification

3.7.1 Introduction

There have been few works in the past that have developed COM for RCCI engines [1, 4, 51]. However, all of these models are based on first principle physics equations. They either use CFD or physics based equations to represent the dynamics of the combustion inside the chamber. These models have been fairly successful. However, it takes considerable amount of time, effort and money to develop and validate these models. However, another approach can be employed to develop these COMs with relative ease and investment and that is the Data Driven Modeling (DDM) approach. The advantage of this approach is that it does not require a thorough knowledge of the plant physics and the interactions and the relationships of various parameters in the plant. This work uses a method in DDM put forward by Rizvi et al. [6] and has been used for RCCI engines by Khoshbakhat et al. [5]. It uses a Machine Learning (ML) strategy called Support Vector Machine (SVM) which is used to classify between to classes of data. This strategy is capable of solving prediction problems [81] and in this work is extended to identify RCCI combustion metrics.

For linear control purposes, one approach of controller design is via state space representation, which is followed in this thesis. To this end, the RCCI model needs to be presented in state space form. For this purpose, the model is linearized around an operating point. But, the state space representation is not accurate over a large range of operating points. In order to operate over a large range of operating points, multiple state space representations are developed. The controller then switches between these state space representations based on the operating conditions. This leads to extensive time and efforts spent in developing these controllers and tuning them. In order to avoid this, a Linear Parameter Varying (LPV) representation can be used. In an LPV representation the A, B, C and D matrices of the state space representation are described as a function of a parameter called scheduling parameter p . A scheduling parameter is a time varying parameter that allows for capturing the dynamic behavior of the plant. As the scheduling parameter changes, the plant representation changes adapting to the change in plant's behaviour. In this work a DDM approach is used to identify an LPV representation for RCCI combustion metrics.

3.7.2 DDM for LPV identification

This Section describes the SVM based DDM used to develop the state-space LPV representation for the RCCI engine model. The following equations Eq. (3.45) and (3.46) show how the LPV system is defined.

$$x_{k+1} = A(p_k)x_k + B(p_k)u_k + K(p_k)e_k \quad (3.45)$$

$$y_k = C(p_k)x_k + e_k \quad (3.46)$$

where x , y and u are the states of the plant, measurable outputs of the plant and the inputs to the plant respectively. p represents the scheduling parameter, e represents stochastic white noise. Each of these parameters are defined in discrete time represented by k . The matrices, $A(p_k)$, $B(p_k)$, $C(p_k)$ and $K(p_k)$ are the state space matrices of the plant as a function of the scheduling parameter p . The equations Eq. (3.45) and Eq. (3.46) can be rewritten as shown in Eq. (3.47) and (3.48):

$$x_{k+1} = \underbrace{(A(p_k) - K(p_k)C(p_k))}_{\tilde{A}(p_k)} x_k + B(p_k)u_k + K(p_k)y_k \quad (3.47)$$

$$y_k = C(p_k)x_k + e_k \quad (3.48)$$

For LPV identification, the $\tilde{A}(p_k)$, $B(p_k)$ and $C(p_k)$ have to be computed using the measured training data. In this work, SVM strategy is used to compute these matrices based on measured training data $[x_k, u_k, p_k, y_k]_{k=1}^N$. The matrices, $\tilde{A}(p_k)$, $B(p_k)$, $C(p_k)$ and $K(p_k)$ can be represented using Eq. (3.49) to (3.52) based on the SVM strategy.

$$\tilde{A}(p_k) = W_1\Phi_1(p_k) \quad (3.49)$$

$$B(p_k) = W_2\Phi_2(p_k) \quad (3.50)$$

$$K(p_k) = W_3\Phi_3(p_k) \quad (3.51)$$

$$C(p_k) = W_4\Phi_4(p_k) \quad (3.52)$$

where W_1, W_2, W_3 and W_4 are support vector weighting matrices and Φ_1, Φ_2, Φ_3 and Φ_4 are feature maps. All of these parameters are unknown and need to be computed.

Now, Eq. (3.47) and 3.48 can be rewritten as shown in Eq. (3.53) and (3.54):

$$x_{k+1} = W_1\Phi_1(p_k)x_k + W_2\Phi_2(p_k)u_k + W_3\Phi_3(p_k)y_k \quad (3.53)$$

$$y_k = W_4\Phi_4(p_k)x_k \quad (3.54)$$

In order to optimize the computation of the state-space matrices, a cost function has to be defined. The cost function should be dependant on the magnitude of the weighing matrices W_1, W_2, W_3 and W_4 and also should account for the error in estimation for the training data. For this purpose, a Least Squares optimization method has been chosen. The method used here was proposed by Suykens et. al [82] and is used to compute the support vector weighing matrices. The cost function is

shown in Eq. (3.55):

$$J = \frac{1}{2} \sum_{i=1}^3 \|W_i\|_F^2 + \frac{1}{2} \sum_{k=1}^N E_k^T \Gamma E_k \quad (3.55)$$

where, Γ is a diagonal matrix of the weighing factors for the error in estimation known as the regularization matrix and $\|\cdot\|_F$ is the Frobenius norm. The method of Lagrange multipliers can be used for minimizing the cost function shown in Eq. (3.55). The Lagrangian function can be represented using the equation shown in Eq. (3.56):

$$\begin{aligned} \mathcal{L}(W_1, W_2, W_3, W_4, \alpha, \beta, e) = J - \sum_{j=1}^N \alpha_j^T \{W_1 \Phi_1(p_j) x_j + W_2 \Phi_2(p_j) u_j + \\ W_3 \Phi_3(p_j) y_j - x_{j+1}\} - \sum_{j=1}^N \beta_j^T \{W_4 \Phi_4(p_j) x_j - y_{j+1}\} \end{aligned} \quad (3.56)$$

where, j is discrete time and α_j and β_j are the Lagrangian multipliers. The global optimum of the Lagrangian can be found when the derivative is equal to zero, as it has a convex shape. The derivatives are shown in Eq. (3.57) to (3.63):

$$\frac{\partial \mathcal{L}}{\partial \alpha_i} = 0 \Rightarrow x_{j+1} = W_1 \Phi_1(p_j) x_j + W_2 \Phi_2(p_j) u_j + W_3 \Phi_3(p_j) y_j \quad (3.57)$$

$$\frac{\partial \mathcal{L}}{\partial W_1} = 0 \Rightarrow W_1 = \sum_{j=1}^N \alpha_j x_j^T \Phi_1^T(p_j) \quad (3.58)$$

$$\frac{\partial \mathcal{L}}{\partial W_2} = 0 \Rightarrow W_2 = \sum_{j=1}^N \alpha_j u_j^T \Phi_2^T(p_j) \quad (3.59)$$

$$\frac{\partial \mathcal{L}}{\partial W_3} = 0 \Rightarrow W_3 = \sum_{j=1}^N \alpha_j y_j^T \Phi_3^T(p_j) \quad (3.60)$$

$$\frac{\partial \mathcal{L}}{\partial W_4} = 0 \Rightarrow W_4 = \sum_{j=1}^N \beta_j x_j^T \Phi_4^T(p_j) \quad (3.61)$$

$$\frac{\partial \mathcal{L}}{\partial e_j} = 0 \Rightarrow \beta_j = \Gamma e_j \quad (3.62)$$

$$\frac{\partial \mathcal{L}}{\partial \beta_j} = 0 \Rightarrow y_j = W_4 \Phi_4(p_j) x_j \quad (3.63)$$

Now, Eq. (3.53) and (3.54) can be rewritten as shown in Eq. (3.64) and (3.65):

$$x_{k+1} = \underbrace{\sum_{j=1}^N \alpha_j x_j^T \Phi_1^T(p_j)}_{W_1} \Phi_1(p_k) x_k + \underbrace{\sum_{j=1}^N \alpha_j u_j^T \Phi_2^T(p_j)}_{W_2} \Phi_2(p_k) u_k + \underbrace{\sum_{j=1}^N \alpha_j y_j^T \Phi_3^T(p_j)}_{W_3} \Phi_3(p_k) y_k \quad (3.64)$$

$$y_k = \underbrace{\sum_{j=1}^N \beta_j x_j^T \Phi_4^T(p_j)}_{W_4} \Phi_4(p_k) x_k + \underbrace{\Gamma^{-1} \beta_k}_{e_k} \quad (3.65)$$

The inner product of $\Phi_4^T(p_j)W_4\Phi_4(p_k)$ can be replaced with a kernel matrix as shown in Eq. (3.66) and (3.67):

$$[\Omega]_{j,k} = \sum_{i=1}^3 z_i^T(j)\bar{k}^i(p_j, p_k)z_i(k) \quad (3.66)$$

$$[\Xi]_{j,k} = x_j^T \bar{k}^4(p_j, p_k)x_k \quad (3.67)$$

where, $z_1(k) = x_k$, $z_2(k) = u_k$ and $z_3(k) = y_k$. In this work, a Gaussian kernel was used which is defined as shown in Eq. (3.68):

$$\bar{k}^i(p_j, p_k) = \exp\left(-\frac{\|p_j - p_k\|_2^2}{2\sigma_i^2}\right) \quad (3.68)$$

where, σ_i is the standard deviation for the gaussian function and $\|\cdot\|$ is the l_2 norm.

Using the Eq. (3.66) and (3.67), Eq. (3.64) and (3.65) can be rewritten as Eq. (3.69)

and (3.70):

$$X_{k+1} = \alpha\Omega \quad (3.69)$$

$$Y = \beta\Xi + \Gamma^{-1}\beta \quad (3.70)$$

where, X_{k+1} and Y are the states and the outputs used in the training data. Thus, α and β can be solved using the following equations:

$$\alpha = X_{k+1}\Omega^{-1} \quad (3.71)$$

$$vec(\beta) = (I_N \otimes \Gamma^{-1} + \Xi^T \otimes I_{n_y})^{-1}vec(Y) \quad (3.72)$$

where, \otimes represents the Kronecker product and $vec(\cdot)$ represents vectorization function. I_{n_y} and I_N are identity matrices. The classical sylvester equation can be used to solve Eq. (3.72). Once α and β have been computed, $\tilde{A}(\cdot)$, $B(\cdot)$, $K(\cdot)$ and $C(\cdot)$ can be computed using the following Eq. (3.73) to (3.76):

$$\tilde{A}(\cdot) = W_1\Phi_1(\cdot) = \sum_{k=1}^N \alpha_k x_k^T \bar{k}^1(p_k, \cdot) \quad (3.73)$$

$$B(\cdot) = W_2\Phi_2(\cdot) = \sum_{k=1}^N \alpha_k u_k^T \bar{k}^2(p_k, \cdot) \quad (3.74)$$

$$K(\cdot) = W_3\Phi_3(\cdot) = \sum_{k=1}^N \alpha_k y_k^T \bar{k}^3(p_k, \cdot) \quad (3.75)$$

$$C(\cdot) = W_4\Phi_4(\cdot) = \sum_{k=1}^N \beta_k x_k^T \bar{k}^3(p_k, \cdot) \quad (3.76)$$

3.7.3 LPV model identification and validation

The methodology explained in the previous Section 3.7.2 can be used to develop a state-space representation for RCCI combustion metrics using experimental data. This largely reduces the amount of time and effort needed to develop a state space representation. The experimental data that is used for the LPV identification has to be collected over the operating range of interest and should capture the dynamic behaviour of the engine. This allows for the development of a robust LPV model. However, due to lack of experimental data that captured the dynamics of MPRR, the data generated by the dynamic model explained in Section 3.6 along with the models for MPRR, SOC, CA50 and IMEP presented in Sections 3.2, 3.3, 3.4 and 3.5 is used. The RCCI engine model is excited with a combination of inputs (FQ, SOI and PR) and the output response (CA50, P_{soc} , T_{soc} , IMEP and MPRR) of the model is recorded. The recorded output of the RCCI engine model is then used to identify the LPV representation.

The state-space representation for RCCI combustion is shown below in Eq. (3.77) to (3.80):

$$X = \left[CA50 \quad MPRR \quad T_{soc} \quad P_{soc} \quad IMEP \right]^T \quad (3.77)$$

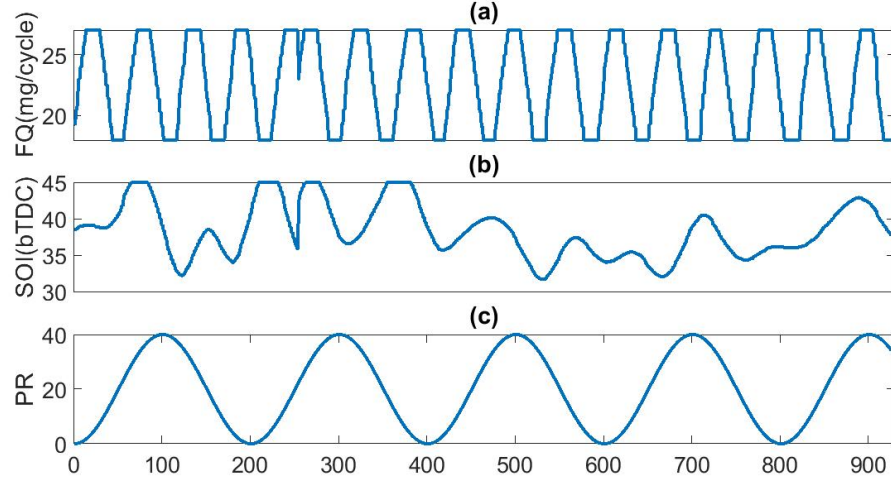


Figure 3.8: Inputs to RCCI dynamic Model $N = 1000$ RPM, $T_{in} = 60^\circ$ C

$$U = \begin{bmatrix} SOI & FQ \end{bmatrix}^T \quad (3.78)$$

$$p = \begin{bmatrix} PR \end{bmatrix} \quad (3.79)$$

$$Y = \begin{bmatrix} CA50 & MPRR & IMEP \end{bmatrix}^T \quad (3.80)$$

The RCCI engine model is excited with inputs (FQ, SOI and PR) as shown in Fig. 3.8. The output response of the RCCI engine model is recorded as shown in Fig. 3.9. The combination of the input and output data generated from the RCCI engine model is used to train the data driven SVM based LPV identification algorithm.

A total of 926 operating points have been collected from the RCCI engine model. This data set is now divided into a training and testing data sets. 65% of the data is used for training the SVM based LPV identification algorithm while the rest 35%

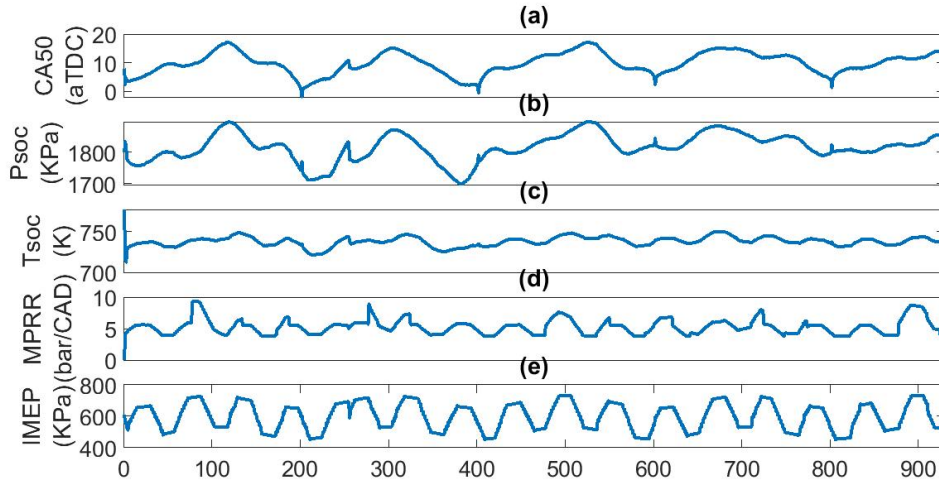


Figure 3.9: State outputs from the RCCI dynamic model $N = 1000$ RPM, $T_{in} = 60^\circ$ C

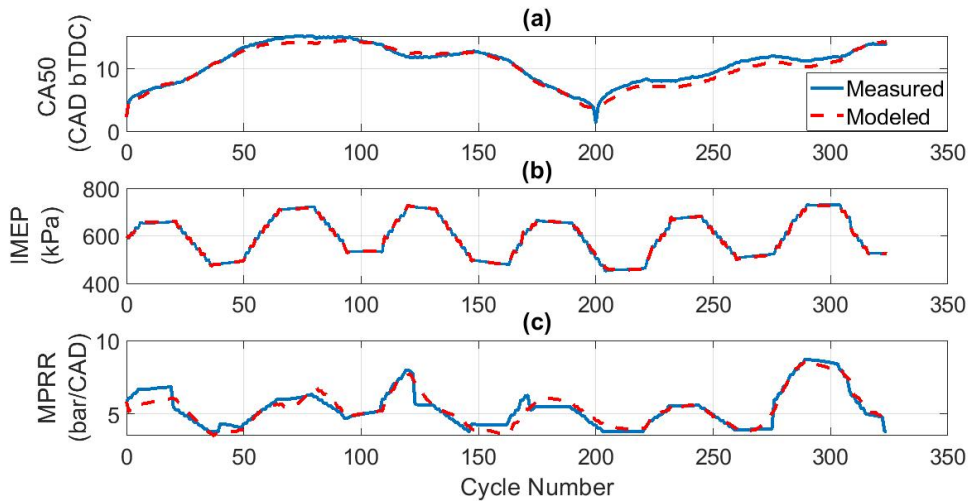


Figure 3.10: Data driven SVM based LPV identification on validation data set at $N = 1000$ RPM, $T_{in} = 60^\circ$ C

is used for testing the identified state-space model. The results of the validation of identified LPV state-space representation are shown in Fig. 3.10.

As shown in Fig. 3.10, the mean error of the LPV state-space representation is 0.5 bar/CAD which is considered acceptable based on the statistical analysis performed

in Section 3.3.3.

An example of A, B, C and D matrices for PR = 20 are shown in the following equations:

$$A = \begin{bmatrix} 0.0203 & 0.0157 & -0.0123 & 0.0152 & -0.0069 \\ -0.4793 & 0.3118 & 1.6990 & 0.0607 & -0.2189 \\ -0.1894 & 0.0452 & 0.7742 & 0.0139 & -0.0162 \\ 0.0204 & 0.0168 & -0.0512 & 0.0832 & -0.0009 \\ 0.0221 & 0.0552 & -0.0789 & 0.0276 & -0.1690 \end{bmatrix} \quad (3.81)$$

$$B = \begin{bmatrix} 0.0386 & -0.3369 & 0.3222 \\ 2.1636 & -4.8719 & 13.3732 \\ 0.5935 & 0.0278 & 4.0693 \\ 0.2575 & 0.1000 & 0.1192 \\ 25.5645 & 0.2879 & 3.2134 \end{bmatrix} \quad (3.82)$$

$$C = \begin{bmatrix} 1 & 0 & 0 & 0 & 0 \\ 0 & 1 & 0 & 0 & 0 \\ 0 & 0 & 0 & 0 & 1 \end{bmatrix} \quad (3.83)$$

$$D = \begin{bmatrix} 0 \end{bmatrix} \quad (3.84)$$

Chapter 4

Combustion Phasing and Load Control with MPRR Limitation

This chapter discusses the development and testing of the Multiple Input Multiple Output (MIMO) LPV - MPC for controlling the combustion phasing (CA50) and engine load (IMEP) while limiting the MPRR of the RCCI engine.

4.1 Development of the LPV system

As shown in Section 3.7.3 a state-space representation was developed to fully define the RCCI engine model presented in Section 3.6. The same state-space representation

is used for the MIMO MPC developed in this section. Thus the states of the LPV state-space are:

1. Crank Angle for 50% mass fraction burned ($CA50$)
2. Maximum Pressure Rise Rate within the combustion cycle ($MPRR$)
3. Temperature at Start of Combustion (T_{soc})
4. Pressure at Start of Combustion (P_{soc})
5. Indicated Mean Effective Pressure ($IMEP$)

The states can then be expressed using the following Eq. (4.1) and Eq. (4.2) where k represents discrete time.

$$X_{k+1} = A(p_k).X_k + B(p_k).U_k \quad (4.1)$$

$$Y_k = C(p_k).X_k + D.U_k \quad (4.2)$$

where,

$$X = \begin{bmatrix} CA50 & MPRR & T_{soc} & P_{soc} & IMEP \end{bmatrix}^T \quad (4.3)$$

$$U = \begin{bmatrix} SOI & FQ \end{bmatrix}^T \quad (4.4)$$

$$p_k = \begin{bmatrix} PR \end{bmatrix} \quad (4.5)$$

$$Y = \begin{bmatrix} CA50 & MPRR & IMEP \end{bmatrix}^T \quad (4.6)$$

Using the Data Driven SVM based LPV identification model presented in Section 3.7.2, an LPV system is developed for the dynamic RCCI engine model. The state space matrices $A(p_k)$ and $B(p_k)$ are plotted against the scheduling parameter, PR in Fig. 4.1 and Fig. 4.2

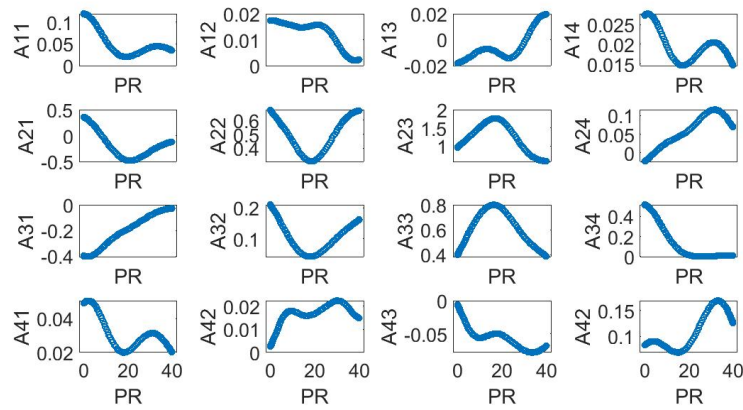


Figure 4.1: $A(p_k)$ vs scheduling parameter (PR)

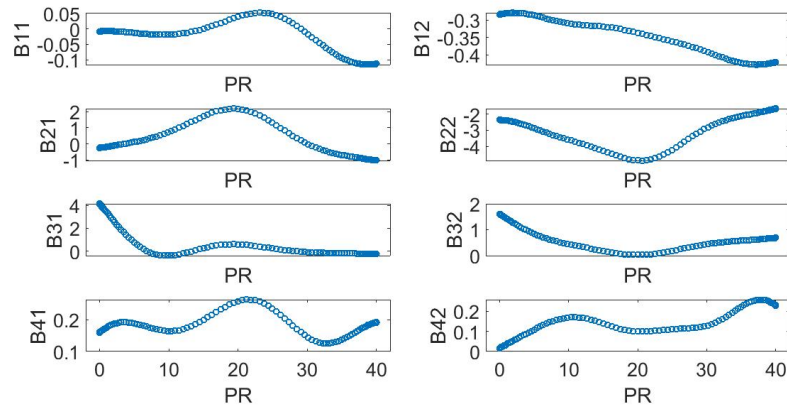


Figure 4.2: $A(p_k)$ vs scheduling parameter (PR)

An example $A(p_k)$, $B(p_k)$, $C(p_k)$ and $D(p_k)$ for $p_k = 40$ is shown in Eq. (4.7) to (4.10).

These matrices represent the relationship between the states with themselves and the inputs. They are updated at the beginning of every cycle based on the scheduling parameter, PR.

$$A = \begin{bmatrix} 0.0347 & 0.0024 & 0.0195 & 0.0146 & -0.0026 \\ -0.1198 & 0.6699 & 0.5719 & 0.0685 & 0.0031 \\ -0.0271 & 0.1624 & 0.3839 & 0.0088 & 0.0455 \\ 0.0202 & 0.0150 & -0.0676 & 0.1260 & 0.0060 \\ 0.0356 & 0.2247 & -0.4759 & 0.0428 & -0.1097 \end{bmatrix} \quad (4.7)$$

$$B = \begin{bmatrix} -0.1129 & -0.4212 & 0.3710 \\ -1.0282 & -1.6608 & 6.9155 \\ -0.2619 & 0.6870 & 2.6769 \\ 0.1914 & 0.2281 & 0.2595 \\ 24.8187 & 1.2000 & 0.8086 \end{bmatrix} \quad (4.8)$$

$$C = \begin{bmatrix} 1 & 0 & 0 & 0 & 0 \\ 0 & 1 & 0 & 0 & 0 \\ 0 & 0 & 0 & 0 & 1 \end{bmatrix} \quad (4.9)$$

$$D = \begin{bmatrix} 0 & 0 \\ 0 & 0 \\ 0 & 0 \end{bmatrix} \quad (4.10)$$

4.2 Model Predictive Controller (MPC)

4.2.1 Controller design

The MPC was developed using the MATLAB[®] Model Predictive Control[™] toolbox. The MPC is designed using a linear state space representation, similar to shown in Eq. 4.11 and Eq. 4.12, that is used to calculate the current states and predict the future plant outputs.

$$X(k+1) = A.X(k) + B.U(k) \quad (4.11)$$

$$Y(k) = C.X(k) + D.U(k) \quad (4.12)$$

where, k denotes the control step, X is a vector of states, Y is a vector of outputs, A is a $n \times n$ matrix, B is a $n \times m$ matrix, C is a $q \times n$ matrix and D is a $q \times m$ matrix where n is the number of states, m is the number of inputs and q is the number of output states.

The controller solves a Quadratic Problem (QP) at each time step to optimize the manipulated variable adjustments. It solves the QP subject to the constraints defined on the inputs and the outputs. The optimization problem is only solved over a certain number of future control time steps, called the prediction horizon. During each optimization, only a fixed number of control steps, called control horizon, are optimized. Invariably, the size of the control and prediction horizons affect the run time performance of the controller. The cost function used for the QP is shown in the following equation:

$$J(z_k) = J_y(z_k) + J_{\Delta u}(z_k) + J_\epsilon(z_k) \quad (4.13)$$

where k is the control interval, z_k is the QP decision as shown in Eq. 4.17 and $J_y(z_k)$ is the cost function for reference tracking, $J_{\Delta u}(z_k)$ is the cost function for manipulated variable rate of change and $J_\epsilon(z_k)$ is the cost function for constraint violation. Each of the cost functions are shown in the following equations:

$$J_y(z_k) = \sum_{j=1}^{n_y} \sum_{i=1}^p \left\{ \frac{W_{i,j}^y}{S_j^y} [r_j(k+i|k) - y_j(k+i|k)] \right\}^2 \quad (4.14)$$

$$J_{\Delta u}(z_k) = \sum_{j=1}^{n_u} \sum_{i=0}^{p-1} \left\{ \frac{W_{i,j}^{\Delta u}}{S_j^u} [u_j(k+i|k) - u_j(k+i-1|k)] \right\}^2 \quad (4.15)$$

$$J_\epsilon(z_k) = \rho_\epsilon \epsilon_k^2 \quad (4.16)$$

where p is the prediction horizon, n_y is the number of output states, n_u is the number

of manipulated variables, $y_j(k+i|k)$ is the predicted value of the j^{th} plant output at the i_{th} prediction horizon step, $r_j(k+i|K)$ is the reference value for j^{th} plant output at the i_{th} prediction horizon step, S_j^y is the scale factor for j^{th} plant output, $W_{i,j}^y$ is the tuning weight of the j^{th} plant output at the i_{th} prediction horizon step, S_j^u is the scale factor for j^{th} manipulated variable, $W_{i,j}^u$ is the tuning weight for j^{th} manipulated variable at the i_{th} prediction horizon step and ρ_ϵ is the constraint violation penalty weight.

$$z_k^T = [u(k|k)^T \quad u(k+1|k)^T \quad \dots u(k+p-1|k)^T \quad \epsilon_k] \quad (4.17)$$

Where ϵ_k is the slack variable at control interval k .

The MPC evaluates constraints at every control step. The following constraints are applied on the MPC:

$$\frac{Y_{j,min}(i)}{S_j^y} - \epsilon_k V_{j,min}^y(i) \leq \frac{Y_j(k+i|k)}{S_j^y} \leq \frac{y_{j,max}(i)}{S_j^y} + \epsilon_k V_{j,max}^y(i), \quad (4.18)$$

$$i = 1 : p, j = 1 : n_y$$

$$\frac{u_{j,min}(i)}{S_j^u} - \epsilon_k V_{j,min}^u(i) \leq \frac{u_j(k+i-1|k)}{S_j^u} \leq \frac{u_{j,max}(i)}{S_j^u} + \epsilon_k V_{j,max}^u(i), \quad (4.19)$$

$$i = 1 : p, j = 1 : n_u$$

$$\frac{\Delta u_{j,min}(i)}{S_j^u} - \epsilon_k V_{j,min}^{\Delta u}(i) \leq \frac{\Delta u_j(k+i-1|k)}{S_j^u} \leq \frac{\Delta u_{j,max}(i)}{S_j^u} + \epsilon_k V_{j,max}^{\Delta u}(i), \quad (4.20)$$

$$i = 1 : p, j = 1 : n_u$$

where $Y_{j,min}(i)$ and $Y_{j,max}(i)$ are the constraints on outputs, $u_{j,min}(i)$ and $u_{j,max}(i)$ are the constraints on manipulated variables and $\Delta u_{j,min}(i)$ and $\Delta u_{j,max}(i)$ are the constraints on rate of change of manipulated variables.

In this work, the control step is defined as one engine cycle. The prediction horizon and control horizons for the MPC in this work are 5 and 2 engine cycles, respectively.

An adaptive MPC was used to achieve the control of CA50 and IMEP while keeping the MPRR restricted. The reason for using adaptive MPC is so that a single controller can be used with a changing LPV system. A built-in Kalman filter within the adaptive MPC is used to estimate the unmeasured states. The schematic of the MPC setup is shown in Fig. 4.3. The LPV subsystem updates the state space representation based on the value of the scheduling parameter, PR, at the beginning of every engine cycle. The adaptive MPC then manipulates SOI and FQ to track CA50 and IMEP along the reference values while maintaining the MPRR at a pre-determined limit. The built-in Kalman filter updates the adaptive MPC with the states of the plant at the beginning of every engine cycle.

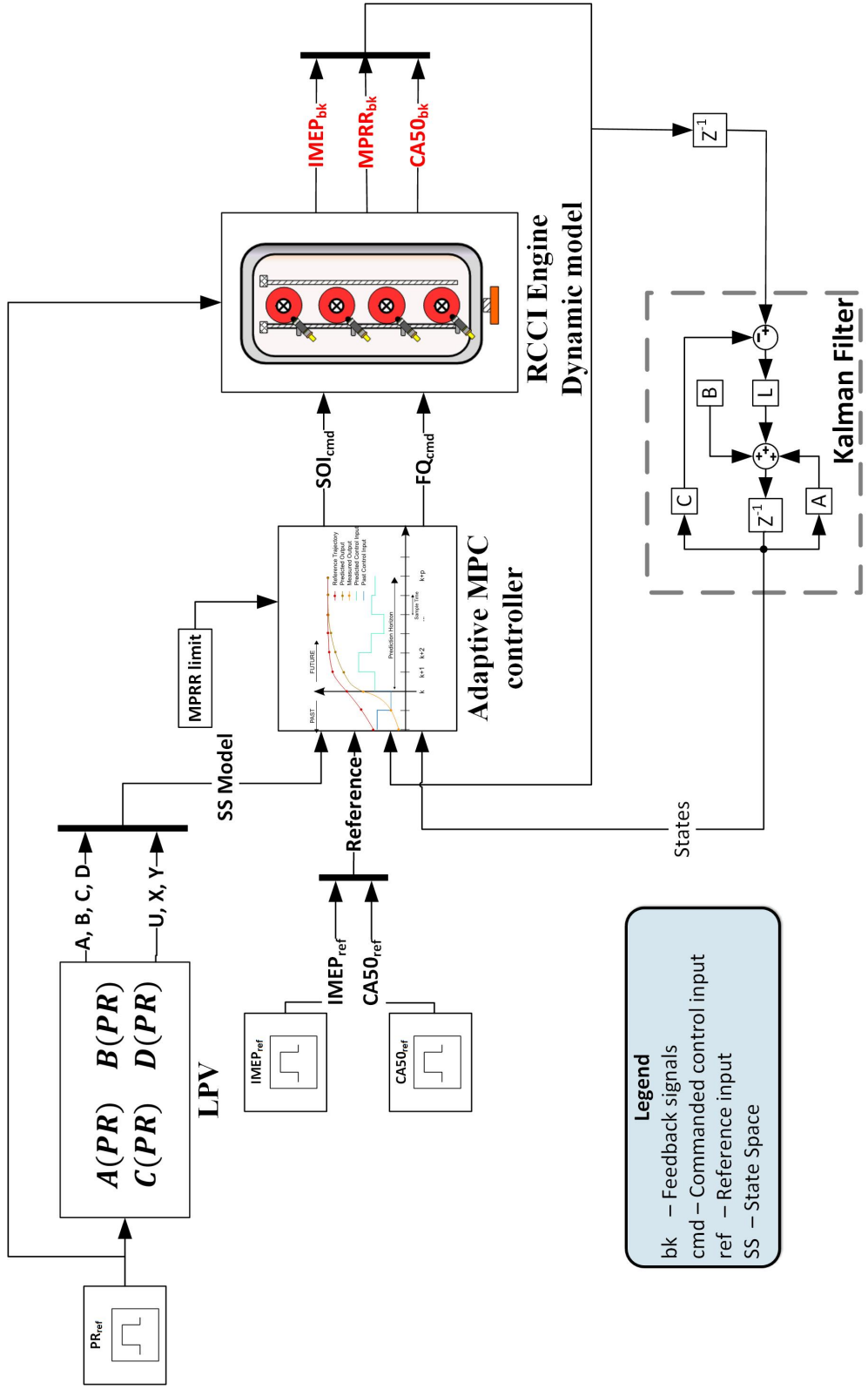


Figure 4.3: Schematic of the LPV - Adaptive MPC setup for controlling CA50 and IMEP with MPRR limitation

Input [units]	Min	Max
SOI [bTDC]	70	0
FQ [mg/cycle]	0	35

Table 4.1
Input constraints

Output [units]	Min	Max
CA50 [aTDC]	-20	20
MPRR [bar/CAD]	0	5.5
IMEP [KPa]	0	800

Table 4.2
Output constraints

Taking advantage of MPC's ability to constrain inputs and outputs, constraints have been applied on both inputs and outputs as shown in Tables 4.1 and 4.2

The constraints on SOI, FQ, CA50 and IMEP are based on the experimental data that was used to validate the RCCI engine dynamic model. The constraints on MPRR however are based on the desired limit for the Maximum Pressure Rise Rate. In order to test MPC's performance the limit for MPRR is chosen to be 5.8 bar/CAD based on the data used to generate the LPV system.

4.2.2 Tracking performance

The MPC is setup to track CA50 and IMEP along a reference signal. The results of the tracking are shown in Fig. 4.4. The MPC is able to track the required CA50 and IMEP with mean error of 0.3 and 4.9 KPa respectively. However, it can be seen that

at cycles 48 to 50, the MPRR exceeds 5.8 bar/CAD.

The MPC is now setup to track CA50 and IMEP while limiting the MPRR to 5.8 bar/CAD. The results of tracking are shown in Fig. 4.5. The MPC is able to track the required CA50 and IMEP with mean error of 0.4 CAD and 4.9 KPa respectively while keeping MPRR below 5.8 bar/CAD.

A measurement noise is then added into the CA50, IMEP and MPRR measurements to test the controller's performance. The dynamic RCCI engine model is then simulated with the MPC limiting the MPRR to 5.8 bar/CAD. The results of this simulation are shown in Fig. 4.6. It can be seen that the MPC is able to restrict the MPRR below 5.8 bar/CAD. The controller is able to track the desired CA50 and IMEP with an average error of 0.9 CAD and 4.7 KPa, respectively, while maintaining the MPRR below 5.8 bar/CAD.

However, when the controller is pushed by increasing the reference IMEP above 650 KPa (6.5 bar), the tracking performance of the controller decreases drastically as shown in Fig. 4.7(a). Though the MPC is able to restrict the MPRR to 5.8 bar/CAD, the performance of CA50 is heavily affected.

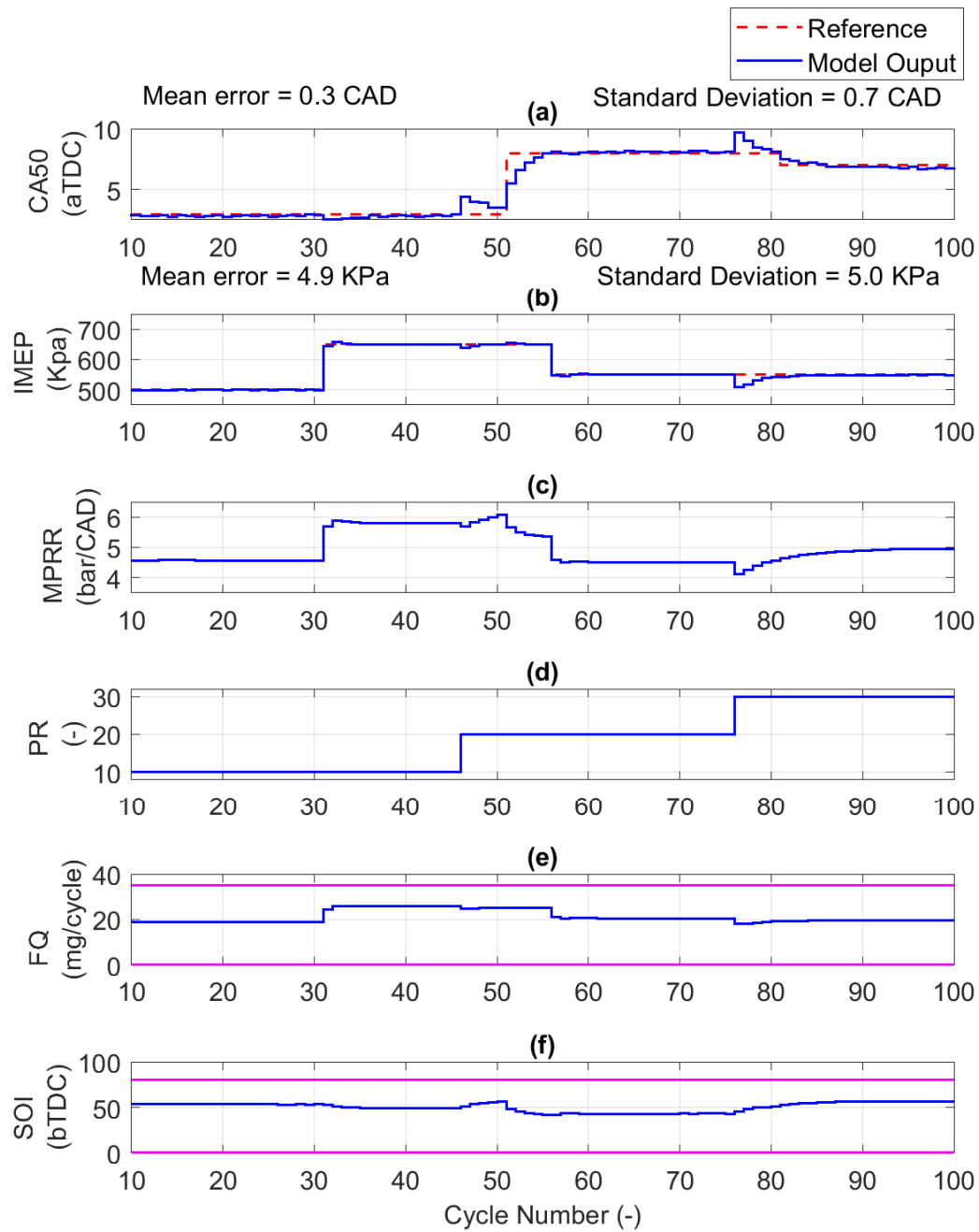


Figure 4.4: CA50 and IMEP tracking without MPRR limitation. Magenta colored dotted lines show the bounds for Inputs and Outputs

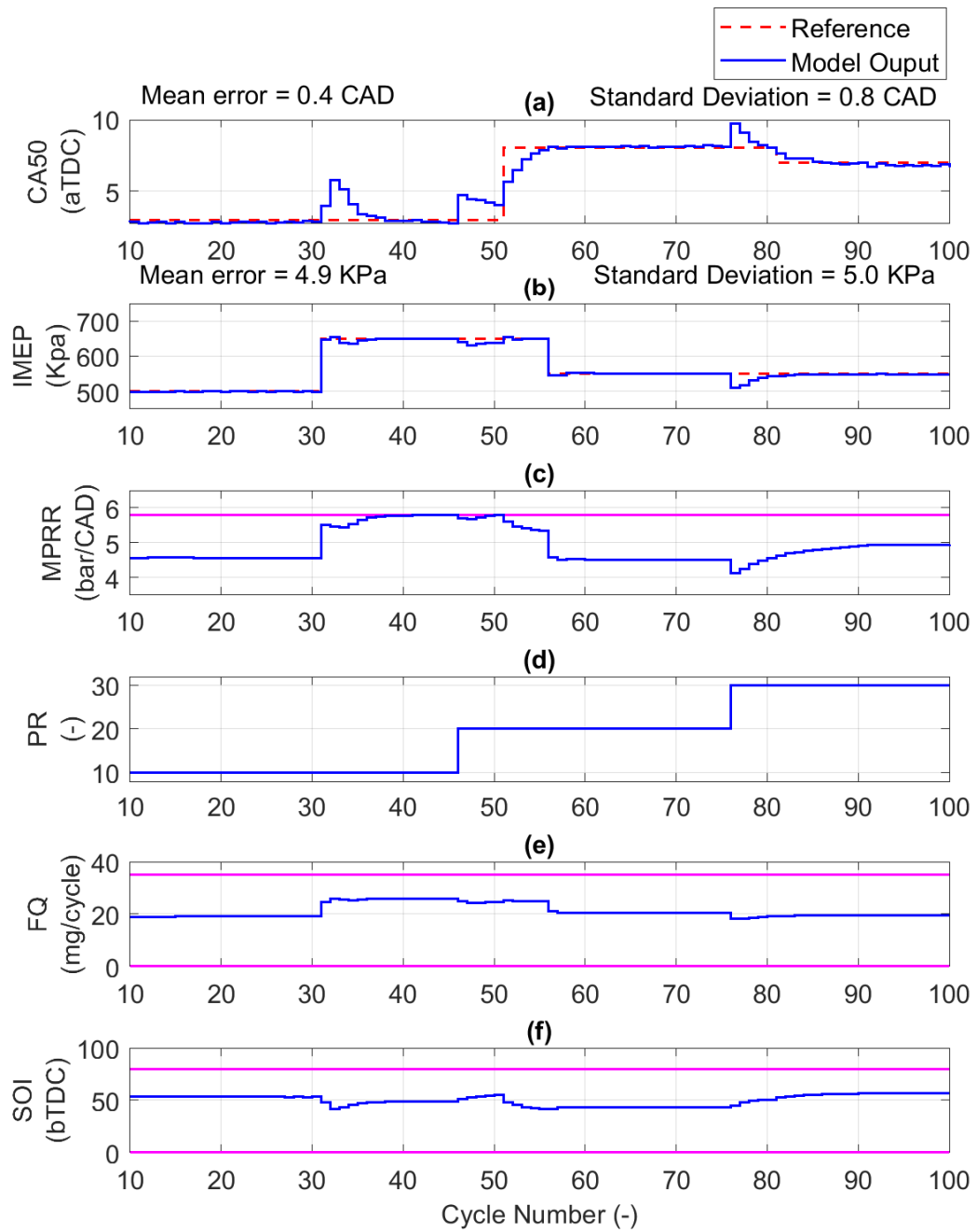


Figure 4.5: CA50 and IMEP tracking with MPRR limitation. Magenta colored dotted lines show the bounds for Inputs and Outputs

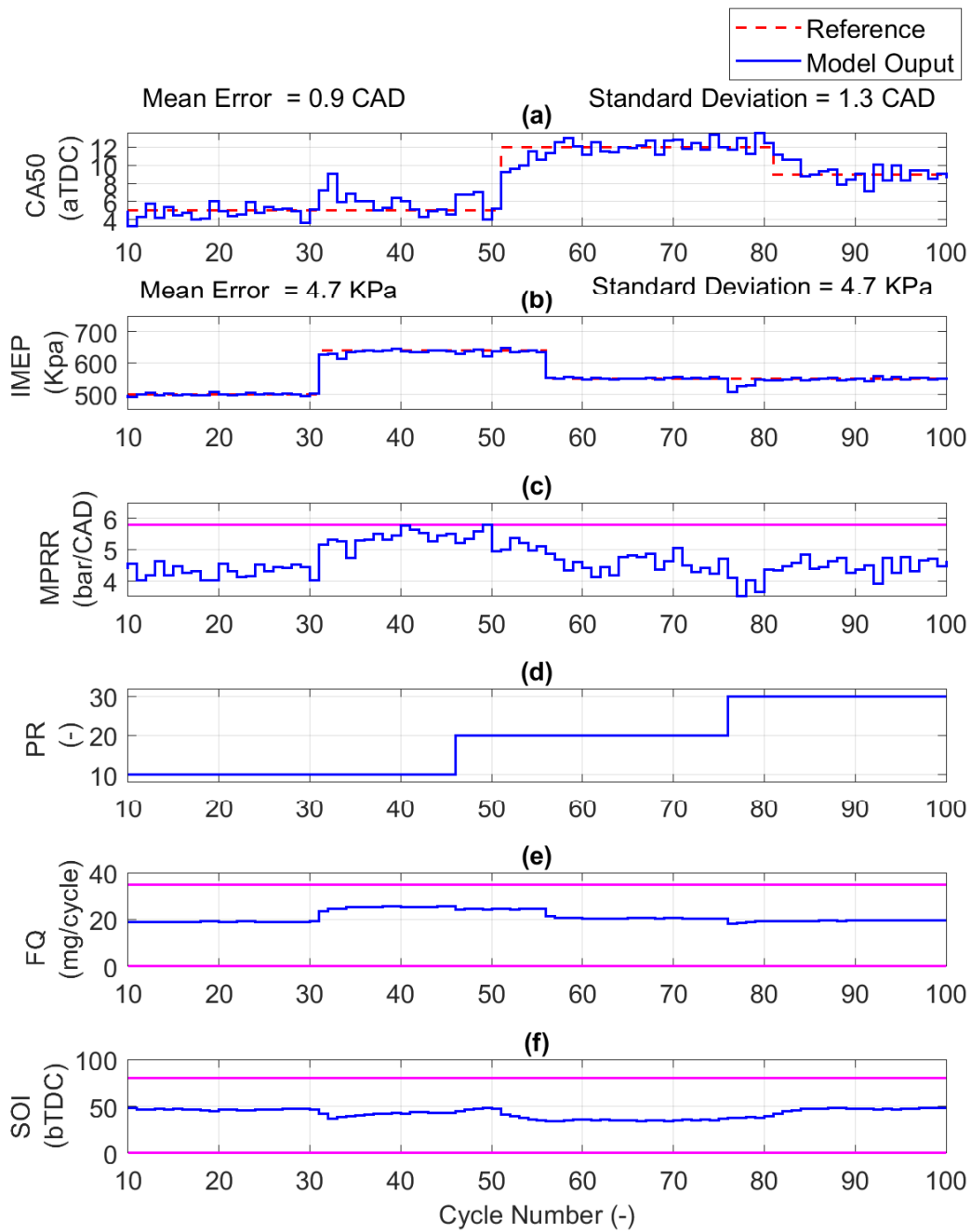


Figure 4.6: CA50 and IMEP tracking with MPRR limitation and noise. Magenta colored dotted lines show the bounds for Inputs and Outputs

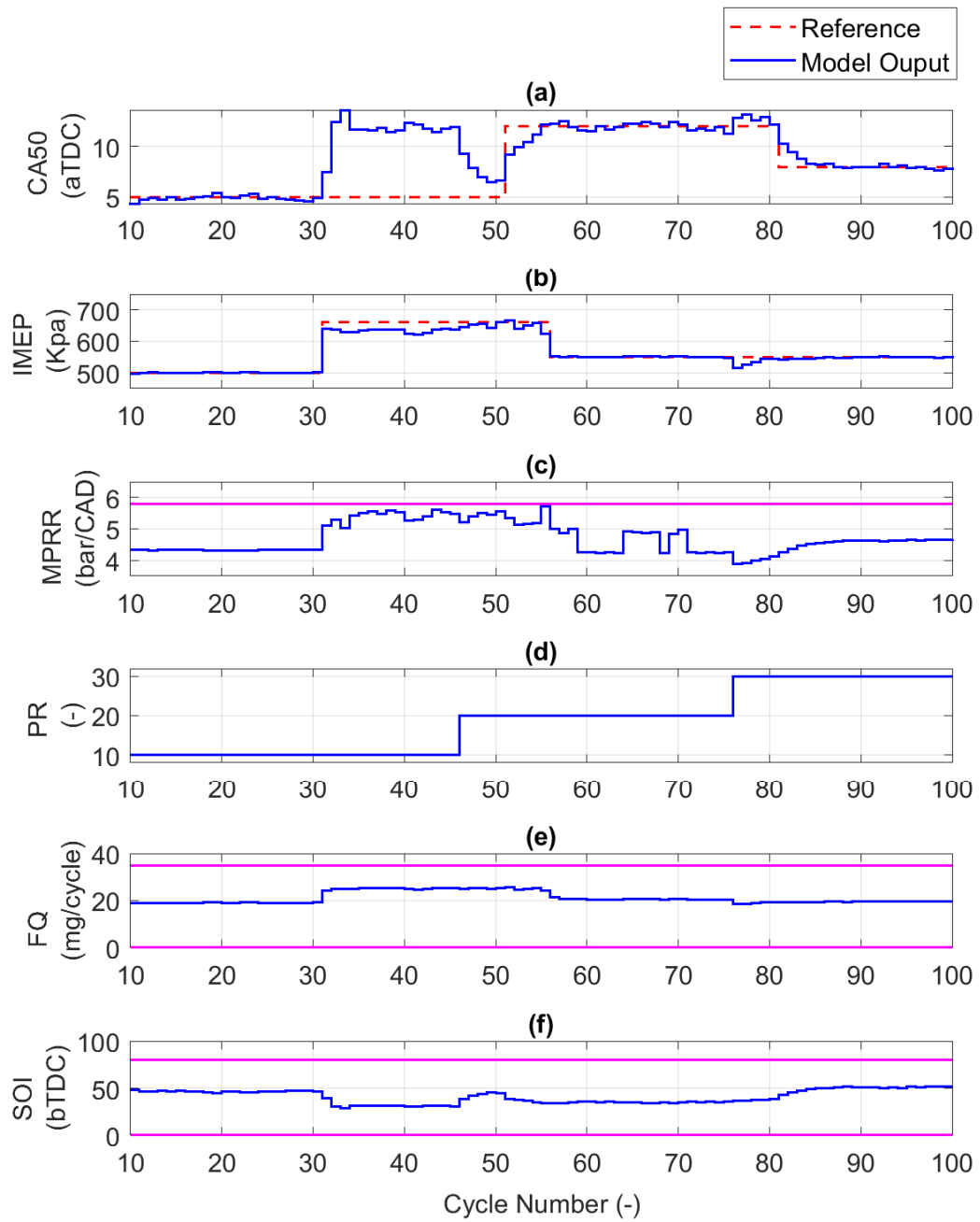


Figure 4.7: CA50 and IMEP tracking with MPRR limitation. Magenta colored dotted lines show the bounds for Inputs and Outputs.

4.3 Motivation for split DI fuel injection

As demonstrated in the previous Section 4.2.2 the MPC is able to restrict the MPRR to a set limit. However, when it is pushed to reach higher loads, it loses performance. The MPC has only two control variables and three controlled outputs. The two control variables, Start of Injection (SOI) and Fuel Quantity (FQ) control CA50 and IMEP directly. They both however affect MPRR too. When the SOI or the FQ is restricted in order to meet the MPRR restriction, the CA50 or IMEP tracking performance is lost. Hence, there is a need for a third control variable which would allow for the independent control of CA50, IMEP and MPRR. The proposed control variable for this purpose is split injection of the DI fuel.

By using two injections for the DI fuel and varying the amount of fuel in each injection, it can effectively vary the stratification inside the combustion chamber allowing for the control of MPRR and CA50 more independently.

Using split injections immediately affects the heat release rate profile within the cylinder. The key to modeling split injection as a COM for predicting MPRR and CA50 is to modify the existing MVM to represent the behaviour of split injection. This strategy of injection will affect the SOC, CA50 and MPRR directly. In order to capture the effects of split injection on CA50 and MPRR, the Wiebe function has to

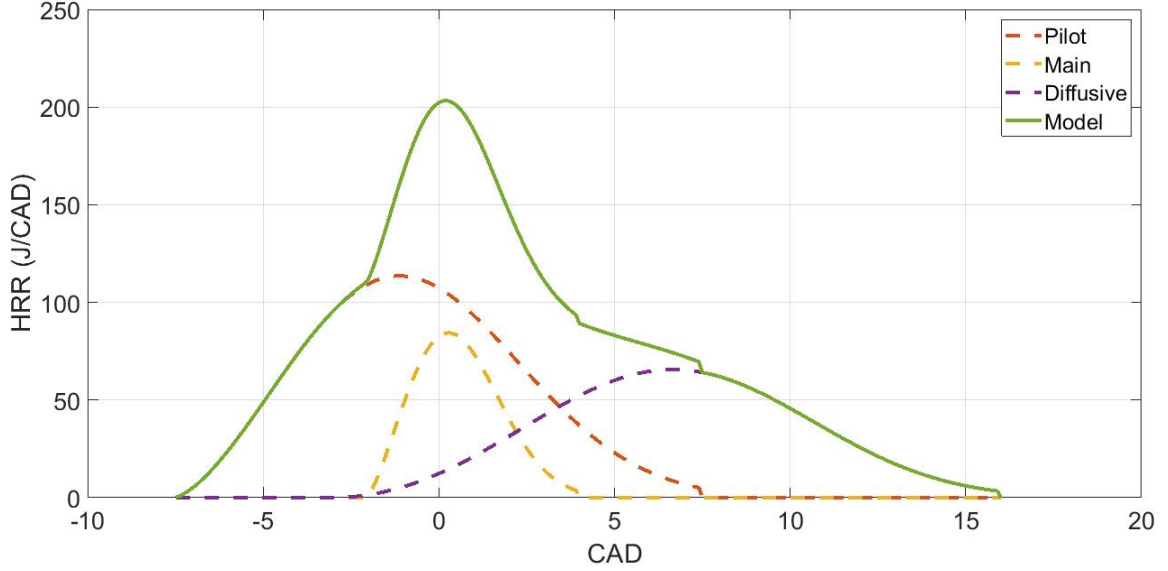


Figure 4.8: Heat Release Rate (HRR) modeling for split injection

be modified appropriately. Using a combination of multiple Wiebe functions based on the type of combustion can be effective for this application [83]. Since diffusive type combustion exists in RCCI combustion, a combination of three Wiebe functions with weighing factors based on the fuel quantity in each injection can be used to model the heat release rate during split injection. An example is shown in Fig. 4.8 where pilot fuel is the first injection and main refers to the second injection. The effect of split injection on SOC can be captured by modifying the MKIM presented in Section 3.3 to include the variation in ϕ_{di} and CN_{mix} with the injection timing. Due to lack of experimental data on DI split injection in RCCI engines, this thesis does not include the MPRR control using fuel injection split. However, the concept of the model is presented in Appendix A and the controller development is the subject of future studies.

Chapter 5

Conclusions and Future work

5.1 Summary and Conclusions

In this work, a model for predicting the MPRR has been developed and included into an existing dynamic RCCI engine model. This model was then used to develop an MPC to control the RCCI engine model. Major contributions/findings from this work are presented below.

† An experimental study was conducted on a modified 2.0L Ecotec engine capable of RCCI combustion under naturally aspirated conditions. The pressure trace from the combustion was analyzed to understand the effects of input parameters

on the Maximum Pressure Rise Rate during combustion. It was found that SOI had a significant impact on the MPRR as earlier SOI led to higher MPRR. FQ and PR also had an effect on MPRR but their effects were more complex and dependant on SOI.

† Another experimental analysis was performed to develop a combination of combustion or input parameters that would characterize the heat release curves during combustion. It was found that by using a combination of combustion parameters such as ϕ_{pfi} , X_{rg} along with input parameters, SOI and PR, different combustion regimes' operating points during RCCI combustion can be separated. A summary of findings is given in Appendix B.

† A Control Oriented Model was developed for predicting the MPRR. A comparison of double Wiebe function and single Wiebe function based mass fraction burn profiles was conducted to determine which one was appropriate for the purpose. The single Wiebe function was able to predict the MPRR with similar accuracy as the double Wiebe function; thus, single wiebe function was favored due its simplicity.

† An MPRR prediction model was developed using the first law of thermodynamics. The model was able to predict the MPRR with an average accuracy of 0.7 bar/CAD in steady state conditions and 1.5 bar/CAD in transient conditions. This MPRR model was combined with an existing validated dynamic RCCI engine model which included transient dynamics of residual gas and fuel

transport.

† Using advanced techniques of machine learning and Support Vector Machines (SVM) a data-driven LPV control model of RCCI including MPRR was developed. The LPV model uses the PR as the scheduling parameter. The model was validated with the data generated by the dynamic RCCI engine model. It was able to predict the CA50, IMEP and MPRR with average errors of 0.9 CAD, 3.3 KPa and 0.5 bar/CAD, respectively.

† A Multi Input Multi Output MPC was developed to work with the LPV representation of the dynamic RCCI engine model. It was developed with a 5-step prediction horizon and 2-step control horizon. Constraints were implemented on the Manipulated Variables and the Controlled Variables. The controller was able to track the CA50 and IMEP as required while keeping the MPRR below 5.5 bar/CAD. The average tracking errors for CA50 and IMEP were 1 CAD and 4.6 KPa, respectively.

† The MPC was able to control CA50 and IMEP while limiting MPRR only in a small operating range. When the reference IMEP was increased beyond 6.5 bar, the MPC would lose performance on CA50 tracking while maintaining the MPRR limit. This is because the number of controlled variables is three and the number of manipulated variables is two. Hence, there is a need to develop a third manipulated variable which would help control CA50, IMEP and MPRR independently.

5.2 Future work

Based on the findings of this work, a few areas can be further explored in order to improve the outcomes. They are listed as follows:

- † The MPC developed can be deployed on a rapid prototyping system in the engine test cell to validate its performance experimentally.
- † A split injection control strategy can be explored in order to develop an additional manipulated variable that can be used to control the CA50, IMEP and MPRR independently.
- † It has been shown in previous work that PR can be a good manipulated variable for CA50 control in certain conditions [3, 4]. Since, the PR is used as a scheduling parameter in this work, it cannot be used as a manipulated variable. Hence, if a new scheduling parameter can be found for the LPV representation, it would allow for the use of both PR and SOI to control CA50 and MPRR. The results presented in the Appendix A can be of utility for this purpose.
- † A stochastic MPC can be developed to account for the cyclic variability of MPRR. The experimental analysis presented in Fig. 2.5 represents the cyclic variability as a function of the input parameters. This can be used to develop a model to account for the variability in MPRR. The same study can help

develop a noise model for the Kalman filter that can help tackle the variability in MPRR.

† Using the results presented in Fig. 2.5, the state space coefficient $K(p_k)$ shown in Eq. (3.45) can be developed. The data driven approach can account for the variation in MPRR as a noise and model that can be built into the LPV representation. This would help develop an MPC that can accurately predict the MPRR at each engine cycle.

† Given the successful implementation of the data driven system identification method, it can be used to develop an LPV system for exhaust gas temperature and engine-out emissions. This can then be used to develop an MPC to restrict the tailpipe emissions or maintain the minimum required exhaust gas temperature to avoid the light-off of the after treatment components.

References

- [1] Kaveh Khodadadi Sadabadi. Modelling and Control of Combustion Phasing of an RCCI Engine. Master's thesis, Michigan Technological University, 2015.
- [2] Kaushik Kannan. An Experimental Investigation of Low Temperature Combustion Regimes in a Light Duty Engine. Master's thesis, Michigan Technological University, 2016.
- [3] Naga Nithin Kondipati. Experimental Study, Modelling and Controller for an RCCI Engine. Master's thesis, Michigan Technological University, 2017.
- [4] Akshat Abhay Raut. Model Based Control of RCCI Engine. Master's thesis, Michigan Technological University, 2017.
- [5] Behrouz K Irdamouza, Syed Z. Rizvi, Javad Mohammadpour Velni, Jeffrey D. Naber, and Mahdi Shahbakhti. Data-Driven Modeling and Predictive Control of Combustion Phasing for RCCI Engines. In *2019 Annual American Control Conference (ACC)*, Pittsburgh, Pennsylvania. IEEE.

- [6] Syed Z Rizvi, Javad Mohammadpour, Roland Tóth, and Nader Meskin. A Kernel-Based Approach to MIMO LPV State-Space Identification and Application to a Nonlinear Process System. *IFAC-PapersOnLine*, 48(26):85–90, 2015.
- [7] United States EIA. EIA Total Energy August Monthly Data. *Energy Information Administration (EIA)*, 8, 2018.
- [8] Independent Statistics and Analysis. *Energy Use for Transportation - Energy Explained, Your Guide To Understanding Energy - Energy Information Administration*. U.S. Energy Information Administration, 2018.
- [9] Daniel Mendoza, Kevin Robert Gurney, Igor Razlivanov, Sarath Geethakumar, Vandhana Chandrasekaran, and Yuyu Zhou. US Onroad Transportation CO2 Emissions Analysis Comparing Highly-Resolved CO2 Emissions and a National Average Approach: Mitigation Options and Uncertainty Reductions. In *American Geophysical Union (AGU) Fall Meeting Abstracts*, 2011.
- [10] EPA USEPA. Inventory of USA Greenhouse Gas Emissions and Sinks: 1990–2013. *Washington, DC, USA, EPA*, 2015.
- [11] U.S. White House Office of the Press Secretary. *Obama Administration Finalizes Historic 54.5 MPG Fuel Efficiency Standards*. U.S Office of the President, 2012.
- [12] Adam Sieminski et al. International Energy Outlook. *Energy Information Administration (EIA)*, 18, 2014.

- [13] Phase 2; Board on Energy Committee on the Assessment of Technologies for Improving Fuel Economy of Light-Duty Vehicles, Environmental Systems; Division on Engineering, and Physical Sciences; National Research Council. *Cost, Effectiveness and Deployment of Fuel Economy Technologies for Light-Duty Vehicles*. National Research Council, 2015.
- [14] J.B.Heywood. *Internal Combustion Engines Fundamentals, Chapter 11*. McGraw-hill New York, 1988.
- [15] Christof Noehre, Magnus Andersson, Bengt Johansson, and Anders Hultqvist. Characterization of Partially Premixed Combustion. Technical report, SAE Technical Paper, 2006.
- [16] Martin Tunér, Karin Frojd, Lars Seidel, and Fabian Mauss. Diesel-PPC engine: Predictive Full Cycle Modeling with Reduced and Detailed Chemistry. Technical report, SAE Technical Paper, 2011.
- [17] A.B. Dempsey. *Dual Fuel Reactivity Controlled Compression Ignition (RCCI) with Alternative Fuels*. PhD thesis, University of Wisconsin - Madison, 2013.
- [18] D. Foster. *Low Temperature Combustion-A Thermodynamic Pathway to High Efficiency Engines*. National Petroleum Council Fuels Study, 2012.
- [19] D.Splitter, R.Hanson, and S.Kokjohn. *Improving Engine Performance by Optimizing Fuel Reactivity with a Dual Fuel PCCI Strategy*. Conference on Thermo and Fluid Dynamic Process in Diesel Engines, 2010.

- [20] R.Hasegawa and H.Yahagihara. *HCCI Combustion in DI Diesel Engine*. SAE Technical paper 2013-01-0745, 2003.
- [21] G.Shibata, K.Oyama, T.Urushihara, and T.Nakano. *Correlation of Low Temperature Heat Release With Fuel Composition and HCCI Engine Combustion*. SAE Technical paper 2005-01-0138, 2005.
- [22] R.Opat, Y.Ra M.Gonzalez, R.Krieger, R.Reitz, and D.Foster. *Investigation of Mixing and Temperature Effects on HC/CO Emissions for Highly Dilute Low Temperature Combustion in a Light Duty Diesel Engine*. SAE Technical paper 2007-01-0193, 2007.
- [23] S.Kokjohn, R.Hanson, D.Splitter, and R.Reitz. *Experiments and Modeling of Dual-Fuel HCCI and PCCI Combustion using In-Cylinder Fuel Blending*. SAE International Journal of Engines,2(2):24-39, 2009.
- [24] K.Inagaki, T.Fuyuto, K.Nishikawa, K.Nakakita, and I.Sakata. *Dual-Fuel PCI Combustion Controlled by In-Cylinder Stratification of Ignitability*. SAE Technical paper 2006-01-0028, 2006.
- [25] S.Kokjohn, R.Hanson, D.Splitter, and R.Reitz. *Fuel Reactivity Controlled Compression Ignition(RCCI): A Pathway to Controlled High-Efficiency Clean Combustion*. International Journal of Engine Research, 12(3):209-226, 2011.
- [26] A.Paykani, A.Kakae, P.Rahnama, and R.Reitz. *Progress and Recent Trends*

- in Reactivity-Controlled Compression Ignition Engines*. International Journal of Engine Research, 17(5):481-524, 2016.
- [27] S.Kokjohn and R.Reitz. *Reactivity Controlled Compression Ignition and Conventional Diesel Combustion: A Comparison of Methods to Meet Light-Duty NOx and Fuel Economy Targets*. International Journal of Engine Research, 14(5):452-468, 2013.
- [28] S.Curran, R.Hanson, R.Wagner, and R.Reitz. *Efficiency and Emissions Mapping of RCCI in a Light-Duty Diesel Engine*. SAE Technical Paper 2013-01-0289, 2013.
- [29] Jan-Ola Olsson, Per Tunestål, and Bengt Johansson. Closed-Loop Control of an HCCI Engine. Technical report, SAE Technical Paper, 2001.
- [30] M. Fathi, O. Jahanian, and M. Shahbakhti. Modeling and Controller Design Architecture for Cycle-by-Cycle Combustion Control of Homogeneous Charge Compression Ignition (HCCI) Engines - A Comprehensive Review . *Energy Conversion and Management*, 139:1–19, 2017.
- [31] Amin Paykani, Amir-Hasan Kakaee, Pourya Rahnama, and Rolf D Reitz. Progress and Recent Trends in Reactivity-Controlled Compression Ignition Engines. *International Journal of Engine Research*, 17(5):481–524, 2016.
- [32] Gautam T Kalghatgi, Per Risberg, and Hans-Erik Ångström. Partially Premixed Auto-ignition of Gasoline to attain Low Smoke and Low NOx at High

- Load in a Compression Ignition Engine and Comparison with a Diesel Fuel. Technical report, SAE Technical paper, 2007.
- [33] Paul W Bessonette, Charles H Schleyer, Kevin P Duffy, William L Hardy, and Michael P Liechty. Effects of Fuel Property Changes on Heavy-Duty HCCI Combustion. Technical report, SAE Technical paper, 2007.
- [34] Kamran Poorghasemi, Rahim Khoshbakhti Saray, Ehsan Ansari, Behrouz Khoshbakht Irdmousa, Mehdi Shahbakhti, and Jeffery D Naber. Effect of Diesel Injection Strategies on Natural Gas/Diesel RCCI Combustion Characteristics in a Light Duty Diesel Engine. *Applied Energy*, 199:430–446, 2017.
- [35] Maciej Mikulski and Cemil Bekdemir. Understanding the Role of Low Reactivity Fuel Stratification in a Dual Fuel RCCI Engine—A Simulation Study. *Applied energy*, 191:689–708, 2017.
- [36] Jing Li, Xiang Ling, Deng Liu, Wenming Yang, and Dezhi Zhou. Numerical Study on Double Injection Techniques in a Gasoline and Biodiesel Fueled RCCI (Reactivity Controlled Compression Ignition) Engine. *Applied Energy*, 211:382–392, 2018.
- [37] Jesús Benajes, Santiago Molina, Antonio García, and Javier Monsalve-Serrano. Effects of Low Reactivity Fuel Characteristics and Blending Ratio on Low Load

- RCCI (Reactivity Controlled Compression Ignition) Performance and Emissions in a Heavy-Duty Diesel Engine. *Energy*, 90:1261–1271, 2015.
- [38] Vinícius B Pedrozo, Ian May, Macklini Dalla Nora, Alasdair Cairns, and Hua Zhao. Experimental Analysis of Ethanol Dual-Fuel Combustion in a Heavy-Duty Diesel Engine: An Optimisation at Low Load. *Applied Energy*, 165:166–182, 2016.
- [39] Jesús Benajes, Antonio García, Javier Monsalve-Serrano, and Vicente Boronat. Achieving Clean and Efficient Engine Operation up to Full Load by Combining Optimized RCCI and Dual-Fuel Diesel-Gasoline Combustion Strategies. *Energy conversion and management*, 136:142–151, 2017.
- [40] Guangfu Xu, Ming Jia, Yaopeng Li, Yachao Chang, and Tianyou Wang. Potential of Reactivity Controlled Compression Ignition (RCCI) Combustion Coupled with Variable Valve Timing (VVT) Strategy for Meeting Euro 6 Emission Regulations and High Fuel Efficiency in a Heavy-Duty Diesel Engine. *Energy Conversion and Management*, 171:683–698, 2018.
- [41] Derek E Nieman, Adam B Dempsey, and Rolf D Reitz. Heavy-Duty RCCI Operation Using Natural Gas and Diesel. *SAE International Journal of Engines*, 5(2):270–285, 2012.
- [42] Amir-Hasan Kakaee, Pourya Rahnama, and Amin Paykani. Influence of Fuel Composition on Combustion and Emissions Characteristics of Natural

- Gas/Diesel RCCI Engine. *Journal of natural gas science and engineering*, 25:58–65, 2015.
- [43] Jesús Benajes, Antonio García, Javier Monsalve-Serrano, and Rafael Lago Sari. Fuel Consumption and Engine-Out Emissions Estimations of a Light-Duty Engine Running in Dual-Mode RCCI/CDC with Different Fuels and Driving Cycles. *Energy*, 157:19–30, 2018.
- [44] Amir-Hasan Kakaee, Ali Nasiri-Toosi, Babak Partovi, and Amin Paykani. Effects of Piston Bowl Geometry on Combustion and Emissions Characteristics of a Natural Gas/Diesel RCCI Engine. *Applied Thermal Engineering*, 102:1462–1472, 2016.
- [45] Adam B Dempsey, N Ryan Walker, and Rolf Reitz. Effect of Piston Bowl Geometry on Dual Fuel Reactivity Controlled Compression Ignition (RCCI) in a Light-Duty Engine Operated with Gasoline/Diesel and Methanol/Diesel. *SAE International Journal of Engines*, 6(1):78–100, 2013.
- [46] Antonio García, Javier Monsalve-Serrano, Vinícius Rückert Roso, and Mario Eduardo Santos Martins. Evaluating the Emissions and Performance of two Dual-Mode RCCI Combustion Strategies under the World Harmonized Vehicle Cycle (WHVC). *Energy Conversion and Management*, 149:263–274, 2017.
- [47] Jesús Benajes, Antonio García, Javier Monsalve-Serrano, Iyad Balloul, and

- G erard Pradel. An Assessment of the Dual-Mode Reactivity Controlled Compression Ignition/Conventional Diesel Combustion Capabilities in a EURO VI Medium-Duty Diesel Engine Fueled with an Intermediate Ethanol-Gasoline Blend and Biodiesel. *Energy Conversion and Management*, 123:381–391, 2016.
- [48] Mahdi Shahbakhti and Charles Robert Koch. Dynamic Modeling of HCCI Combustion Timing in Transient Fueling Operation. *SAE International Journal of Engines*, 2(1):1098–1113, 2009.
- [49] Charles F Aquino. Transient A/F Control Characteristics of the 5 Liter Central Fuel Injection Engine. *SAE Transactions*, pages 1819–1833, 1981.
- [50] Yifeng Wu, Reed Hanson, and Rolf D Reitz. Investigation of Combustion Phasing Control Strategy during Reactivity Controlled Compression Ignition (RCCI) Multicylinder Engine Load Transitions. *Journal of Engineering for Gas Turbines and Power*, 136(9):091511, 2014.
- [51] Armando Indrajuana, Cemil Bekdemir, Xi Luo, and Frank Willems. Robust Multivariable Feedback Control of Natural Gas-Diesel RCCI Combustion. *IFAC-PapersOnLine*, 49(11):217–222, 2016.
- [52] A Indrajuana, C Bekdemir, E Feru, and F Willems. Towards Model-Based control of RCCI-CDF Mode-Switching in Dual Fuel Engines. *SAE Technical Paper*, pages 01–0263, 2018.

- [53] Jayant Kumar Arora. Design of Real-time Combustion Feedback System and Experimental Study of an RCCI Engine for Control. Master's thesis, Michigan Technological University, 2016.
- [54] JC Livengood and PC Wu. Correlation of Autoignition Phenomena in Internal Combustion Engines and Rapid Compression Machines. In *Symposium (international) on combustion*, volume 5, pages 347–356. Elsevier, 1955.
- [55] Ivan Arsie, Fausto Di Genova, Armando Mogavero, Cesare Pianese, Gianfranco Rizzo, Antonello Caraceni, Piero Cioffi, and G Flauti. Multi-Zone Predictive Modeling of Common Rail Multi-Injection Diesel Engines. Technical report, SAE Technical Paper, 2006.
- [56] Mahdi Shahbakhti. Modeling and Experimental Study of an HCCI Engine for Combustion Timing Control. 2009.
- [57] Akshat Raut, Mehran Bidarvatan, Hoseinali Borhan, and Mahdi Shahbakhti. Model Predictive Control of an RCCI Engine. In *2018 Annual American Control Conference (ACC)*, pages 1604–1609. IEEE, 2018.
- [58] Cemil Bekdemir, Rik Baert, Frank Willems, and Bart Somers. Towards control-Oriented Modeling of Natural Gas-Diesel RCCI Combustion. Technical report, SAE Technical Paper, 2015.
- [59] Maciej Mikulski, C Bekdemir, and F Willems. Experimental Validation of a

- Combustion Kinetics based Multi-Zone Model for Natural Gas-Diesel RCCI Engines. In *Symposium for Combustion Control 2016, June 15-16, 2016, Aachen, Germany*, 2016.
- [60] DT Hountalas and RG Papagiannakis. Theoretical and Experimental Investigation of a Direct Injection Dual Fuel Diesel-Natural Gas Engine. Technical report, SAE Technical Paper, 2002.
- [61] RG Papagiannakis, PN Kotsiopoulos, TC Zannis, EA Yfantis, DT Hountalas, and CD Rakopoulos. Theoretical Study of the Effects of Engine Parameters on Performance and Emissions of a Pilot Ignited Natural Gas Diesel Engine. *Energy*, 35(2):1129–1138, 2010.
- [62] F Payri, A Broatch, B Tormos, and V Marant. New Methodology for In-Cylinder Pressure Analysis in Direct Injection Diesel Engines Application to Combustion Noise. *Measurement Science and Technology*, 16(2):540, 2005.
- [63] Stefan Byttner, Thorsteinn Rögnvaldsson, and Nicholas Wickström. Estimation of Combustion Variability using In-Cylinder Ionization Measurements. Technical report, SAE Technical Paper, 2001.
- [64] J.B.Heywood. *Internal Combustion Engines Fundamentals, Chapter 2*. Mcgraw-hill New York, 1988.
- [65] David T Klos and Sage L Kokjohn. Investigation of the Effect of Injection and

- Control Strategies on Combustion Instability in Reactivity-Controlled Compression Ignition Engines. *Journal of Engineering for Gas Turbines and Power*, 138(1):011502, 2016.
- [66] Sage Lucas Kokjohn. *Reactivity Controlled Compression Ignition (RCCI) Combustion*. PhD thesis, The University of Wisconsin-Madison, 2012.
- [67] AH Kakaee, P Rahnama, and A Paykani. Numerical Study of Reactivity Controlled Compression Ignition (RCCI) Combustion in a Heavy-Duty Diesel Engine using 3D-CFD Coupled with Chemical Kinetics. *International Journal of Automotive Engineering*, 4(3):792–804, 2014.
- [68] William J Glewen, Robert M Wagner, K Dean Edwards, and C Stuart Daw. Analysis of Cyclic Variability in Spark-Assisted HCCI Combustion using a Double Wiebe Function. *Proceedings of the Combustion Institute*, 32(2):2885–2892, 2009.
- [69] Puneet Valecha, Chinmaya Mishra, PMV Subbarao, and Pranab Das. Development of Improved Thermodynamic Model Using Cylinder Blow by and Double-Wiebe Functions for High Speed Diesel Engine. Technical report, SAE Technical Paper, 2018.
- [70] Gabriel Ingesson, Lianhao Yin, Rolf Johansson, and Per Tunestål. Efficiency Optimal, Maximum-Pressure Control in Compression-Ignition Engines. In *2017 American Control Conference (ACC)*, pages 4753–4759. IEEE, 2017.

- [71] H Yasar, HS Soyhan, H Walmsley, B Head, and C Sorousbay. Double-Wiebe Function: An Approach for Single-Zone HCCI Engine Modeling. *Applied Thermal Engineering*, 28(11-12):1284–1290, 2008.
- [72] Yeliana Yeliana, C Cooney, J Worm, DJ Michalek, and JD Naber. Estimation of Double-Wiebe Function Parameters using Least Square Method for Burn Durations of Ethanol-Gasoline Blends in Spark Ignition Engine Over Variable Compression Ratios and EGR Levels. *Applied Thermal Engineering*, 31(14-15):2213–2220, 2011.
- [73] Maciej Mikulski and Sławomir Wierzbicki. Numerical Investigation of the Impact of Gas Composition on the Combustion Process in a Dual-Fuel Compression-Ignition Engine. *Journal of Natural Gas Science and Engineering*, 31:525–537, 2016.
- [74] Junseok Chang, Orgun Güralp, Zoran Filipi, Dennis Assanis, Tang-Wei Kuo, Paul Najt, and Rod Rask. New Heat Transfer Correlation for an HCCI Engine Derived from Measurements of Instantaneous Surface Heat Flux. *SAE transactions*, pages 1576–1593, 2004.
- [75] II Vibe. Semi-empirical expression for combustion rate in engines. In *Proceedings of Conference on piston engines, USSR Academy of sciences, Moscow*, pages 185–191, 1956.

- [76] Friedrich Pukelsheim. The Three Sigma Rule. *The American Statistician*, 48(2):88–91, 1994.
- [77] Mehran Bidarvatan. Physics-Based Modeling and Control of Powertrain Systems Integrated with Low Temperature Combustion Engines. 2015.
- [78] Nicolò Cavina, Carlo Siviero, and Rosanna Suglia. Residual Gas Fraction Estimation: Application to a GDI Engine with Variable Valve Timing and EGR. *SAE transactions*, pages 1774–1782, 2004.
- [79] J.B.Heywood. *Internal Combustion Engines Fundamentals, Chapter 5*. Mcgraw-hill New York, 1988.
- [80] DJ Rausen, AG Stefanopoulou, J-M Kang, JA Eng, and T-W Kuo. A Mean-Value Model for Control of Homogeneous Charge Compression Ignition (HCCI) Engines. *Journal of Dynamic Systems, Measurement, and Control*, 127(3):355–362, 2005.
- [81] D Solomatine, Linda M See, and RJ Abrahart. Data-Driven Modelling: Concepts, Approaches and Experiences. In *Practical Hydroinformatics*, pages 17–30. Springer, 2009.
- [82] Johan AK Suykens and Joos Vandewalle. Least Squares Support Vector Machine Classifiers. *Neural processing letters*, 9(3):293–300, 1999.

- [83] Fabrizio Ponti, Enrico Corti, Gabriele Serra, and Matteo De Cesare. Common Rail Multi-Jet Diesel Engine Combustion Model Development for Control Purposes. Technical report, SAE Technical Paper, 2007.

Appendix A

Control Oriented Modeling of split injection in RCCI engines

From section 4.2.2, it is evident that a single injection is not sufficient to control MPRR and CA50 independently. Hence a split injection strategy for Direct Injection is proposed. Using 2 injections brings in multiple parameters for control such as the injection timing and the ratio of fuels injected in each injection. The parameters used to define split injection are listed below:

1. **Pilot injection:** It is the first injection after IVC.
2. **Main injection:** It is the second injection after IVC. It can occur at any time after the pilot injection has ended.

3. **Ratio of fuel injected to total fuel (ρ):** The amount of fuel injected in each injection is represented using Eq. A.1 and A.2

$$\rho_{pilot} = \frac{FQ_{pilot}}{FQ_{DI}}.100 \quad (\text{A.1})$$

$$\rho_{main} = \frac{FQ_{main}}{FQ_{DI}}.100 \quad (\text{A.2})$$

Using the parameters defined above, split injection can be easily described.

A.1 Wiebe function modeling for Split injection

As presented in this work a wiebe function can be used to model the MFB and consequently the heat release rate from the fuel. However, when there are two injections involved, a single wiebe function is not sufficient to model the heat release curve. It requires the use of multiple wiebe functions. Each Direct Injection can be represented using a wiebe function. If the combustion has a diffusive behaviour then an additional wiebe function is required to model it [83]. Since, RCCI combustion has diffusive type behaviour, 3 wiebe functions have to be used to model split injection. Eq. A.3 represents the equation that is used to model the wiebe function for split

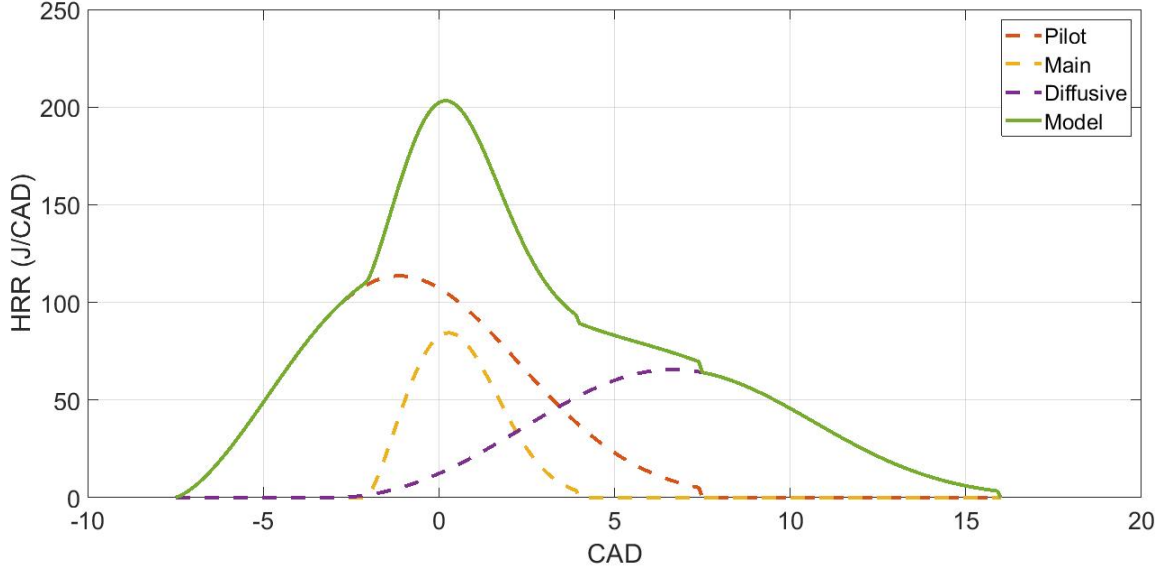


Figure A.1: HRR modeling for split injection

injection.

$$X_b(\theta) = \sum_{i=1}^{i=3} p_i \cdot \left(1 - \exp \left[- \left(\frac{\theta - \theta_{SOC_i}}{\alpha \Delta \theta_i} \right)^{m_i} \right] \right) \quad (\text{A.3})$$

where $i = 1, 2, 3$ represent the wiebe function for pilot, main and diffusive combustion respectively. Also,

$$\sum_{i=1}^3 p_i = 1 \quad (\text{A.4})$$

An example for split injection modeling with 3 wiebe functions is shown in Fig. A.1

A.2 Modifying MKIM for split injection

θ_{soc} for each wiebe function are predicted by modifying the MKIM presented in section 3.3. The MKIM currently being used for single injection is shown in Eq. A.5

$$\int_{SOI}^{SOC} \frac{d\theta}{A_2 N (\phi_{DI}^{B_{2DI}} + \phi_{PFI}^{B_{2PFI}}) \exp\left(\frac{C_2}{CN_{mix} + b} \frac{(P_{ivc} v_c^{n_c})^D}{T_{ivc} v_c^{n_c - 1}}\right)} + \int_{IVC}^{SOI} \frac{d\theta}{A_1 N \phi_{PFI}^B \exp\left(\frac{C_1 (P_{ivc} v_c^{n_c})^{D_1}}{T_{ivc} v_c^{n_c - 1}}\right)} = 1 \quad (A.5)$$

When the MKIM is used for single injection, the assumption is that the ϕ_{DI} doesn't change from *SOI* to *SOC*. However, when split injection is used, the amount of DI fuel in the combustion chamber varies from SOI_{pilot} to *SOC*. This also affects the CN_{mix} . Hence, they both have to be defined as a function of θ .

$$\phi_{DI} = \begin{cases} \phi_{DI_{pilot}} & SOI_{pilot} < \theta < SOI_{main} \\ \phi_{DI} & \theta > SOI_{main} \end{cases} \quad (A.6)$$

$$CN_{mix} = \frac{FAR_{st,nhep} \phi_{di} CN_{nhep} + FAR_{st,iso} \phi_{PFI} CN_{iso}}{FAR_{st,nhep} \phi_{DI} + FAR_{st,iso} \phi_{PFI}} \quad (A.7)$$

These changes to the definitions of ϕ_{DI} and CN_{mix} as shown in Eq. A.6 and Eq. A.7 enable the MKIM to detect SOC accurately. However, there are two cases that can happen when split injection is used.

1. SOI_{main} before SOC detected by MKIM

If the main injection happens before the MKIM detects the SOC, then,

$$SOC_{pilot} = SOC_{main} \quad (A.8)$$

2. SOI_{main} after SOC detected by MKIM

If the main injection happens after MKIM detects the SOC, then,

$$SOC_{main} = SOC_{pilot} + ID \quad (A.9)$$

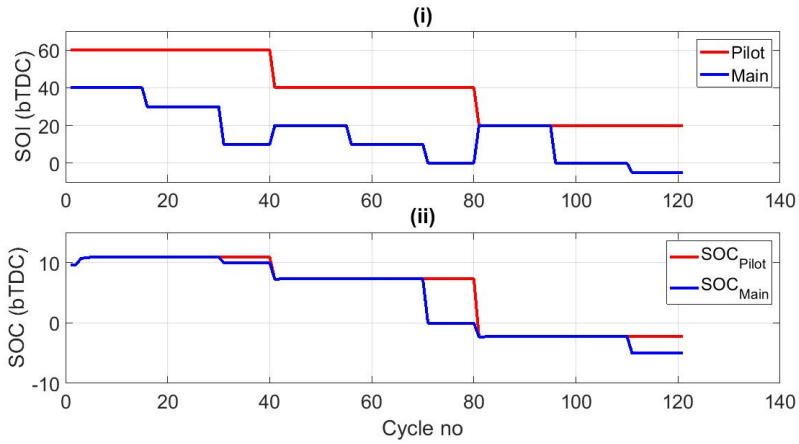
where

$$ID = \frac{K}{CN_{mix}} \quad (A.10)$$

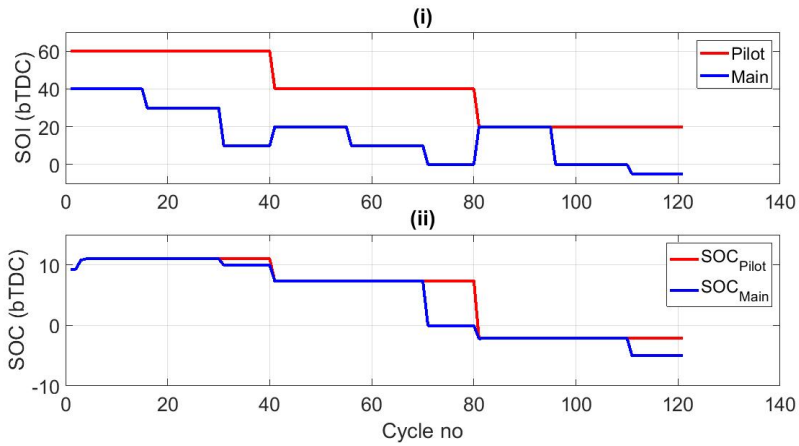
where K is a constant that needs to be parametrized.

An example of variation in SOC_{pilot} and SOC_{main} based on SOI_{pilot} and SOI_{main} is shown in Fig. A.2

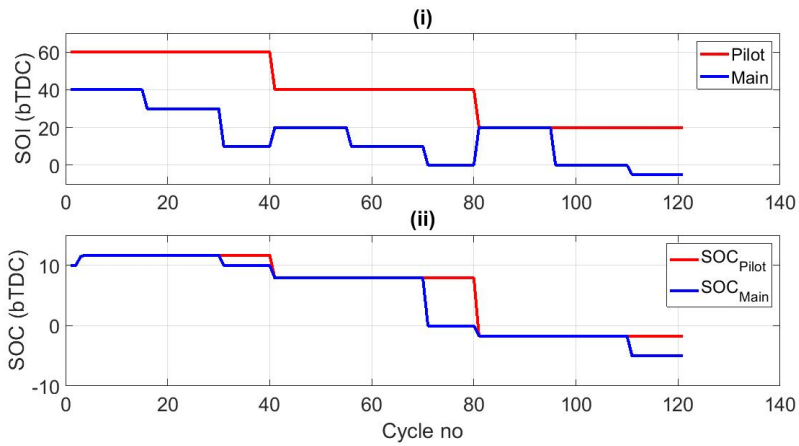
It can be seen in the Fig. A.2 that when SOI_{main} is after SOC_{pilot} , there is a delay from SOC_{pilot} to SOC_{main} . Also, when comparing SOC_{pilot} between Fig. A.2 (a), (b) and (c), it can be seen that the SOC_{pilot} is advanced when ρ_{pilot} is higher. This potentially gives the opportunity to use ρ as a manipulated variable to control SOC.



(a) $\rho_{pilot} = 10\%$



(b) $\rho_{pilot} = 50\%$



(c) $\rho_{pilot} = 90\%$

Figure A.2: Effect of ρ and SOI on SOC

Appendix B

Combustion regime separation in RCCI combustion

In section 3.7 and 4.1 an LPV representation of the dynamic RCCI model was discussed. The scheduling parameter that is used is Premixed Ratio (PR) which is also a known manipulated variable for CA50 control [3, 4]. But, using PR as a scheduling parameter inhibits it from being used as a manipulated variable. This is because the scheduling parameter defines the LPV representation and when the controller manipulates this parameter, it effectively changes the state space representation that defines the plant near that operating point. This leads to inaccuracies during control. Hence, a new scheduling parameter that can be used to define the plant's non linearity is required so that PR can be used as a manipulated variable.

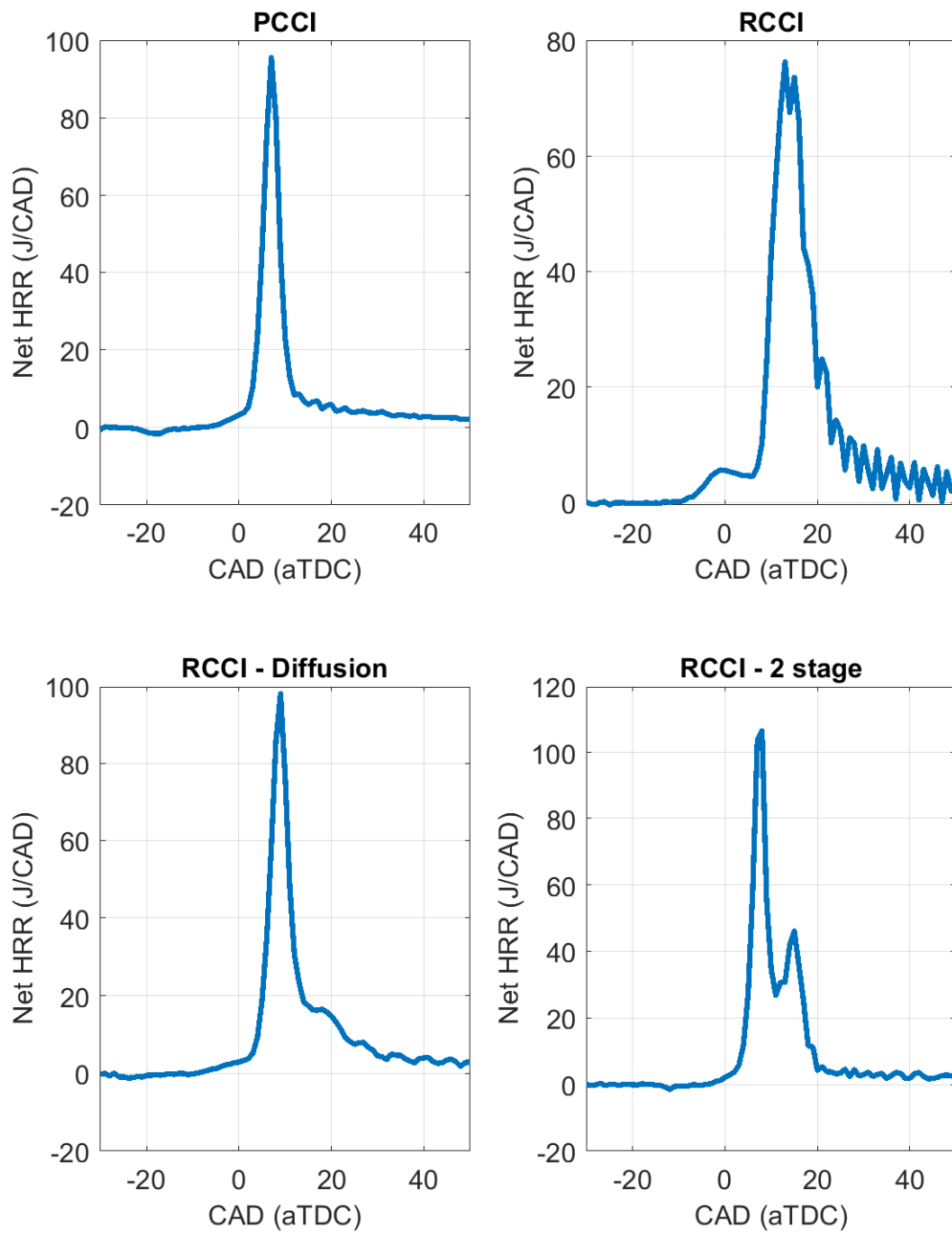
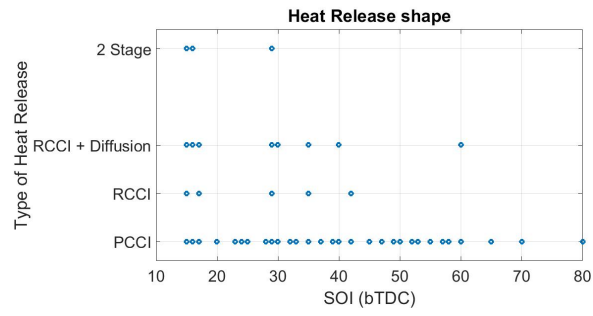


Figure B.1: Different combustion regimes seen during RCCI operation

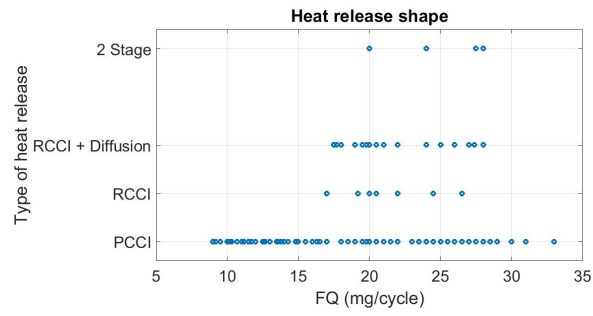
In order to explore a scheduling parameter, it is important to understand how the plant varies in order to pick the right parameter or combination of parameters. Fig. B.1 represents the different combustion regimes encountered in RCCI combustion. In principle, if a parameter or combination of parameters could separate the operating points leading to each of these combustion regimes, that would be an ideal scheduling parameter.

Fig. B.2 shows how different input and intermediate parameters effect the heat release shapes. Other parameters such as $P_{in}, T_{in}, P_{soc}, T_{soc}, X_{rg}$ etc., were explored for differentiating between the different combustion regimes. However, just like the parameters in Fig. B.2 none showed a clear distinction between the different combustion regimes.

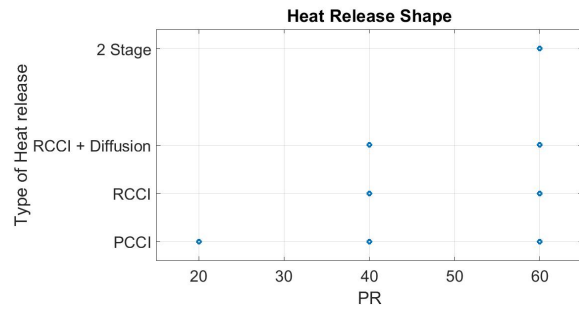
Hence, a combination of different parameters needs to be explored in order to separate the different combustion regimes that occur during RCCI operation. Fig. B.3 represents an attempt to do the same. The X-axis is a function of ϕ_{pfi} and the Y-axis is a function of SOI, PR, X_{rg} . The figure shows that the combustion regimes can be localized into one specific combination of the X and Y values. However, there are more intermediate parameters that can be explored to reach a combination of functions that would clearly distinguish between the combustion regimes. A combination of those function would be an ideal scheduling parameter for the LPV representation of the dynamic RCCI engine model.



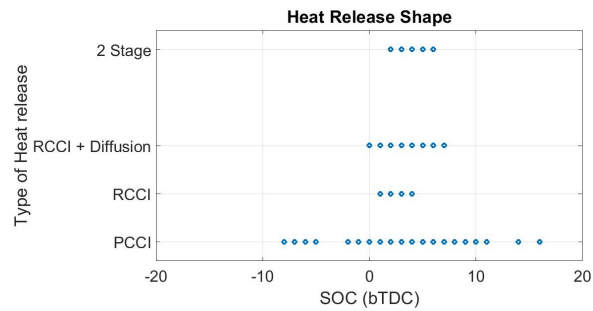
(a) Effect of SOI



(b) Effect of FQ



(c) Effect of PR



(d) Effect of SOC

Figure B.2: Effect of different parameters on heat release shape

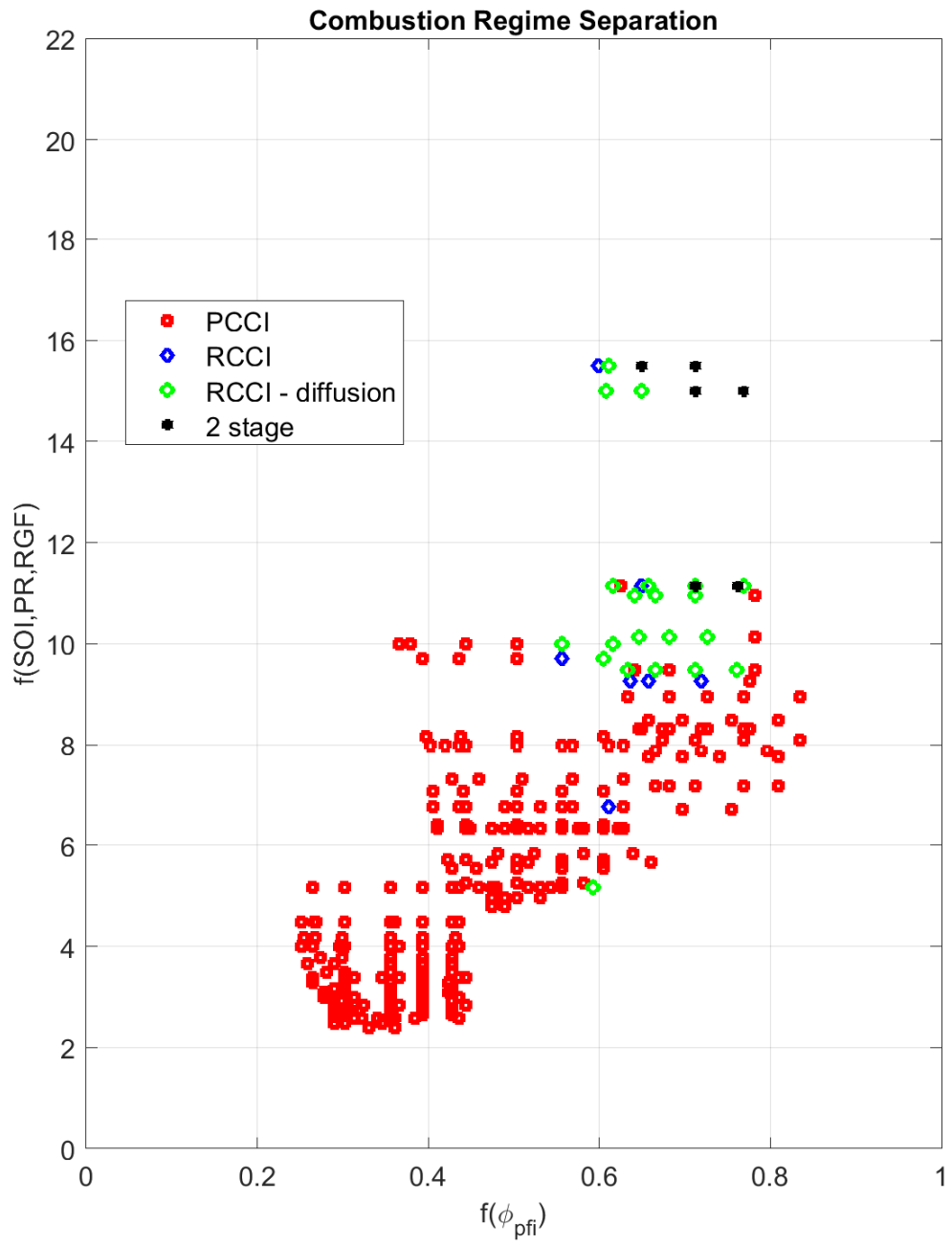


Figure B.3: Combustion regime separation

Appendix C

Experimental Data used for Parametrizing the MVM for MPRR

C.1 Data used for parametrizing the MVM for MPRR

Table C.1
Experimental data used for parametrizing the MVM for MPRR

S.no	MPRR	CA50	m_{fuel}	SOI	PR	λ	MAP
(#)	(bar/CAD)	(aTDC)	(mg/cycle)	(bTDC)	(-)	(-)	(KPa)
1	2.71	13.82	17.00	40.00	20.00	1.71	96.50
2	3.31	12.82	19.00	40.00	20.00	1.52	96.50
3	3.62	11.82	21.00	40.00	20.00	1.37	96.50
4	3.76	12.82	23.00	40.00	20.00	1.24	96.50
5	3.73	7.82	17.00	50.00	20.00	1.72	96.50
6	4.70	6.82	19.00	50.00	20.00	1.54	96.50
7	5.54	5.82	21.00	50.00	20.00	1.38	96.50
8	6.04	5.82	23.00	50.00	20.00	1.26	96.50
9	2.96	9.82	17.00	60.00	20.00	1.78	96.50
10	5.12	5.82	19.00	60.00	20.00	1.58	96.50
11	6.65	4.82	21.00	60.00	20.00	1.41	96.50

S.no	MPRR	CA50	m_{fuel}	SOI	PR	λ	MAP
(#)	(bar/CAD)	(aTDC)	(mg/cycle)	(bTDC)	(-)	(-)	(KPa)
12	2.83	13.82	19.00	45.00	30.00	1.56	96.50
13	3.95	10.82	21.00	45.00	30.00	1.40	96.50
14	4.14	11.82	23.00	45.00	30.00	1.28	96.50
15	4.45	11.82	25.00	45.00	30.00	1.15	96.50
16	3.76	9.82	19.00	50.00	30.00	1.56	96.50
17	4.31	8.82	21.00	50.00	30.00	1.41	96.50
18	5.30	.82	23.00	50.00	30.00	1.28	96.50
19	6.02	7.82	25.00	50.00	30.00	1.16	96.50
20	3.76	9.82	19.00	60.00	30.00	1.58	96.50
21	5.11	8.82	21.00	60.00	30.00	1.43	96.50
22	6.58	7.82	23.00	60.00	30.00	1.30	96.50
23	3.28	12.82	20.00	45.00	35.00	1.51	96.50

S.no	MPRR	CA50	m_{fuel}	SOI	PR	λ	MAP
(#)	(bar/CAD)	(aTDC)	(mg/cycle)	(bTDC)	(-)	(-)	(KPa)
24	2.42	14.82	17.00	40.00	10.00	1.79	96.50
25	2.66	15.82	19.00	40.00	10.00	1.59	96.50
26	3.14	13.82	21.00	40.00	10.00	1.41	96.50
27	3.37	13.82	23.00	40.00	10.00	1.25	96.50
28	3.86	6.82	17.00	50.00	10.00	1.80	96.50
29	4.92	5.82	19.00	50.00	10.00	1.60	96.50
30	5.23	5.82	21.00	50.00	10.00	1.41	96.50
31	5.75	5.82	23.00	50.00	10.00	1.25	96.50
32	3.48	7.82	17.00	60.00	10.00	1.84	96.50
33	5.45	4.82	19.00	60.00	10.00	1.63	96.50
34	6.83	1.82	21.00	60.00	10.00	1.45	96.50
35	2.28	10.00	10.00	35.00	20.00	2.88	96.50

S.no	MPRR	CA50	m_{fuel}	SOI	PR	λ	MAP
(#)	(bar/CAD)	(aTDC)	(mg/cycle)	(bTDC)	(-)	(-)	(KPa)
36	4.82	7.00	14.00	35.00	20.00	2.03	96.50
37	5.65	7.00	19.00	35.00	20.00	1.49	96.50
38	7.26	8.00	28.00	35.00	20.00	1.01	96.50
39	3.77	8.00	14.00	40.00	40.00	2.01	96.50
40	6.03	6.00	17.00	40.00	40.00	1.65	96.50
41	7.36	5.00	20.00	40.00	40.00	1.39	96.50
42	8.14	5.00	24.00	40.00	40.00	1.16	96.50
43	8.59	7.00	28.00	40.00	40.00	0.99	96.50
44	5.37	7.00	19.00	45.00	60.00	1.50	96.50
45	6.71	8.00	22.00	45.00	60.00	1.28	96.50
46	9.47	7.00	25.00	45.00	60.00	1.12	96.50
47	10.62	8.00	28.00	45.00	60.00	1.00	96.50

S.no	MPRR	CA50	m_{fuel}	SOI	PR	λ	MAP
(#)	(bar/CAD)	(aTDC)	(mg/cycle)	(bTDC)	(-)	(-)	(KPa)
48	2.48	6.00	9.00	25.00	20.00	3.10	96.50
49	2.68	6.00	10.00	25.00	20.00	2.77	96.50
50	3.60	7.00	13.00	25.00	20.00	2.11	96.50
51	3.73	8.00	18.00	25.00	20.00	1.52	96.50
52	3.86	9.00	22.00	25.00	20.00	1.24	96.50

4

C.2 Data used for validating the MVM for MPRR

Table C.2
Experimental data used for parametrizing the MVM for MPRR

S.no	MPRR	CA50	m_{fuel}	SOI	PR	λ	MAP
(#)	(bar/CAD)	(aTDC)	(mg/cycle)	(bTDC)	(-)	(-)	(KPa)
1	4.17	10.00	27.00	25.00	20.00	1.01	96.50
2	3.62	7.00	13.00	30.00	40.00	2.12	96.50
3	4.02	7.00	15.00	30.00	40.00	1.82	96.50
4	5.01	7.00	18.50	30.00	40.00	1.47	96.50
5	5.59	7.00	23.00	30.00	40.00	1.18	96.50
6	6.07	8.00	28.00	30.00	40.00	0.97	96.50
7	4.65	8.00	19.80	35.00	60.00	1.38	96.50
8	5.41	8.00	22.00	35.00	60.00	1.24	96.50
9	6.17	8.00	25.00	35.00	60.00	1.08	96.50
10	6.73	10.00	29.00	35.00	60.00	0.93	96.50
11	2.56	5.00	10.00	25.00	20.00	2.68	96.50

S.no	MPRR	CA50	m_{fuel}	SOI	PR	λ	MAP
(#)	(bar/CAD)	(aTDC)	(mg/cycle)	(bTDC)	(-)	(-)	(KPa)
12	3.99	7.00	18.00	25.00	20.00	1.47	96.50
13	4.12	8.00	22.00	25.00	20.00	1.20	96.50
14	4.57	9.00	26.00	25.00	20.00	1.01	96.50
15	2.78	7.00	11.50	25.00	40.00	2.33	96.50
16	4.10	9.00	18.00	25.00	40.00	1.46	96.50
17	4.54	9.00	22.00	25.00	40.00	1.20	96.50
18	4.62	10.00	26.50	25.00	40.00	0.99	96.50
19	4.08	9.00	18.50	29.00	60.00	1.43	96.50
20	4.52	8.00	20.00	29.00	60.00	1.32	96.50
21	4.74	9.00	24.00	29.00	60.00	1.09	96.50
22	5.69	9.00	28.00	29.00	60.00	0.93	96.50
23	2.08	7.00	10.30	20.00	20.00	2.52	96.50

S.no	MPRR	CA50	m_{fuel}	SOI	PR	λ	MAP
(#)	(bar/CAD)	(aTDC)	(mg/cycle)	(bTDC)	(-)	(-)	(KPa)
24	2.73	9.00	13.00	20.00	20.00	1.98	96.50
25	3.00	11.00	18.00	20.00	20.00	1.43	96.50
26	2.98	12.00	22.00	20.00	20.00	1.17	96.50
27	3.21	14.00	26.00	20.00	20.00	0.99	96.50
28	2.63	7.00	11.20	24.00	40.00	2.32	96.50
29	3.26	8.00	13.60	24.00	40.00	1.89	96.50
30	4.12	9.00	18.00	24.00	40.00	1.41	96.50
31	4.23	11.00	26.00	24.00	40.00	0.98	96.50
32	4.00	9.00	18.00	29.00	60.00	1.43	96.50
33	4.31	9.00	20.50	29.00	60.00	1.25	96.50
34	4.57	9.00	24.00	29.00	60.00	1.06	96.50
35	5.47	8.00	27.50	29.00	60.00	0.93	96.50

S.no	MPRR	CA50	m_{fuel}	SOI	PR	λ	MAP
(#)	(bar/CAD)	(aTDC)	(mg/cycle)	(bTDC)	(-)	(-)	(KPa)

,

Appendix D

Programs and data files summary

D.1 Chapter 1

File Name	File Description
LTC_Comparison.jpg	Figure 1.1
Operating_Points.jpg	Figure 1.2
Sadabadi_Controller.jpg	Figure 1.5
PI_Controller_Arora.jpg	Figure 1.6

Table D.1
Figure Files

File Name	File Description
CLCC_RCCI_litreview_dynamics.vsd	Figure 1.2
CLCC_RCCI_litreview_controls.vsd	Figure 1.4
Thesis_Organisation.vsd	Figure 1.7

Table D.2
Visio Files

D.2 Chapter 2

File Name	File Description
New_LTC_Engine_Setup.vsd	Figure 2.1
exp_setup_2.vsd	Figure 2.2
Data_Acquisition.vsd	Figure 2.3

Table D.3
Visio Files

File Name	File Description
MPRR_Plotting	Figure 2.4
MPRR_std_Plotting	Figure 2.5

Table D.4
Plot files

D.3 Chapter 3

File Name	File Description
HR_Analysis.m	Matlab code for creating plots in Fig 3.1
MPRR_modeling.m	Matlab code for creating plots in Fig. 3.2 and 3.3
MPRR_Transient.m	Matlab code for creating plots in Fig. 3.5 and 3.4
Statistical_Analysis.m	Matlab code for generating plots in Fig. 3.6
LPVmodelling.m	Matlab code for creating plots in Fig. 3.8, 3.9 and 3.10

Table D.5
Plot Files

D.4 Chapter 4

File Name	File Description
LPV_MPC_Visualization.m	Matlab file for plots in Fig. 4.1, 4.2, 4.4, 4.5, 4.6 and 4.7
Split_Injection_Wiebe.m	Matlab file for plot in Fig. 4.8

Table D.6
Plot Files

File Name	File Description
MPC_Control_Model_Schematic.vsd	Figure 4.3

Table D.7
Visio Files

D.5 Appendix A

File Name	File Description
Split_Injection_Wiebe.m	Matlab file for plot in Fig. 4.8
Split_MPRR_Visualization.m	Matlab file for plot in Fig. A.2

Table D.8
Plot Files

D.6 Appendix B

File Name	File Description
Plotting_HRR.m	Matlab file for plots in Fig. B.1
HRR_Effects	Matlab file for plot in Fig. B.2
Scheduling_Parameter_final.m	Matlab file for plot in Fig. B.3

Table D.9
Plot Files

Appendix E

Letters of Permission

For figure 1.1

Copyright Clearance Center RightsLink®

Home Create Account Help LIVE CHAT

SAGE Publishing

Title:	Progress and recent trends in reactivity-controlled compression ignition engines
Author:	Amin Paykani, Amir-Hasan Kakaee, Pourya Rahnama, et al
Publication:	International Journal of Engine Research
Publisher:	SAGE Publications
Date:	06/01/2016
	Copyright © 2016, © SAGE Publications

LOGIN
If you're a copyright.com user, you can login to RightsLink using your copyright.com credentials. Already a RightsLink user or want to learn more?

Gratis Reuse

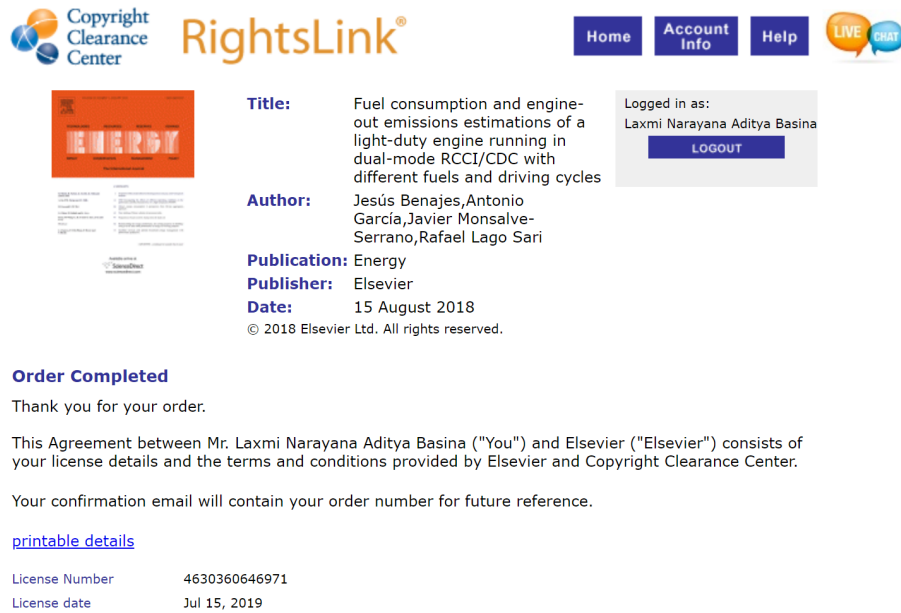
Permission is granted at no cost for use of content in a Master's Thesis and/or Doctoral Dissertation. If you intend to distribute or sell your Master's Thesis/Doctoral Dissertation to the general public through print or website publication, please return to the previous page and select 'Republish in a Book/Journal' or 'Post on intranet/password-protected website' to complete your request.

BACK CLOSE WINDOW

Copyright © 2019 Copyright Clearance Center, Inc. All Rights Reserved. [Privacy statement](#) [Terms and Conditions](#). Comments? We would like to hear from you. E-mail us at customercare@copyright.com

Figure E.1: Letter of permission

For figure 1.3



The screenshot displays the Elsevier RightsLink interface. At the top left, the Copyright Clearance Center and RightsLink logos are visible. Navigation buttons for Home, Account Info, and Help are present, along with a LIVE CHAT icon. The main content area shows a thumbnail of the article cover, followed by the article title, author names (Jesús Benajes, Antonio García, Javier Monsalve-Serrano, Rafael Lago Sari), publication name (Energy), publisher (Elsevier), and date (15 August 2018). A 'Logged in as:' section shows the user name 'Laxmi Narayana Aditya Basina' and a LOGOUT button. Below this, an 'Order Completed' message thanks the user and provides a link to 'printable details'. At the bottom, license details are listed: License Number 4630360646971 and License date Jul 15, 2019.

Copyright Clearance Center RightsLink®

Home Account Info Help LIVE CHAT

Title: Fuel consumption and engine-out emissions estimations of a light-duty engine running in dual-mode RCCI/CDC with different fuels and driving cycles

Author: Jesús Benajes, Antonio García, Javier Monsalve-Serrano, Rafael Lago Sari

Publication: Energy

Publisher: Elsevier

Date: 15 August 2018

© 2018 Elsevier Ltd. All rights reserved.

Logged in as:
Laxmi Narayana Aditya Basina
LOGOUT

Order Completed

Thank you for your order.

This Agreement between Mr. Laxmi Narayana Aditya Basina ("You") and Elsevier ("Elsevier") consists of your license details and the terms and conditions provided by Elsevier and Copyright Clearance Center.

Your confirmation email will contain your order number for future reference.

[printable details](#)

License Number 4630360646971
License date Jul 15, 2019

Figure E.2: Letter of permission